

**High Definition Metrology based Process Control:  
Measurement System Analysis and Process Monitoring**

**by**

**Saumuy Suriano Puchala**

A dissertation submitted in partial fulfillment  
of the requirements for the degree of  
Doctor of Philosophy  
(Industrial and Operations Engineering)  
in the University of Michigan  
2013

Doctoral Committee:

Professor S. Jack Hu, Co-Chair  
Assistant Research Scientist Hui Wang, Co-Chair  
Professor Thomas J. Armstrong  
Professor Judy Jin  
Professor Ji Zhu

© Saumuy Suriano Puchala 2013

*To my family*

## ACKNOWLEDGEMENTS

I would like to express my deepest thanks to Prof. Jack Hu for giving me the opportunity to join his lab. Through his guidance and encouragement, I have grown both personally and professionally. He has been a thoughtful and wonderful mentor, and I am grateful that I had the chance to learn from him. I am also extremely thankful to Dr. Hui Wang for his endless questioning and creativity which greatly improved this research. I appreciate his support and guidance; most of all, I appreciate his friendship.

I would like to thank my committee members, Prof. Thomas Armstrong, Prof. Judy Jin and Prof. Ji Zhu for their valuable comments. I am particularly grateful to Prof. Jin for always making the time for research discussions and for her helpful suggestions.

Conversations with Hu-lab members have sparked many research ideas and discussion. I am thankful to them for their camaraderie and collaborative spirit which has made work enjoyable. I am also grateful to the faculty and staff that the IOE department, particularly Tina, Wanda and Matt, for their good cheer and helpfulness.

Throughout my time in the program, I have been extremely blessed to have the encouragement of family and friends. I especially could not have finished this dissertation without my parents, siblings and husband. They have believed in me, pushed me when needed and have been a constant source of loving support and joy.

## TABLE OF CONTENTS

DEDICATION.....	ii
ACKNOWLEDGEMENTS.....	iii
LIST OF TABLES.....	vi
LIST OF FIGURES.....	vii
ABSTRACT.....	xi
CHAPTER 1	
INTRODUCTION.....	1
1.1. Motivation.....	1
1.2. State of the art.....	6
1.3. Research Objectives.....	12
1.4. Organization of Thesis.....	13
CHAPTER 2	
SURFACE MODELING THROUGH FUSION OF PROCESS AND HDM DATA.....	15
2.1. Cross correlations uncovered by HDM systems.....	16
2.2. Surface prediction considering spatial and cross correlations.....	20
2.3. Case Study.....	22
2.4. Chapter Summary.....	24
CHAPTER 3	
MEASUREMENT SYSTEM ANALYSIS FOR HIGH DEFINITION METROLOGY USING CROSS-CORRELATION.....	26
3.1. Proposed Framework for High Dimensional Multivariate MSA.....	32
3.1.1. HDM Data Regularization using Spatial and Cross- Correlations.....	32
3.1.2. MSA for HDM.....	38
3.2. Case Studies.....	40
3.2.1. Planar Measurements MSA.....	41
3.2.2. Volumetric Shell Measurements MSA.....	46

3.3.	Discussion .....	49
3.4.	Chapter Summary .....	50
CHAPTER 4		
	SURFACE VARIATION MONITORING USING HDM .....	52
4.1.	Sequential Monitoring of HDM Data .....	53
4.1.1.	Preprocessing of HDM Data .....	54
4.1.2.	Large Scale Monitoring using Parameterized Principal Curve .....	56
4.1.3.	Localized Monitoring using Spatial Clustering .....	65
4.1.4.	Small Scale Monitoring using Variograms .....	68
4.1.5.	Case Study .....	71
4.2.	Progressive Monitoring of Multi-resolution Data under Bayesian Framework .....	75
4.2.1.	Fusion Model based Inference .....	77
4.2.2.	Single Linkage Clustering Monitoring using Surface Fusion Model .....	79
4.2.3.	Case Study .....	87
4.3.	Chapter Summary .....	91
CHAPTER 5		
	MULTISTAGE MODELING AND MONITORING OF HIGH DEFINITION METROLOGY DATA .....	94
5.1.	Background: Modeling of Multistage Interdependence using Functional Morphing .....	96
5.2.	Multistage Monitoring using Functional Morphing and Spatial Correlation .....	99
5.3.	Case Study .....	103
5.4.	Chapter Summary .....	110
CHAPTER 6		
	CONCLUSION .....	112
6.1.	Conclusions .....	112
6.2.	Future Work .....	114
	REFERENCES .....	118

## LIST OF TABLES

Table 3.1.	MSA Case study Analysis Methods and Data Set Summary .....	40
Table 3.2	Eigenvalues for Parts, Measurement and Gauge Covariance Matrices for Planar Measurements .....	44
Table 3.3	Gauge %R&R and P/T ratio for Planar Measurement Spatial Clusters.....	45
Table 3.4	Eigenvalues for Parts, Measurement and Gauge Covariance Matrices for Volumetric Measurements .....	48
Table 3.5	%R&R and P/T Ratio for Volumetric measurement Spatial Clusters .....	48
Table 4.1	Material Properties for FEM Simulation .....	62
Table 4.2	Model Coefficients for the first 4 Principal Components .....	64
Table 4.3	OOB pattern based on individual control chart points.....	84
Table 4.4	Values of Quality Characteristics for Monitoring .....	90
Table 5.1	Cross-Covariance Parameters for Model Residuals .....	105
Table 5.2	Average Surface Prediction RMS for each Surface Model .....	107

## LIST OF FIGURES

Figure 1.1	(a) HDM measurement and (b) CMM measurement.....	2
Figure 1.2	(a) HDM Patches and (b) CMM Trace on an Automotive Engine Head.....	3
Figure 1.3	New surface features Uncovered using HDM .....	4
Figure 1.4	Cross-Correlation between Surface Height and Arc Length .....	5
Figure 1.5	Surface Data Correlation between Machining Stages [3].....	5
Figure 1.6	Thesis Organization .....	14
Figure 2.1	Cross-Correlation between Surface Height and MRR [1] .....	18
Figure 2.2	Cross-Correlation: Surface Height vs. Cutter Insert Engagement [2] .....	19
Figure 2.3	Cross-Correlation: Surface Height vs. Feed rate or Tool Mark Spacing.....	19
Figure 2.4	Cross-Correlation: Surface Height vs. Clamping torque .....	20
Figure 2.5	Data Inputs for Data Fusion Surface Prediction .....	23
Figure 2.6	Prediction Results .....	24
Figure 2.7	Comparison Between Prediction Cross Sections.....	24
Figure 3.1	(a) 3D planar Measurement (b) Volumetric Shell Measurement.....	27
Figure 3.2	HDM Measurements of two parts.....	28
Figure 3.3	Proposed Measurement System Analysis Framework.....	32
Figure 3.4	(a) Regularized Part Measurements (b) Point Cloud Part Measurements ...	33
Figure 3.5	Projection of Scattered Data onto Grids .....	35
Figure 3.6	Procedure for Identifying Prediction Locations.....	36
Figure 3.7	Volumetric Shell Object Partition for Interpolation .....	38
Figure 3.8	Sample Planar Measurements used for Laser Interferometer MSA .....	41



Figure 3.9	%R&R values and %R&R distribution for (a) Measurements for a Normal Process (b) Measurements with a Large Operator Effect, and (c) Measurements with Large Gauge Error .....	43
Figure 3.10	First three 2-D Principal Components of Planar Measurements .....	43
Figure 3.11	Spatial Cluster Scheme on HDM measurements using K-means Algorithm with (a) normal process Measurements (b) Measurements with an Operator Effect (c) Measurements with a Gauge Error .....	45
Figure 3.12	Volumetric Part Measurements from Laser Scanner .....	46
Figure 3.13	%R&R distributions for (a) Normal Process Measurements (b) Measurements with Operator Effect and (c) Measurements with Gauge Effect.....	47
Figure 4.1	Scatter Plot of Spatial Data between Regions.....	53
Figure 4.2	Proposed HDM data monitoring Framework .....	54
Figure 4.3	Decomposition of HDM Data.....	55
Figure 4.4	An Example of a Principal /Curve for 2-D case .....	58
Figure 4.5	Principal Curve projection at Regions 33 & 36.....	58
Figure 4.6	Part and Machining Operation for Case Study .....	63
Figure 4.7	Scree Plot based on PCA .....	63
Figure 4.8	Multivariate Control Chart based on the Parameterized Principal Curve Model.....	64
Figure 4.9	$T^2$ control Chart for Monitoring Principal Components .....	65
Figure 4.10	Theoretical Variogram.....	70
Figure 4.11	$T^2$ control chart for Engine Head Principal Components .....	72

Figure 4.12	Scree Plot for Selection of $k$ .....	72
Figure 4.13	K-means partition for Average Part.....	73
Figure 4.14	Localized Monitoring using Spatial Clustering.....	73
Figure 4.15	Patch Selection for Case Study Data .....	74
Figure 4.16	Surface and Variogram for Part 5, Patch 9 .....	74
Figure 4.17	Variogram-based Control Chart.....	75
Figure 4.18	Proposed Monitoring Framework .....	77
Figure 4.19	Spatial distribution Patterns of Out of Limit Points.....	81
Figure 4.20	Clustering Algorithm Steps.....	83
Figure 4.21	Scatter Plot of MRR vs. Surface Height .....	88
Figure 4.22	(a) Normal Part (b) Defective Part.....	90
Figure 4.23	Surface Variation Monitoring.....	91
Figure 4.24	OOL points for Normal and Defective Parts .....	91
Figure 5.1	(a) Part surface Changes in Multistage Process (b Two-stage machining Process Part Measurements (c) Inter-stage Surface Shape Compensation [3] .....	95
Figure 5.2	Monitoring using Backward Morphing .....	99
Figure 5.3	False alarm and Misdetection Scenarios Using Backward Morphing.....	100
Figure 5.4	Part Surface Measurements using (a) HDM and (b) Multi-resolution Metrology (CMM and profilometer) .....	101
Figure 5.5	Proposed Monitoring Framework for Multistage Processes.....	104
Figure 5.6	Part Surface (a) After Milling and (b) After Drilling .....	104
Figure 5.7	Normal and Defective Part Surfaces after Stage 1 and 2.....	105

Figure 5.8	Predicted Surfaces for Several Models .....	107
Figure 5.9	Individual Monitoring Charts for Stage 1 using (a) Morphed Estimates and (b) Morphed Estimates Adjusted using Limited Measurements.....	108
Figure 5.10	Monitoring of OOC Patterns using Control Charts for Upstream Stage ...	109
Figure 5.11	Cluster Locations for Normal and Defective Parts for Upstream Stage ....	110
Figure 6.1	Two level closed loop feedback control .....	115

## ABSTRACT

Process control in high precision machining necessitates high-definition metrology (HDM) systems that provide fine resolution data needed to characterize surface shape. HDM data is critical for the evaluation of process surface variation, as it reveals local surface patterns that are undetectable using low definition metrology (LDM) systems. Monitoring of the part-to-part variation of these patterns identified by HDM enables the detection of abnormal surface variation and the degradation of process conditions.

HDM systems present many opportunities for surface variation reduction. However, there are challenges to using HDM data for process control. Conventional HDM systems are inefficient and may take a long time to measure a part, such that sufficient samples cannot be obtained for process control purposes. In addition, conventional monitoring methods are difficult to implement due to the high density of data.

A new study uncovered significant cross-correlations between part surface height and process variables in an automotive engine milling process. This dissertation aims to apply new insights gained from HDM to develop algorithms and methods for surface variation control, specifically:

- *Surface modeling through fusion of process variables and HDM data:* An improved surface model is developed by incorporating process and multi-resolution data through spatial and cross-correlation to increase prediction

accuracy and reduce the amount of HDM measurements necessary for process control.

- *Measurement system analysis for HDM using:* A method to effectively estimate the gage capability for HDM systems is proposed.
- *Surface variation monitoring using HDM data:* A sequential monitoring framework is developed to monitor surface variations as reflected by HDM data. Based on the surface data-process fusion model, a progressive monitoring algorithm under a Bayesian framework is developed to monitor surface variations when limited HDM measurements are available.
- *Multistage modeling and monitoring of HDM Data:* A morphing-based approach is proposed to model process multistage interdependence. A new multistage monitoring procedure is developed based on the morphing model.

The research presented in this dissertation will aid in transforming quality control practices from dimensional variation reduction to surface shape variation control. The proposed HDM data monitoring algorithms can be extended to other high precision manufacturing processes.

## CHAPTER 1

### INTRODUCTION

#### 1.1. Motivation

Process control in high precision machining necessitates high-definition metrology (HDM) systems that provide fine lateral (x-y) resolution data needed to characterize surface shape. HDM systems can measure up to millions of points per part, with resolution ranging from nanometers to microns. HDM data is critical for the evaluation of process performance with micron-level accuracy. Figure 1.1a shows the HDM measurement (lateral resolution: 300 $\mu$ m) of a deck face on an automotive engine head. Local variations surrounding the cylinder bores can be clearly observed, a detail that is not well captured by a coordinate measuring machine (CMM, lateral resolution: 0.2-1mm) that scans the surface along a few preprogrammed traces (Figure 1.1b), or traditional profilometric measurement systems. Such surface variation patterns not only significantly impact the sealing performance of engine assemblies but also reflect cutting force dynamics during machining processes [1]. Monitoring of the part-to-part variation of these patterns identified by the new HDM helps detect tool condition degradation including the stiffness change and the abnormal wear of cutting inserts in a spindle-cutter system [2].

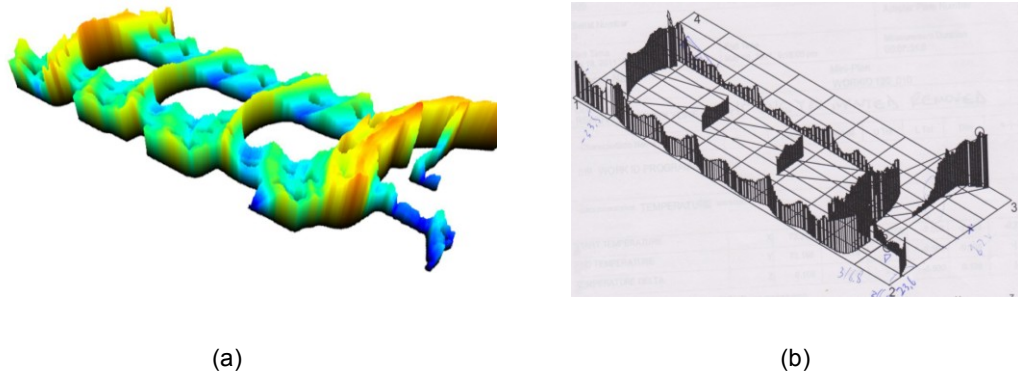


**Figure 1.1 (a) HDM measurement and (b) CMM measurement**

Process control based on HDM data faces two major challenges:

1. *Efficiency of metrology systems:* Obtaining HDM measurements for process monitoring can be difficult since HDM systems are costly and taking measurements is time-consuming. Due to the high cost, manufacturers may deploy fewer HDM machines in a plant, resulting in an insufficient sample size and further restricting the number of parts that can be measured. Therefore, it is common practice to monitor the process characteristics using a combination of HDM and low definition metrology (LDM). The HDM measurements are taken on pre-selected patches on the part surface, while the LDM measures the part surface along a few pre-programmed traces. Figure 1.2 shows the (a) HDM measurements and (b) LDM measurements used to monitor an automotive engine head process.
2. *Methodologies for HDM Data Monitoring:* The large density of measurement points obtained by HDM makes conventional statistical process control (SPC) approaches difficult to use. One approach is to monitor each measurement point individually using univariate methods such as Shewhart control charts, but this increases the false

alarm rates as the data density increases. A second approach is to use multivariate methods such as the  $T^2$  control chart; however these methods are not capable of handling surface data in the millions of points. Neither of these approaches aid in finding the defect area location, which is important for the diagnosis of abnormal surface variation.

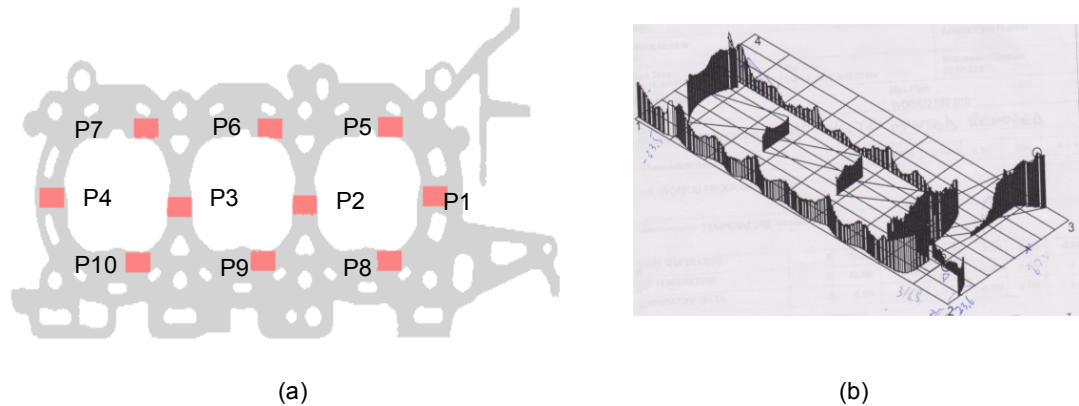


**Figure 1.2 (a) HDM Patches and (b) CMM Trace on an Automotive Engine Head**

### ***New Opportunities Enabled by HDM***

A recent study [1] provided new insights on surface variation which present opportunities to address the aforementioned challenges, as follows:

- *Understanding surface features*: HDM technology can reveal previously unseen local variations on the part surface. For example, the HDM measurement of an engine head in Figure 1.3 clearly shows local variations on the part surface such as patterns 1-3. When using CMMs, these variations are undetected due to the low density of measurements, as shown in Figure 1.2b.



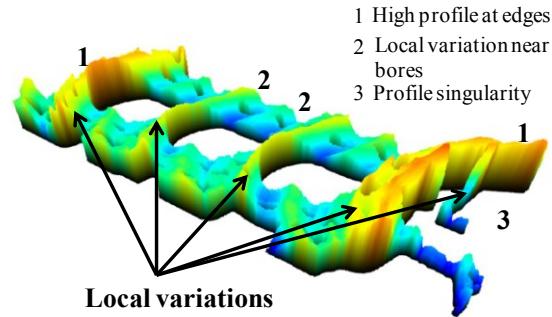


**Figure 1.3 New surface features Uncovered using HDM**

- *Establishing cross-correlations between surface and process variables:* The availability of fine resolution data over the entire part surface has revealed correlations between the part surface and process variables that were previously undiscovered [1]. One such cross-correlation is between the average surface profile along the feed direction and the arc length of a cutter engaged in cutting. For example, [1] shows that the surface height is correlated to the part geometry and the amount of material removal along the cutting feed direction, i.e., the average surface profile becomes high where more material is present. It can be conjectured that this correlation may result from variations of the axial cutting force between the cutter and workpiece which is proportional to the variations in the material removal rate (MRR), i.e., amount of material removal volume per unit feed. A large axial cutting force could cause a higher relative cutter-workpiece displacement leading to high surface profile. When other variables are constant, the surface height is linearly correlated to the cutting arc length. Other such cross-correlations will be explored in more detail in Section 2.

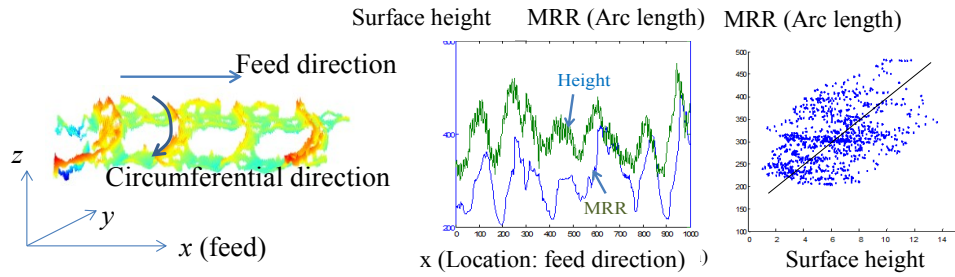


**Figure 1.4 Cross-Correlation between Surface Height and Arc Length**

- Multistage Interdependence:* Surface shape variations could be interdependent over multiple stages. For example, a machined surface may change its shape as it goes through a multistage machining process (Figure 1.5a) because a downstream operation can change the surface characteristics generated from a prior upstream operation. Figure 1.5b shows a workpiece which goes through a face milling operation (Op  $i$ ) that mills its top surface followed by a hole drilling operation on its side (Op  $i+1$ ). Due to the drilling torque, the top surface is twisted thus creating a local height variation. Understanding the interdependency between these local variations resulting from subsequent machining stages will enable between-stage monitoring of the surface shape.

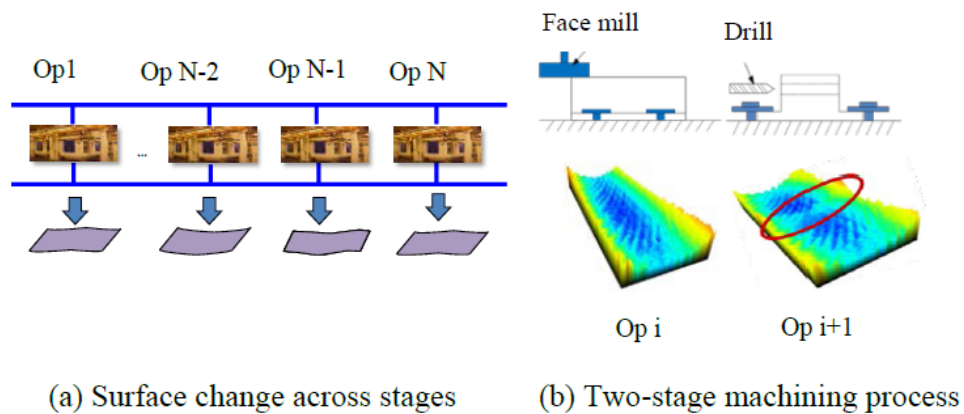


**Figure 1.5 Surface Data Correlation between Machining Stages [3]**

These new insights can be utilized to improve the surface modeling by fusing process variables and multi-resolution data, for surface variation monitoring and multistage modeling and monitoring of HDM data.

This dissertation aims to apply the insights gained from HDM systems to develop algorithms and methods for surface variation control using high dimensional quality characteristics by (1) modeling part surfaces using the fusion of process and HDM data, (2) developing methods for Measurement System Analysis (MSA) using high dimensional data, (3) applying the surface models to create cost effective monitoring methods for high dimensional quality characteristics, and (4) modeling the inter-stage surface variation relationship in multistage manufacturing processes.

## **1.2. State of the art**

This section reviews research related to surface variation modeling, single stage and multistage HDM data monitoring.

### ***Surface variation modeling***

Researchers have taken different approaches to address the challenges of measuring and analyzing HDM data. These approaches include interpolating and extrapolating surface forms from measured points through least squares [4] and B-spline methods [5-7]. The surface shape may also be estimated using spatial statistics by taking into account spatial dependence among sampled points. Such spatial correlation reflects spatial similarities between data in the same vicinity of the part surface, and has been extensively utilized to interpolate and extrapolate surface data for form error estimation

[8, 9] and remote sensing applications, [10-13]. The surface model usually follows the general form of

$$Y(\mathbf{x}) = \mathbf{f}_T(\mathbf{x}) \boldsymbol{\beta} + Z(\mathbf{x}) + \boldsymbol{\varepsilon} \quad , \quad (1-1)$$

where the functions,  $\mathbf{f}_T$ , are assumed known,  $\boldsymbol{\beta}$  is the vector of regression coefficients, and  $Z(\mathbf{x})$  is a Gaussian process with zero-mean and covariance function  $\sigma^2\psi$ . The model was also employed to determine the optimal measurement strategy [14].

Other proposed approaches combine limited HDM data with low definition metrology (LDM) data to estimate surface shape with high resolution. There are two main ways in which the data are combined: the first one requires individual modeling of both sources of data and using statistical inference to estimate the data at a medium or new scale [15]; the second method is to create a linkage model [16, 17] by which the low z-resolution (vertical resolution) data is linked to the data with high z-resolution, such that

$$y_h(x_i) = \alpha_1 \sum_{j=1..m} K(x_i, x_j) \eta_l(x_j) + \alpha_0 + \boldsymbol{\varepsilon} \quad , \quad (1-2)$$

where  $y_h(x_i)$  is the high resolution response,  $\alpha_1$  and  $\alpha_0$  are the scale and location coefficients,  $K(x_i, x_j)$  is a kernel or Gaussian function,  $\eta_l$  are the LDM measurements, and  $\boldsymbol{\varepsilon}$  is a normally distributed error. In addition, research also focused on using the same vertical resolution data and combining metrologies of different lateral resolutions to improve surface prediction [18, 19].

For nonlinear cases, a model for the data surface height can be

$$\mathbf{y}(\mathbf{x}_i) = \mathbf{f}(\mathbf{t}_i) + \varepsilon, \quad (1-3)$$

where the function vector  $\mathbf{f}(\mathbf{t}_i)$  is used to estimate the spatial nature of nonlinear variation patterns. Principal curve estimation has been demonstrated [20-22] to be an effective method to identify the nonlinear patterns  $\mathbf{f}(\mathbf{t}_i)$  among multi-dimensional data, especially for two-dimensional image processing [23, 24]. However, this method is not computationally efficient in processing high-dimensional data. Apley and Zhang [20] proposed a dimensional reduction method through PCA filtering given that the nonlinear patterns can be approximated as piecewise linear, which is reasonable for most of manufacturing applications. Although the principal curve can provide a visualization of spatial variation, a quantitative method is essentially needed to detect the abnormal variation patterns and evaluate the associated risk for the quality control purposes.

*Research Gap:* A significant amount of work related to multi-resolution surface data has focused on surface form prediction, multi-resolution data registration, and measurement strategy evaluations using spatial correlations. These spatial-correlation enabled methods rely on the density of the measured data points; but an inadequate amount of measurements could fail to capture the local variations, such as the variations surrounding the cylinder bores in Figure 1.3. There is a lack of research on combining engineering insights with spatial data modeling to improve surface variation modeling, especially for a large surface with complex designed geometry given limited measurements due to a time or cost constraint.

### ***Process Monitoring and Diagnosis using Surface Data***

Various multivariate statistical methods have been developed for identifying and analyzing variation patterns in multi-dimensional data [25-28]. Principal Component

Analysis (PCA) has been applied [25, 27] to extract the process variation patterns in autobody assembly when only one single fault is present at a time. To characterize a process with multiple faults, the most commonly used approaches assume that the high-dimensional feature variation can be represented as a linear combination of contributions from multiple variation patterns [25, 28]. Each variation pattern is either obtained from process knowledge through off-line modeling or identified from variation patterns in data without the process knowledge a priori. In addition, nonlinear variation patterns were captured by principal curve modeling [20].

Quality control based on high-dimensional data has been focused on part inspection and process performance evaluation. The objective of part inspection is to characterize surface geometric features for each part by fitting a parameterized model to the data [29-31]. The model parameters are compared with specification for conformance of each part to the geometric tolerance. These parametrization methods are simple to implement, but often are not effective in detecting changes in local variation patterns because the model is fit to the global trend. Thus, wavelet based approaches for fault detection and part characterization have been explored extensively [32-35], as they allow for a multiscale decomposition of surfaces, and thus global and local scales can be characterized. The wavelet analysis is data driven but it is challenging to monitor the large number of wavelet coefficients that are generated on the entire part surface. Process variation monitoring (e.g., using Hotelling  $T^2$  control chart [36]) is used to evaluate process stability (repeatability) by measuring a sequence of parts. This approach uses one test statistic to characterize the overall variation of multiple variables and can assist in the detection of

process faults. But such monitoring provides very limited insights into variation source diagnosis and cannot be directly used with high dimensional data.

*Research Gap:* With the increased amount of data provided by HDM, monitoring data points individually may lead to high false alarm rates (type I error). Therefore, the major challenge in monitoring multidimensional data is the reduction of the data dimension by discerning the critical features of the product and monitoring these features jointly without inflating the type I error. In addition, previously proposed monitoring methods make a linear variation pattern assumption, whereas with HDM a non-linear variation pattern might exist. A methodology that takes into consideration the HDM non-linear pattern variation and spatial autocorrelation is needed to effectively monitor HDM data. When the availability of HDM data is limited because of measurement time or cost constraints, researchers have proposed surface prediction models combining multi-resolution data. There is a lack of research incorporating process variable information to improve the accuracy of surface predictions for surface variation monitoring using a low sample of HDM data.

### ***Multistage Process Control using Surface Data***

Methods have been proposed to improve the performance of multistage manufacturing processes (MMP's). The related work includes regression-based methods [37], Bayesian methods [38, 39], control chart allocation strategies [40, 41] and cause-selecting strategies [42]. A detailed review of SPC for MMP's can be found in [43]. In addition to SPC methods, dimensional variation propagation has been studied using the stream of variation (SoV) methodology [44, 45], which models variation through

dimensional quality state spaces or vectors, creating between-stage variation models through rigid body kinematics [46-49], finite element analysis (FEA) [50], or by statistical approaches [51]. These SoV methods have been successfully applied to improve tolerancing, process adjustment and diagnosis [52-55]. However, the SPC and SoV methodologies have mainly been applied to dimensional variation control instead of surface variation control.

*Research Gap:* Although the existing SoV methods are effective in modeling the variation propagation from upper stream to downstream, the method for capturing the impact of certain downstream stages on the surface variations generated at upstream stages is still lacking. Furthermore, the majority of these methods focus on dimensional control, and not surface variation control. The SoV methodology has mainly been applied to dimensional variation control instead of 3D surface variation control. Although the existing SoV methods are effective on modeling the variation propagation from upper stream to downstream, the method for capturing the impact of certain downstream stages on the surface variations generated at upstream stages is still lacking.

### ***Summary***

There is a lack of effective methodologies for the monitoring of high-precision multidimensional data in manufacturing processes. The overall research gaps are the lack of (1) surface variation modeling considering cross-correlation between the surface height data and process variables, (2) efficient monitoring and diagnostic methods using HDM data for quickly detecting and locating abnormal surface variation changes, and (3)



understanding of surface variation patterns and the effect of downstream stages on surface variations generated from the upstream stages (multistage interdependence).

### 1.3. Research Objectives

To fill the research gaps as outlined above, this dissertation proposes:

- *Surface modeling through fusion of process and HDM data:* An improved surface model is developed by incorporating process and multi-resolution data through spatial and cross-correlation. The proposed model is as follows:

$$Z(\mathbf{s}) = \mu(\mathbf{s}) + w(\mathbf{s}) + \varepsilon(\mathbf{s}), \text{ where}$$

Mean	$\mu(\mathbf{s}) = [\mathbf{1} \quad \mathbf{U}(\mathbf{s})^T] \boldsymbol{\beta}$	
Covariance	$w(\mathbf{s}) \sim \text{GP}(0, \sigma^2 \rho(\phi; \ \mathbf{s}_i - \mathbf{s}_j\ ))$	, (1-4)
Error	$\varepsilon(\mathbf{s}) \sim \text{N}(0, \tau^2)$	

where the mean of the expression,  $\mu(\mathbf{s})$  is modeled as a deterministic function in terms of the correlated process variable, and the residuals are modeled as a spatial process,  $w$ , with mean zero and variance  $\sigma^2 \rho(\phi)$ , where  $\rho(\phi)$  is the exponential correlation of the form  $\exp(-\phi \|\mathbf{s}_i - \mathbf{s}_j\|)$ , and the error,  $\varepsilon(\mathbf{s})$  is normally distributed with mean zero and variance  $\tau^2$ . The proposed model increases prediction accuracy and reduces the amount of HDM measurements needed.

- *Measurement system analysis for HDM:* An MSA procedure is needed to make certain that HDM systems are capable of measuring surface local variations with high repeatability. A framework is proposed which uses the surface data-process fusion model to effectively calculate the HDM system capability of capturing both global and local variations. In addition, a zone by zone Gage R&R is developed which detects the areas on the part where the gage is incapable.

- *Surface variation monitoring using HDM data:* A sequential monitoring framework is developed to monitor surface variations as reflected by HDM data. Based on the surface data-process fusion model, a progressive monitoring algorithm under a Bayesian framework is also developed to monitor surface variations when limited HDM measurements are available. The proposed methods are able to effectively monitor HDM data and locate defective part areas.
- *Multistage modeling and monitoring of HDM Data:* A morphing-based approach is proposed to model the multistage interdependence between downstream and upstream operations. A new multistage monitoring procedure is developed based on the morphing model which improves surface prediction accuracy when abnormal variations are present.

#### **1.4. Organization of Thesis**

The thesis is organized as depicted in Figure 1.6. Chapter 2 conducts modeling of surface data-process fusion using spatial and cross-correlation. Chapter 3 develops methods for measurement system analysis for HDM. Based on the data-process fusion model, Chapter 4 develops surface variation monitoring for (a) HDM data and (b) multi-resolution data when only limited HDM data is available. Chapter 5 models the multistage interdependence using a morphing-based methodology to monitor between stage surface variations. Chapter 6 concludes the thesis and outlines topics for future research.

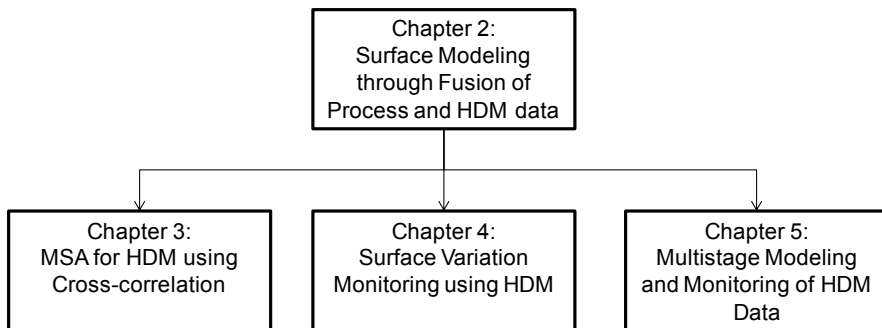


**Figure 1.6 Thesis Organization**

## CHAPTER 2

### SURFACE MODELING THROUGH FUSION OF PROCESS AND HDM DATA

HDM systems provide fine resolution measurements needed for the evaluation of process performance with micron-level accuracy. As observed in Chapter 1, obtaining a sufficient sample size of HDM measurements for process monitoring can be difficult since HDM systems are costly and the measurement is time-consuming. It might take a significant amount of time for an HDM system to measure a part, depending on the part size, the scanning speed, and the scanning technology employed. In addition, due to the high cost of HDM systems, manufacturers deploy fewer HDM machines in plant, further restricting the number of parts that can be measured. There is a strong need to develop an efficient strategy for HDM-based process control that addresses these challenges.

To enable HDM-based process control, it is desirable to combine the insights gained through HDM data with LDM measurements to decrease measurement time and cost. Thus, this chapter develops an approach for efficiently predicting surface variations by using both limited HDM measurements from preselected local regions and LDM measurements over the entire surface from an incoming part. Based on these combined measurements, we propose a method to predict spatial data at unobserved locations using

the cross correlations between the surface profile and process variables in conjunction with spatial correlation. The cross correlation patterns were reported for the first time by previous studies [1, 56] which showed that surface profile variations along certain directions are strongly correlated to process variables such as material removal rate. The process variables considered are usually less costly and more time-efficient to measure. Incorporating such cross correlations with these variables in a surface model can potentially reduce the number of HDM measurements needed for process control while maintaining prediction accuracy.

In this chapter, the existing cross correlations between the process variables and surface profile are first reviewed and illustrated. A data fusion surface prediction model is then established by using the cross correlation between the HDM data and machining process variables in conjunction with spatial correlation to improve surface prediction. A case study demonstrates the effectiveness of the proposed surface model.

## **2.1. Cross correlations uncovered by HDM systems**

Spatial correlation and cross correlation may be utilized to reconstruct the surface profiles revealed by the HDM data. The spatial correlation reflects the similarity among neighboring data points on the surface, while the cross correlation reflects the relationship between external process variables and the surface data. In a machining process, dominant cross-correlation patterns exist between surface height and material removal rate (MRR), i.e., the material removal volume per cutter revolution [1]. A change in MRR can cause cutting force variation and thus impact surface shape. Since the MRR is influenced by feed rate, arc length of cutter engaged in cutting, cutting insert

engagement and cutter path, and clamping, this section discusses different cross correlation patterns with these variables.

Cross correlation with cutting arc length. A previous study on HDM surface characterization reported a linear cross-correlation pattern between the average surface profile along the feed direction and the arc length of a cutter engaged in cutting [1]. For example, the HDM data of the deck face on the engine head in Figure 1.4 show that the surface profile is low where a bore is present and becomes high where more material is present (e.g., the bridge areas between cylinder bores). A correlation study was conducted to analyze the relationship between the average surface profile per cutting revolution and the material removal volume per cutter revolution, i.e., material removal rate (MRR). The MRR can be approximated by the arc length of a cutter engaged in cutting. Figure 1.4 shows that the average height of the part surface is positively correlated to the MRR or the arc length. Such a cross correlation is induced by the cutting force during machining, which was shown in [56] using a cutting force simulation based on a Third Wave Systems<sup>®</sup> package. The simulation revealed that due to surface discontinuities caused by surface geometry, the volume of removed material per cutting revolution (MRR) varies as the cutter moves along the feed direction. The MRR causes axial cutting force changes which generate the variations of the relative displacement between the work piece and cutter, resulting in surface height variations along the feed direction.

Cross correlation with cutting arc length. Figure 2.1 demonstrates the relationship between the surface height and the MRR. When the cutter is in position 1, less material is being removed than when the cutter is in position 2. A trace on the part shows that when

the cutter is at position 1, the surface height is low; when the cutter is in position 2, the surface height is high.

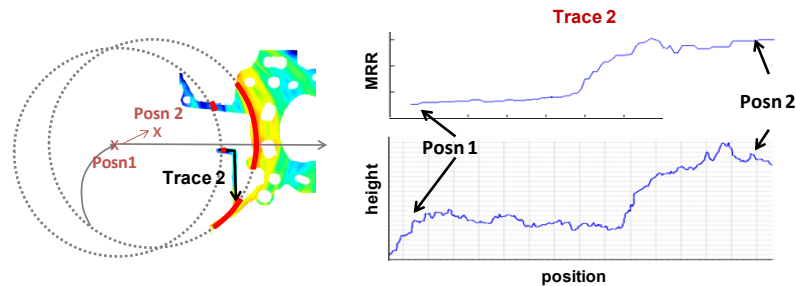


**Figure 2.1 Cross-Correlation between Surface Height and MRR [1]**

Cross correlation with cutting insert engagement Cross-correlation patterns also exist in the circumferential direction of the cutter. Figure 2.2(a) shows the profile of a machined planar surface where the color represents surface height. Figure 2.2(b)-(f) show the states of the cutter during one complete revolution. For example, in Figure 2.2(b), insert 1 is engaged in cutting, and as the cutter rotates clockwise, both insert 5 and insert 1 begin to be engaged in cutting as shown in Figure 2.2(c). The boundary between the zones with different grey scales in Figure 2.2(g) outlines the locations where the number of inserts engaged in cutting switches from 1 to 2 or from 2 to 1. The area where the number of inserts engaged in cutting switches from 1 to 2 (or equivalently where axial cutting force changes) in Figure 2.2(g) corresponds to a height change in the profile in Figure 2.2(a). Thus, the surface profile along the circumferential direction is correlated to the cutting force variation due to the different insert engagement.

Cross correlation with feed rate. Another type of MRR cross-correlation observed occurs between varying feed rate and the surface height. Figure 2.3 shows a close up of the tool-marks on an engine head surface. The spacing between the tool-marks are an indication of the feed rate; the larger the spacing, the faster the feed rate. In this example, the CNC

machine tool executes a different line of G-code, causing a dwell zone, where the spacings between the tool-marks are reduced by two thirds, indicating a feed rate slowdown. The decreased feed rate reduces axial cutting force generating smaller relative displacement between the cutting insert and workpiece and therefore creating a lower surface profile. Thus, the surface height is highly correlated with the feed rate or tooling mark spacings on the surface.

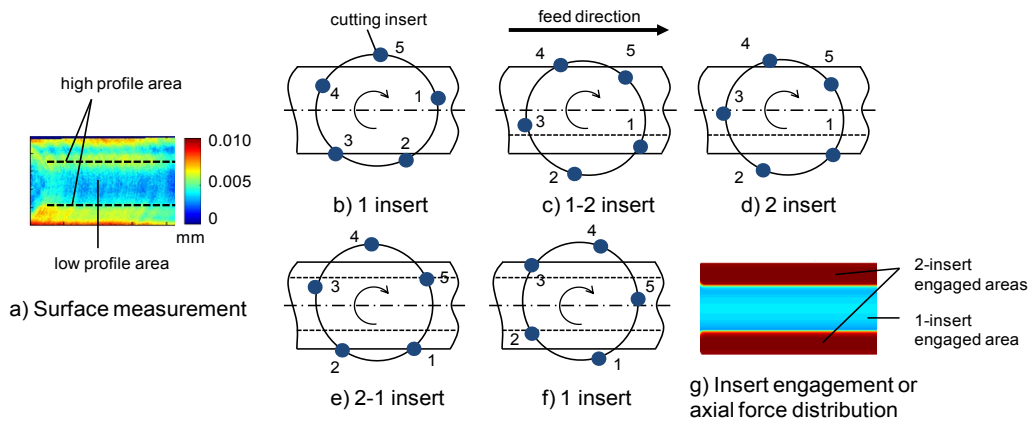


**Figure 2.2 Cross-Correlation: Surface Height vs. Cutter Insert Engagement [2]**

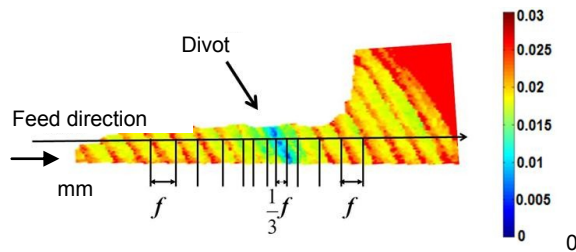


**Figure 2.3 Cross-Correlation: Surface Height vs. Feed rate or Tool Mark Spacing**

Cross correlation with clamping scheme. The surface profile is correlated to the clamping scheme including clamping layouts and force as shown in Figure 2.4. It can be seen that the surface height increases at locations where the clamping is applied. Such a pattern



results from cutting depth decrease at the clamped areas due to the clamping effect. The magnitude of the clamping torque is also positively correlated to surface height.

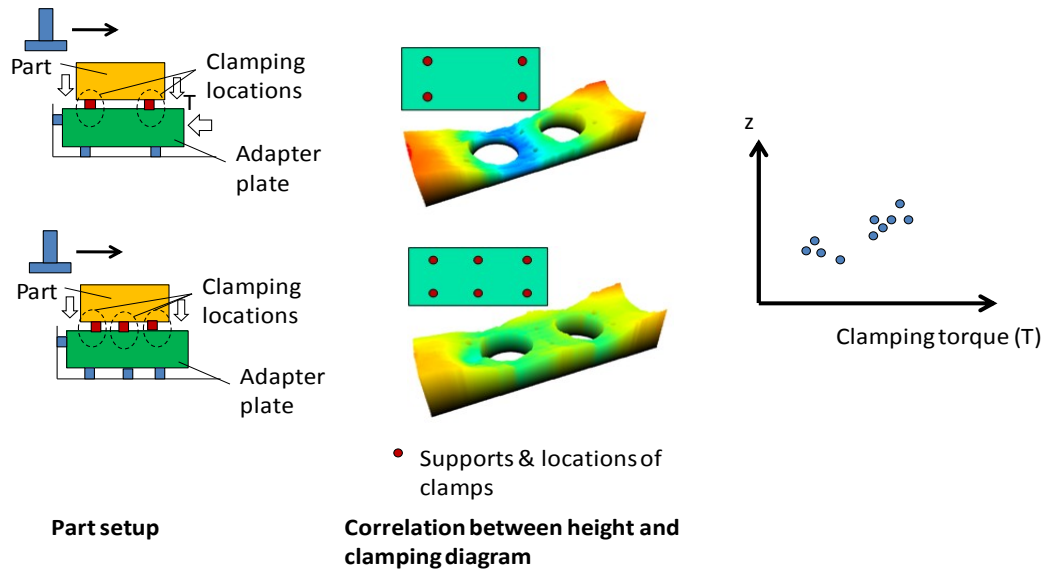


**Figure 2.4 Cross-Correlation: Surface Height vs. Clamping torque**

The above insight on the correlation patterns gained from HDM measurements can be used to improve the surface prediction accuracy. The remainder of this chapter uses the cross correlation between surface height and cutter arc length to demonstrate the prediction improvement.

## 2.2. Surface prediction considering spatial and cross correlations

A high resolution estimate of machine surface height can be predicted using the surface measurements along with process variables. The components used for the prediction are the reduced subset of HDM measurements, the spatial correlation between these HDM data and the cross-correlation between the HDM data and highly correlated process variables, such that

$$\mathbf{Z}(\mathbf{s}) = f(\mathbf{Z}(\mathbf{s}_0), \mathbf{U}_1(\mathbf{s}_0), \dots, \mathbf{U}_n(\mathbf{s}_0)) + \varepsilon \quad (2-1)$$

where  $Z(\mathbf{s})$  is the estimate of surface height at any location  $\mathbf{s}=(x_i, y_i)$ ;  $f$  is a function that reflects both the spatial correlation between the observed surface height measurements,  $Z$ , and the cross-correlation between the surface height and process variables;  $U_1(\mathbf{s}_0) \dots U_n(\mathbf{s}_0)$  are the observed measurements for  $n$  process variables at surface locations  $\mathbf{s}_0$ , and  $\varepsilon$  is the error. This dissertation refers to the surface height (the variable of interest) as the primary variable and the correlated process variable as the secondary variable.

A number of models could be proposed for the function  $f()$  to expand Equation 2-1 and estimate the  $Z(\mathbf{s})$  (the primary variable). Without losing generality, this dissertation uses the hierarchical Bayesian model as an example to illustrate the procedure [57]. The model inputs are:

- $\mathbf{Z}(\mathbf{s}_0)=[Z_1 \dots Z_i]^T$ , an  $i \times 1$  vector of observed measurements of the primary variable;
- $\mathbf{U}(\mathbf{s}_0)=[U_i^T(\mathbf{s}_0)]_{i=1}^p$ , an  $i \times p$  matrix of measurements with  $i$  observations for each of the  $p$  secondary variables.

The secondary variables  $\mathbf{U}$  are assumed to have a high correlation with the surface height and be cost-effective to measure. The inclusion of these secondary variables supplements the information provided by the primary variable, resulting in a more accurate estimate for the prediction variable. The estimate of  $Z$  can be calculated by

$$Z(\mathbf{s}) = \mu(\mathbf{s}) + w(\mathbf{s}) + \varepsilon(\mathbf{s}), \text{ where}$$

$$\begin{aligned}
\text{Mean} \quad & \mu(\mathbf{s}) = [\mathbf{1} \quad \mathbf{U}(\mathbf{s})^T] \boldsymbol{\beta} \\
\text{Covariance} \quad & w(\mathbf{s}) \sim \text{GP}(0, \sigma^2 \rho(\phi; \|\mathbf{s}_i - \mathbf{s}_j\|)) \\
\text{Error} \quad & \varepsilon(\mathbf{s}) \sim \text{N}(0, \tau^2)
\end{aligned} \tag{2-2}$$

The mean of the expression,  $\mu(\mathbf{s})$  is modeled as a deterministic function in terms of the correlated process variable, and the residuals are modeled as a spatial process,  $w$ , with mean zero and variance  $\sigma^2 \rho(\phi)$ , where  $\rho(\phi)$  is the exponential correlation of the form  $\exp(-\phi \|\mathbf{s}_i - \mathbf{s}_j\|)$ , and the error,  $\varepsilon(\mathbf{s})$  is normally distributed with mean zero and variance  $\tau^2$ .

Equations 2-1~2-2 are used to make surface height predictions on the spatial domain for a single part and establish the basis for surface monitoring, as will be discussed in Chapter 4.

### 2.3. Case Study

To demonstrate the advantages of using a secondary variable for surface prediction, the following section compares the predictions obtained using (a) one covariate, the spatial correlation between  $Z_{\text{HD}}$  and (b) two covariates, the spatial correlation between  $Z_{\text{HD}}$  and the cross-correlation between  $Z_{\text{HD}}$  and the MRR variable on a single surface. Figure 2.5 shows the model input data; for case (a) only the surface measurements are used, and for case (b) both the surface measurements and the MRR measurements at 3000 locations are used. The right panel shows the MRR, which was calculated as the total arclength of the part moving in the feed direction; i.e. the arclength is lower in the areas where the bores are present.

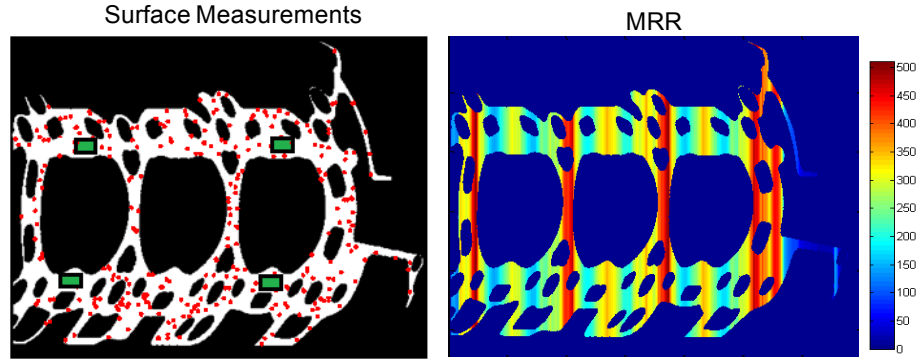


**Figure 2.5 Data Inputs for Data Fusion Surface Prediction**

The spatial relationships were modeled by Equations 2-1 ~ 2-2.

$$\begin{aligned}
 \beta &\sim \text{unif}() \\
 \phi &\sim \text{unif}(0.1,3) \\
 \sigma^2 &\sim \text{IG}(2,0.35) \\
 \tau^2 &\sim \text{IG}(2,1.04e-5)
 \end{aligned}
 \tag{2-3}$$

where  $\beta$ ,  $\phi$ ,  $\sigma^2$  and  $\tau^2$  are as described in Equation 2-2. Predictions are shown in Figure 2.6. The left panel shows the actual measurements, the middle panel the results from using only spatial correlation, and the right panel the results from using both spatial and cross-correlation. The predictions based on spatial correlation in case (a) produce a smoother surface compared to the actual surface. The addition of the cross-correlation information in case (b) captures local variation features, such as the peaks and valleys around the bores. The root mean square (RMS) improved from an RMS=0.008 in case (a) to RMS=0.003 in case (b), showing that the prediction using both spatial and cross-correlation is closer to the actual. The use of the MRR information at the prediction points improved the prediction accuracy significantly.

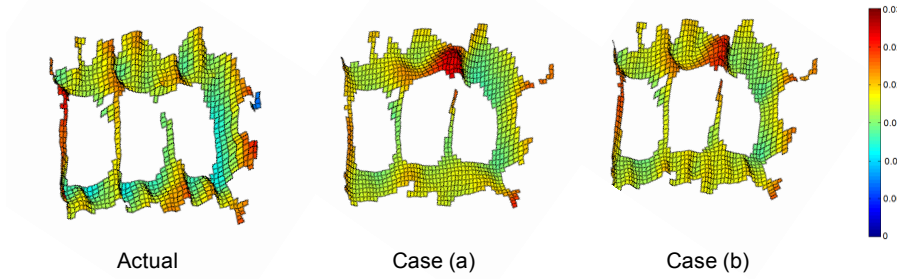


**Figure 2.6 Prediction Results**

To more clearly show the improvement of local variation prediction, a cross section of the parts in cases (a) and (b) are compared in Figure 2.7. In both panels, the actual measurement is in red, while the prediction is in blue. As seen in the figure, the prediction in case (b) is more accurate and better captures the local variation of the surface.

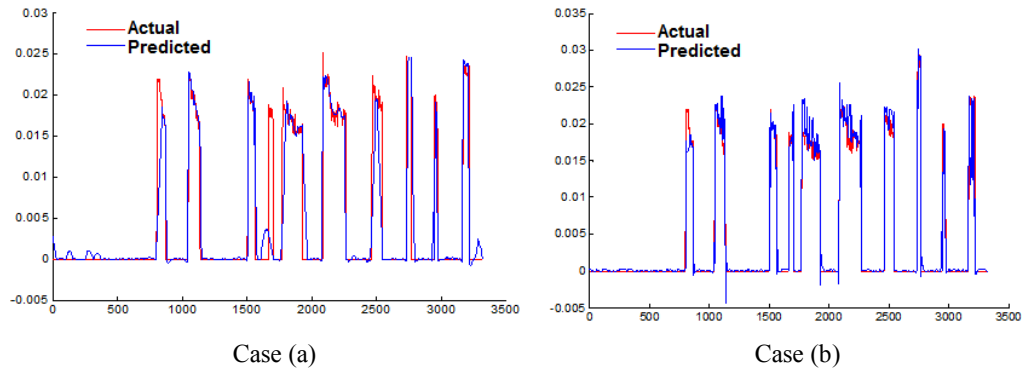


**Figure 2.7 Comparison Between Prediction Cross Sections**

## 2.4. Chapter Summary

HDM systems enabled the discovery of cross-correlations between process variables and the surface profile of a part in a machining process. In this chapter, examples of such cross-correlations were outlined, including the cross-correlation between the part surface and the MRR, arc length, feed rate and clamping scheme. A model was proposed to predict the surface data at unobserved locations by incorporating spatial correlation and

cross-correlations between the surface measurements and process variables in conjunction with limited HDM data and LDM data. A case study demonstrated that the proposed surface model is more accurate at predicting the surface local variations as compared to a spatial correlation surface model that does not include process information. The data fusion surface model thus enables HDM based process control by reducing the need for a large sample size of HDM data. The proposed data fusion model is the basis for the work presented in the subsequent chapters: engineering-driven MSA, process monitoring and multistage monitoring.

## **CHAPTER 3**

### **MEASUREMENT SYSTEM ANALYSIS FOR HIGH DEFINITION**

#### **METROLOGY USING CROSS-CORRELATION**

HDM technologies are increasingly being used in manufacturing plants to make inferences on product and process quality. Prior to utilizing an HDM system for process control in a manufacturing process, the system has to be deemed capable of measuring parts in a repeatable and reproducible fashion. Currently, industry practitioners use conventional capability indices designed for LDM systems on HDM systems. This chapter develops a new MSA method to improve the estimation of gage capability for HDM systems through an engineering driven, spatial clustering based method. A comparison between the proposed method and other commonly used approaches is provided.

The measured data from an HDM system usually is in the form of a data cloud comprised of individual points. Each point is identified by its 3-dimensional x-y-z coordinates. Two of the most common types of 3D measurement data for manufacturing processes are planar surfaces and 3D shell objects. Planar surfaces are measurements where each x-y location has only one associated z measurement; usually

these measurements can be converted into images in an x-y grid of measurements at each location. Figure 3.1(a) shows a planar measurement of an automotive engine head measured by a laser interferometry system, where the color indicates the height (z) measurement. Three-dimensional shell measurements are taken on the surface of an object, and typically each x-y location might have more than one associated z measurement. Figure 3.1(b) shows an example of a volumetric shell measurement of a generic part as measured by a scanner system.

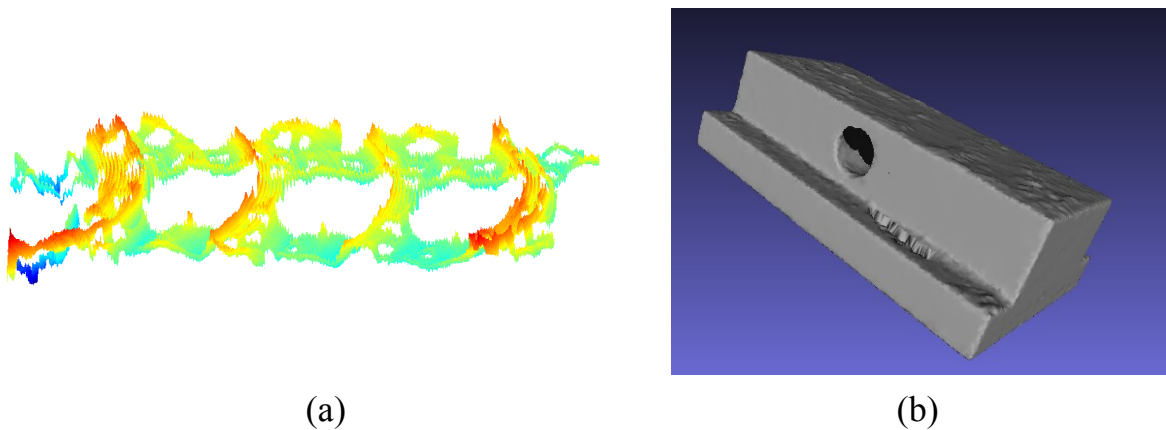


**Figure 3.1(a) 3D planar Measurement (b) Volumetric Shell Measurement**

Conventional methods to quantify the performance of a measurement system were developed based on LDM data. These methods use a few critical summary dimensional characteristics to calculate a system's capability, and might not accurately estimate the capability of an HDM gage at measuring local surface variations. For instance, Figure 3.2 shows the HDM measurements of the surface of two milled parts. A typical way of calculating the gage capability is to use the part surface flatness, which is the maximum minus the minimum observation in the data set. Both parts in Figure 3.2 have a surface flatness of approximately 30  $\mu\text{m}$ , but their local surface variations are dissimilar. An



MSA based on the surface flatness might incorrectly conclude that a gage is capable. Another less popular approach used in practice is to calculate the capability for each point individually (pointwise). For high dimensional HDM data, this calculation can become computationally intensive, particularly if each measurement has millions of points. In addition, HDM data can be highly auto-correlated, and performing an MSA without accounting for this correlation results in an overestimation of the %R&R [58]. Additional challenges of calculating the capability of data utilizing the pointwise method is that measurements utilizing the same HDM system on the same part might yield a different number of points per measurement, and these measurements may not have aligned x-y coordinates.

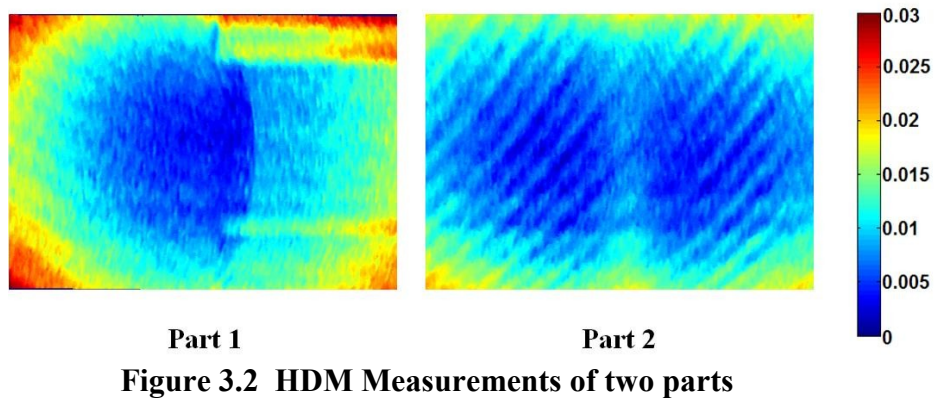


**Figure 3.2 HDM Measurements of two parts**

Thus, the challenges of using conventional MSA methods with HDM metrology systems may be summarized as follows: (1) global surface variations might mask local variations in conventional MSA methods resulting in inaccurate capability estimates, (2) the capability of the measurement system may be underestimated if the measurement points are highly autocorrelated, and (3) applying the MSA method pointwise is computationally intensive.

### ***State of the Art***

The most used MSA model calculates capability indices based on decomposing the total study variance into the various measurement system components [59-61], such that

$$\sigma_{meas}^2 = \sigma_{QC}^2 + \sigma_{gage}^2 \quad (3-1)$$

where  $\sigma_{meas}^2$  is the variance of the measurement of the observed quality characteristic,  $\sigma_{QC}^2$  is the variance of the true, unknown value of the quality characteristic, and  $\sigma_{gage}^2$  is the gauge error. Based on Equation 3-1, several indices have been developed to measure the capability of a gauge. One index that is often utilized is the P/T ratio as described in AIAG (2002),

$$\frac{P}{T} = \frac{k\hat{\sigma}_{gage}}{TOL}, \quad (3-2)$$

where  $k$  represents the sigma-multiplier ( $k = 5.15$  is usual), and  $TOL$  is the maximum specification minus the minimum specification limit as set by the plant. Usually, a P/T ratio of less than 10% is considered acceptable. Another index is the %R&R,

$$\%R \ \& \ R = \left( \frac{\sigma_{gage}}{\sigma_{meas}} \right) \times 100, \quad (3-3)$$

such that a system is considered capable if the %R&R is less than 33%. Finally, the signal-to-noise ratio (SNR) index which is a function of the %R&R is also used,

$$SNR = \left( \frac{\sigma_{meas}}{\sigma_{gage}} \right) \sqrt{2}. \quad (3-4)$$

A measurement system is considered capable if the SNR is less than five.

To estimate the variation components  $\sigma_{meas}$ ,  $\sigma_{gauge}$  and  $\sigma_{total}$  in a two-factor experiment, a two-way ANOVA may be used [61, 62]. The experiment involves  $o$  operators measuring  $p$  parts  $n$  times each, such that

$$Y_{ijk} = \mu + O_i + P_j + OP_{ij} + \varepsilon_{ijk}, \quad (3-5)$$

where  $Y_{ijk}$  is an individual measurement performed by operator  $i$  ( $i = 1 \dots o$ ), measuring part  $j$  ( $j = 1 \dots p$ ) for the  $k^{th}$  time ( $k = 1 \dots n$ );  $\mu$  is the overall mean,  $O_i$  is the effect of the  $i^{th}$  operator,  $P_j$  is the effect of the  $j^{th}$  part,  $OP_{ij}$  is the interaction effect of the operator and part, and  $\varepsilon_{ijk}$  is the normally distributed error term. While this method is straightforward and intuitive, it only assesses the capability of the system to measure one particular quality characteristic. Thus, practitioners often have individual %R&R requirements for each dimensional measurement, such that there are as many capability ratios as there are quality dimensions.

Previous researchers have addressed the challenges for dealing with the high dimensionality of HDM data using different strategies. Majeske [58] proposed using the multivariate generalization of ANOVA, MANOVA, to calculate the capability indices. The framework works well in instances where the number of parts measured,  $p$ , is greater than the number of quality characteristics measured on each part,  $m$ . However, when  $m \gg p$  there are not enough degrees of freedom to estimate the error term, covariance matrices become singular and the variance components cannot be estimated. This type of high-dimensional scenario where  $m \gg p$  is typical when analyzing HDM and image data where each point may count as a quality characteristic.

Recent work has focused on reducing data dimensionality prior to performing the MSA, which usually fits models to the multidimensional data and measures the capability of the system using the fitting coefficients [63, 64]. However, these methods are not performed directly on point data clouds and some of the local information from the between part variability may be lost when fitting coefficients. Researchers have also explored multivariate multisite capability testing using principal components [65] and factor analysis [66].

Most multivariate MSA methods rely on MANOVA to decompose gage variation. However, MANOVA is difficult to use with multivariate data where the number of dimensions is larger than the number of observations. Most of the research on MANOVA for high dimensional data is divided into two categories; the first tries to find high-dimensional approximations to the MANOVA test statistic [67]; the second tries to reduce the high-dimensional data by selecting the most significant features [59, 68, 69].

A cohesive methodology is needed to assess the capability of a high dimensional, point cloud measurement system that addresses the previously listed challenges. In this chapter, a method is developed to estimate the capability of HDM gages at measuring the global and local variations of multidimensional data. In addition, the method is able to locate the areas of the gages that are not capable, thus aiding in gage diagnosis and calibration. This chapter: (1) proposes an improved engineering-driven interpolation method that improves MSA estimation, (2) develops a spatial clustering based MSA method to calculate zone by zone gage capability, and (3) provides a comparison of several data reduction methods to perform MSA using HDM data.

The rest of the chapter is organized as follows: section 3.1 describes proposed method for high dimensional MSA. In section 3.2, the method is demonstrated using a generic part and 3D sphere measurements. Section 3.3 discusses the advantages and disadvantages of various data reduction approaches in high-dimensional MSA and section 3.4 concludes the chapter.

### 3.1. Proposed Framework for High Dimensional Multivariate MSA

The proposed method for high-dimensional multivariate MSA focuses on applying multivariate MSA to reduced and regularized data as shown in

Figure 3.3. The first three steps address the measurement, registration and interpolation of the data to transform all measurements to the same coordinate frame. The part measurement size needs to be reduced in step 4 such that the multivariate MSA procedure can be applied in step 5. Each of these steps is discussed in the following subsections in more detail.

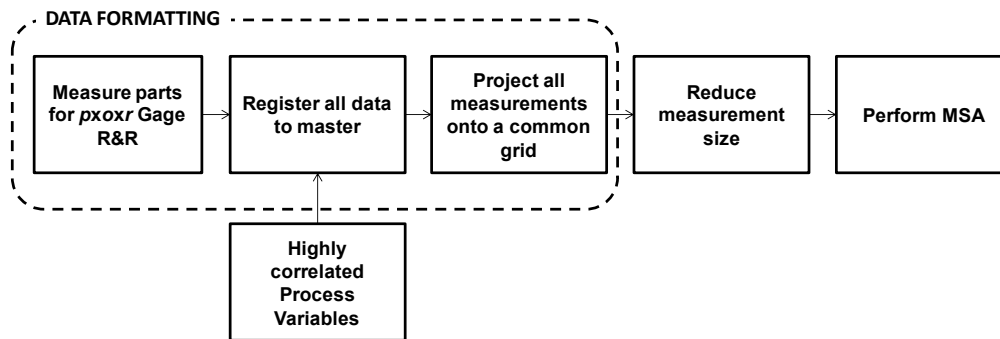
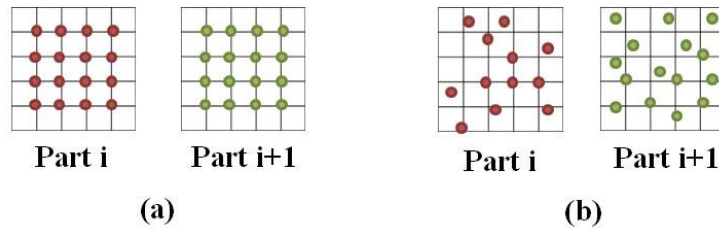


Figure 3.3 Proposed Measurement System Analysis Framework

#### 3.1.1. HDM Data Regularization using Spatial and Cross-Correlations

HDM data pre-processing might be required prior to performing MSA analysis. Ideally, HDM data obtained from repeated measurements on the same part should

produce the same number of points, where each point has the same x-y location in the same coordinate frame across measurements, as illustrated in Figure 3.4(a). However, HDM systems do not necessarily produce an equal number of data points for each measurement. As shown in Figure 3.4(b), HDM systems may produce a different number of points in different x-y locations. Thus, to facilitate the comparison of the data, two data regularization steps might be needed before performing an MSA on an HDM measurement system: (1) data registration and (2) data interpolation.



**Figure 3.4 (a) Regularized Part Measurements (b) Point Cloud Part Measurements**

### ***3.1.1.1. HDM Data Registration***

A set of HDM point cloud measurements is unregistered when one or more of the measurement's x-y coordinates are not aligned with the others. To facilitate the comparison between the measurements, the HDM data needs to be registered, such that a mapping function which scales, rotates and translates the points between the measurements is established. The mapping functions considered in this paper consist of affine transformations that estimate the rotation and translation between two parts. As the measurement system is measuring the same part repeatedly, it is assumed that the measurement data will have negligible deformation such that the scaling effect can be ignored. A review of registration methods for image data can be found in [70]; for 3D point clouds in [71, 72].

A general rigid-body registration approach is briefly reviewed. Denote two different measurements of the same part as  $A$  and  $B$ , with each measurement having a corresponding coordinate frame,  $C_A$  and  $C_B$  respectively. Further denote the points  $\mathbf{Z}_A = [x_A \ y_A \ z_A]$  and  $\mathbf{Z}_B = [x_B \ y_B \ z_B]$ , which are corresponding points measuring the same feature in measurement  $A$  and  $B$ . Then a transformation,  $T$ , may be found such that

$$\mathbf{Z}_B = \mathbf{R}_{AB} \mathbf{Z}_A + \mathbf{t}_{AB}, \quad (3-6)$$

with an objective function

$$\min_{\mathbf{R}, \mathbf{t}} = \sum_{i=1}^N \mathbf{Z}_{B_i} - (\mathbf{R}_{AB} \mathbf{Z}_A + \mathbf{t}_{AB}), \quad (3-7)$$

where  $\mathbf{R}_{AB}$  is a  $3 \times 3$  rotation matrix and  $\mathbf{t}_{AB}$  is a  $3 \times 1$  translation vector transforming point  $\mathbf{Z}_B$  into the reference coordinates of  $\mathbf{Z}_A$ .

Various closed form and iterative methods have been developed to determine the  $\mathbf{R}_{AB}$  and  $\mathbf{t}_{AB}$  matrices. A comparison of commonly used closed form methods based on feature (surfaces, lines, or points) correspondence is found in [73]. For cases where it is desirable to estimate the rotation and translation by minimizing the distance between the measurement data clouds, the iterative closest point (ICP) algorithm may be used [74-76]. ICP seeks to minimize the distance between the points in each measurement, and has been found to be an efficient way to find local minima. Given two point data clouds,  $\{P_i\}$  and  $\{Q_i\}$ , the following objective function is minimized

$$f(R, t) = \frac{1}{N} \sum \|p_i - |\mathbf{R}(q_i) - \mathbf{t}|\|, \quad (3-8)$$

where  $p_i$  and  $q_i$  are points corresponding to data clouds  $\{P_i\}$  and  $\{Q_i\}$ ,  $N$  is the total number of pairs in the data sets,  $\mathbf{R}$  is the rotation matrix, and  $\mathbf{t}$  is translation vector. The ICP algorithm is widely used due to the ease of implementation.

### 3.1.1.2. HDM Data Interpolation using process-data fusion model

Data interpolation is the process by which the data at unobserved locations is estimated. The purpose of the data interpolation when doing an MSA is to regularize the different measurements onto the same grid such that they can be compared. Figure 3.5 shows an example of scattered data points ( $z_i$ ) and interpolation estimates ( $z'_i$ ) that can be at the lattice points.

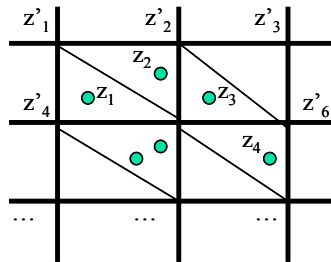


**Figure 3.5 Projection of Scattered Data onto Grids**

Prior to interpolation, the number and location  $(i_p, j_p)$  of the prediction points,  $\hat{Z}(i_p, j_p)$ , should be determined. To establish the location of the prediction points, it is recommended to overlay all of the registered measurements taken for the MSA experiment, and find the outer points for all of the combined locations. For planar surfaces, a lattice can be established between the boundary points at the edges of measurements, such as the one shown in Figure 3.6, and the prediction locations placed on the corners of the lattice. The lattice spacing should be determined by the desired measurement resolution. It is recommended that that the lattice spacing is greater than the



precision of the gauge such as to not extrapolate data to a higher precision than the gauge's capability. In addition, Nyquist theory indicates that the spacing should be at least half of the smallest measurement feature that needs to be captured by the gage.

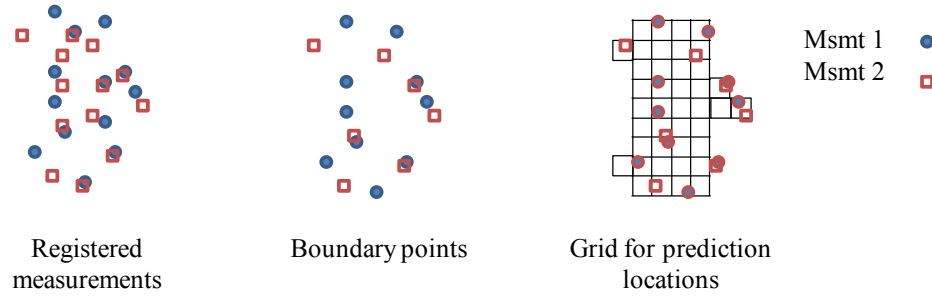


**Figure 3.6 Procedure for Identifying Prediction Locations**

### 3.1.1.3.HDM Data Interpolation using Spatial and Cross-Correlations

The surface model for the fusion of HDM and process data proposed in Chapter 2 can be used to improve the accuracy of the interpolated planar and volumetric measurements, such that

$$\hat{Z}(i_p, j_p) = f(Z(i_o, j_o), U_1(i_o, j_o), \dots, U_n(i_o, j_o)) + \varepsilon. \quad (3-9)$$

The estimate,  $\hat{Z}$ , can be calculated by using Bayesian Kriging such that

$$Z(i_p, j_p) = \mu(i_p, j_p) + w(i_p, j_p) + \varepsilon(i_p, j_p), \text{ where}$$

$$\begin{aligned} \text{Mean} \quad & \mu(i_p, j_p) = [\mathbf{1} \quad \mathbf{U}(\mathbf{s})^T] \boldsymbol{\beta} \\ \text{Covariance} \quad & w(i_p, j_p) \sim \text{GP}(0, \sigma^2 \rho(\phi; \|\mathbf{s}_i - \mathbf{s}_j\|)) \\ \text{Error} \quad & \varepsilon(i_p, j_p) \sim \text{N}(0, \tau^2) \end{aligned} \quad (3-10)$$

The mean of the expression,  $\mu(i_p, j_p)$  is modeled as a deterministic function in terms of the correlated process variable, and the residuals are modeled as a spatial process,  $w$ , with

a mean of zero and variance of  $\sigma^2\rho(\phi)$ , where  $\rho(\phi)$  is the exponential correlation of the form  $\exp(-\phi \|\mathbf{s}_i - \mathbf{s}_j\|)$ , and the error,  $\varepsilon(i_p, j_p)$  is normally distributed with a mean of zero and variance of  $\tau^2$ . By incorporating the information from process physics to adjust the measurement predictions, the accuracy at measurement areas where there are fewer observations (such as at the edges of the measurement) can be improved.

If there is no highly correlated process information available, many interpolation methods may be used, most of which estimate the data at a prediction location using the measurements in its vicinity. Two commonly used methods are Kriging and triangular interpolation. Kriging is a linear least squares estimator commonly used in the geostatistical field to estimate values at unobserved locations through establishing a spatial relationship between the points in the data cloud [77, 78]. Triangular interpolation seeks to estimate lattice data on grids, and at each grid corner the prediction is calculated from a few of its locally observed measurements [79]. Comprehensive reviews on different interpolation algorithms can be found in [80, 81].

*Note:* For volumetric shell objects, the object should be partitioned prior to engineering driven interpolation. Most interpolation techniques rely on calculating the point estimate by using local information. However, volumetric measurements may have multiple z-height values for the same x-y locations, distorting the interpolation results. Thus, it is necessary to partition the object such that only one z-height value is associated with each x-y location. For example, Figure 3.7 shows a half shell partitioned into four different sections using the x-y-z planes as guides.

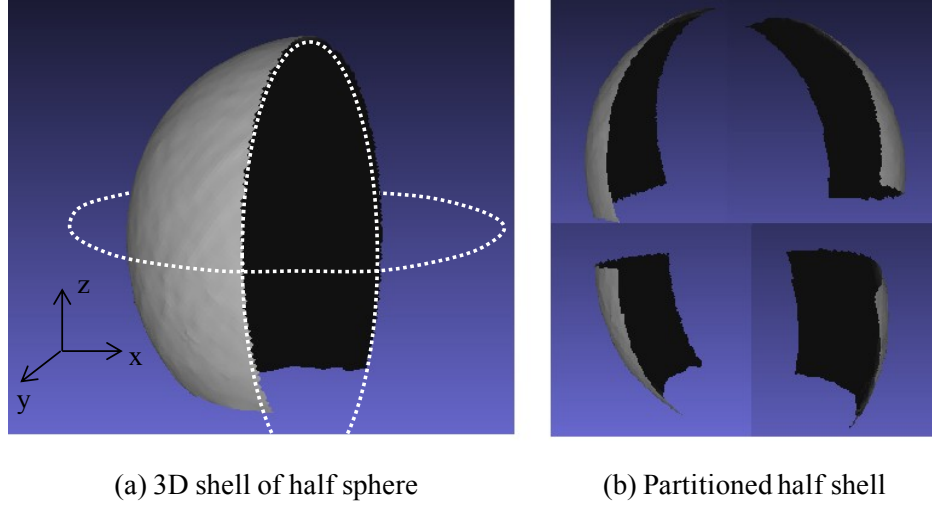


**Figure 3.7 Volumetric Shell Object Partition for Interpolation**

### 3.1.2. MSA for HDM

Data reduction is necessary after the data pre-processing. Different data reduction techniques may be useful depending on the nature of the measurement. In this section we briefly review two approaches which are applicable across a number of fields, and which have proved successful in decreasing data size while retaining local variation information.

The first approach is data reduction through Principal Components Analysis (PCA), which converts data points into variables (or principal components) that are linear combinations of the points [82]. For a data cloud  $\mathbf{Y}=[Y_1 \dots Y_m]$ , its  $i^{\text{th}}$  principal component is defined as

$$PC_i = \sum_{i=1}^m a_i Y_i, \quad (3-11)$$

where the  $a$ 's are constants which minimize the variation of  $Z$ . Thus the data cloud  $\mathbf{Y}$  can be represented using  $pc$  number of principal components which account for a large portion of the variation in the data, such that  $pc \ll m$ .

A PCA decomposition may be applied to the data by rearranging the  $K$  images of size  $M \times N$  into a single  $K \times MN$  matrix, such that each row of the matrix represents an image. Equation 3-11 can be used on  $K \times MN$  matrix to find the principal components of the variation between the images. After the PCA decomposition, the resulting eigenvectors can be reverted back into  $K$  images to visualize the spatial variation corresponding to each principal component. Recently, a 2D PCA method was proposed [83] which may also be used for image feature extraction and data reduction. The 2D PCA method may be more computationally efficient than PCA, however, the use of more coefficients per image is required.

The second reduction approach is to use spatial clustering algorithms. These algorithms seek to segment a data cloud into clusters, each cluster composed of similar points. Common clustering models include distance based models (such as hierarchical clustering), center based models (such as k-means or k-medoid) and distribution based models. These algorithms differ in terms of the clustering criteria and efficiency. In this dissertation, the K-means approach is used, but any spatial clustering method can be effectively used within the proposed framework.

After the data has been reduced, the methodology utilizes the framework proposed in [58] on the registered, interpolated, and reduced data. Majeske's model for a three factor model is

$$\mathbf{Y}_{ijk} = P_i + O_j + PO_{ij} + \varepsilon_{ijk}, \quad (3-12)$$

where  $\mathbf{Y}_{ijk} = [Y_1 \dots Y_1]$  is the  $k^{th}$  multivariate measurement of part  $i$  and operator  $j$ . The model is analyzed using Multivariate Analysis of Variance (MANOVA), and the %R&R,

P/T ratio and SNR derived. The framework works well for the reduced data; however it is important to note that in a  $p$ -dimensional MANOVA, there is a probability that the difference between the between-group mean squares and the within-group mean squares will be negative, thus resulting in negative estimates of variance components. A common approach to dealing with negative variance components is to set them to zero and estimate the within-group components by using the pooled mean squares. An alternative approach proposed by Amemiya derives covariance matrix estimators that are always proper [84].

### 3.2. Case Studies

Measurement system analyses for a complete set of combinations from two HDM measurement systems, three data reduction methods and three data sets were compared, as summarized in Table 3.1.

**Table 3.1. MSA Case study Analysis Methods and Data Set Summary**

Measurement system	High dimensional MSA method	Data set
1. Laser interferometry	1. Pointwise	1. Normal process (original meas.)
2. Laser scanner	2. PCA reduction	2. Large operator effect (simulated meas.)
	3. Spatial clustering	3. Large gage effect (simulated meas.)

The measurement systems tested were a planar HDM laser interferometer and a volumetric HDM scanner. An initial data set was obtained from a normal process using a  $2 \times 2 \times 3$  Gage R&R experiment for both metrology systems. A data set with a large

operator effect (operator variance increase of 20%) and one with a large gauge effect (gauge variance increase of 30%) were simulated. After the measurement data was interpolated, the MSA method described in the previous section was used to assess the capability of the gauge using the individual points (pointwise), PCA reduced data and spatial clustering.

### 3.2.1. Planar Measurements MSA

The planar HDM system tested was a laser holographic interferometer, with a measurement area of 300 mm<sup>2</sup>, an x-y resolution of 150 μm and z height resolution of 1 μm. Measurements from this system are high dimensional and can be up to 4M points. Sample measurements from such a system can be seen in Figure 3.1(a) and Figure 3.2. A two-factor high dimensional multivariate Gauge R&R study was conducted on the laser interferometry system, where two operators measured two parts three times each. Surface measurements of the milled top surface of two generic aluminum parts were used for the analysis, as seen in Figure 3.8. The overall global shape pattern for both parts shows a similar global variation but different local variations.

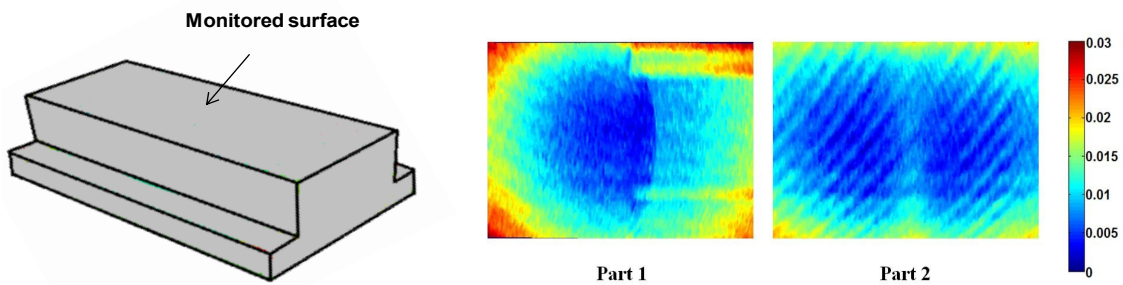


**Figure 3.8 Sample Planar Measurements used for Laser Interferometer MSA**

Although the 12 measurements did not require registration due to the nature of the measurement system, the original measurements consisted of data clouds of size ranging

from 8500 to 9000 points. As process information was not available, B-spline interpolation was used to regularize the measurements to 8000 points each at pre-selected rectangular grid locations.

### ***3.2.1.1. Pointwise MSA***

An individual MSA analysis was performed on each of the 8000 points in the planar surface measurement using conventional ANOVA analysis methods, as can be found in [62]. The results for the normal process data shown in Figure 3.9(a) demonstrate most of the measurement points have a passing %R&R, but towards the center of the parts the %R&R is close to 100%. After closer examination, there is negligible variation in the center area between the 12 measurements. This very small part variation (approximately 1 micron) resulted in a failing %R&R in the center areas. The simulated increased operator variation and gauge error result in an increased %R&R, as expected. The large operator variance depicted %R&R in Figure 3.9(b) shows a spatial pattern which might be explained by operator differences in measuring. Figure 3.9(c) which illustrates %R&R for the data with large gauge variation has no discernible spatial pattern; thus we can conclude that the gauge variation has increased evenly over the whole measurement area of the part.

### ***3.2.1.2. PCA based MSA***

PCA was applied to the planar surface measurements, and the PCA scores used to evaluate the measurement system. Figure 3.10 shows the normal process images decomposed into the first three principal components. As can be seen from the images, most of the variation in the measurements can be explained by using the first principal

component, which accounts for 99.8% of the variation of the data. This is explained by the marked difference between the two original part surfaces as seen in Figure 3.8, such that the part variation was higher than the measurement repeatability and reproducibility. The second and third principal components appear to be random noise and have no discernible spatial pattern.

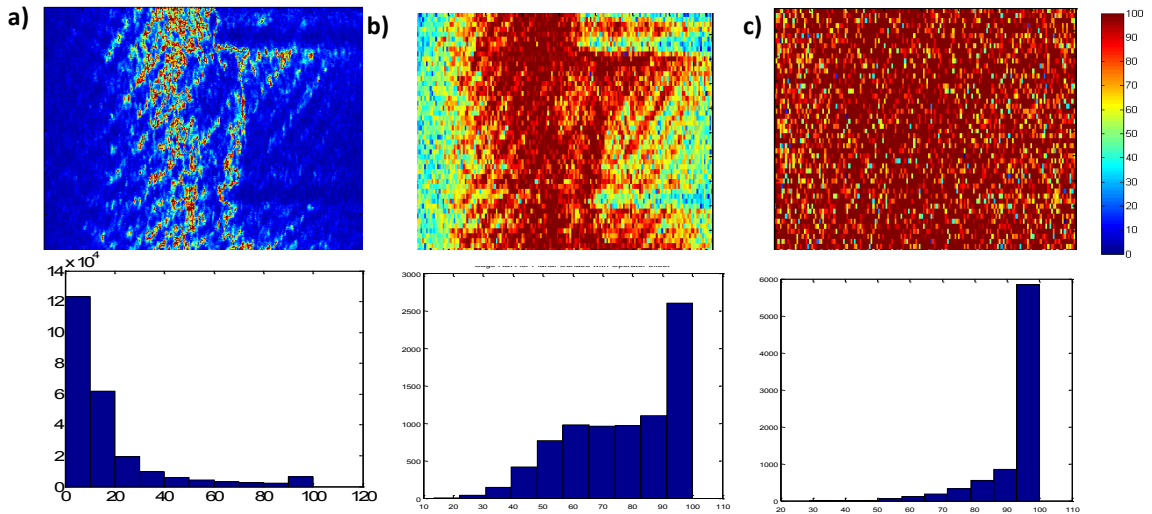


**Figure 3.9 %R&R values and %R&R distribution for (a) Measurements for a Normal Process (b) Measurements with a Large Operator Effect, and (c) Measurements with Large Gauge Error**

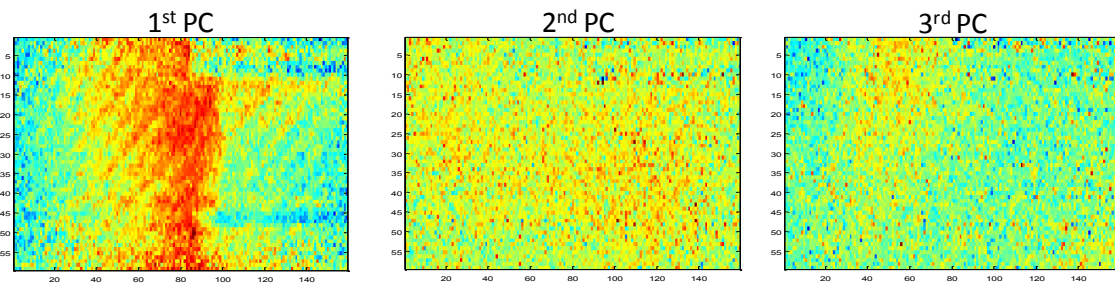


**Figure 3.10 First three 2-D Principal Components of Planar Measurements**

Using the PCA reduction method, the %R&R was 3.97%, which is much decreased from the estimates using the pointwise method. This decrease might be attributed to the noise present in the point by point MSA, where outliers are more likely to affect the



individual calculations. The %R&R for the measurements with the simulated operator and gauge errors were calculated using the corresponding PC's that attributed for at least 90% of the variation, which are summarized in Table 3.2. As expected, the simulated operator effect increased the %R&R to 53.4%, while the gauge error increased the %R&R to 70.9%.

**Table 3.2 Eigenvalues for Parts, Measurement and Gauge Covariance Matrices for Planar Measurements**

No.	Normal			Operator effect			Gage effect		
	Part	Gage	Meas.	Part	Gage	Meas.	Part	Gage	Meas.
1	3.8190	0.0096	3.8240	0.1336	0.0014	0.2066	0.4140	0.0000	0.4140
2	-	-	-	0.0000	0.1089	0.1090	0.0000	0.3560	0.3560
3	-	-	-	0.0000	0.0683	0.0686	0.0000	0.7700	0.7700
4	-	-	-	0.0000	0.0688	0.0688	0.0000	1.5990	1.5990
5	-	-	-	-	-	-	0.0000	1.7680	1.7680
6	-	-	-	-	-	-	0.0000	1.6270	1.6270
7	-	-	-	-	-	-	0.0000	1.6530	1.6530
8	-	-	-	-	-	-	0.0000	1.6750	1.6750
9	-	-	-	-	-	-	0.0000	1.7020	1.7020
10	-	-	-	-	-	-	0.0000	1.7230	1.7230

### 3.2.1.3. Spatial clustering MSA

The K-means clustering algorithm was applied to an average part calculated from the study measurements to separate the measurement data into similar clusters. The characteristics used for the clustering were the mean and standard deviation at each of the measurement locations. The resulting clustering scheme which separated the normal process data into 11 spatial clusters is seen in Figure 3.11(a), where each color represents a different cluster. The resulting clustering schemes for the measurements with a large operator and gauge effect can be seen in Figure 3.11(b) and (c) respectively.

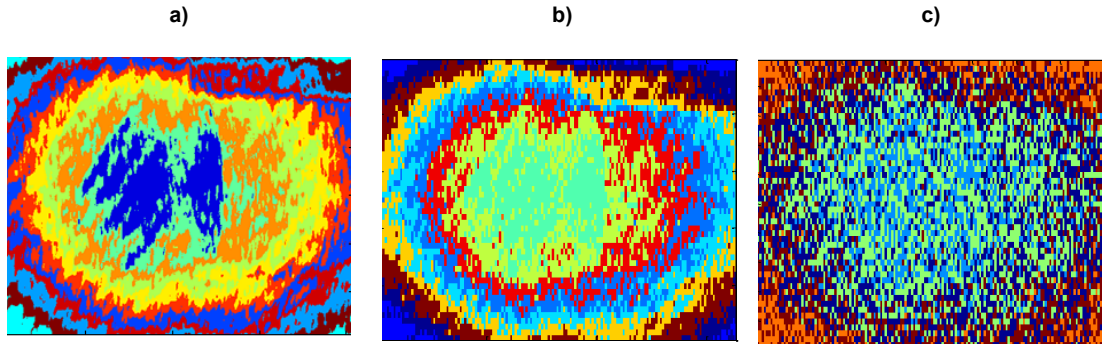


**Figure 3.11 Spatial Cluster Scheme on HDM measurements using K-means Algorithm with (a) normal process Measurements (b) Measurements with an Operator Effect (c) Measurements with a Gauge Error**

The clustering scheme was then applied to each of the part measurements and the %R&R and P/T ratio calculated from the cluster averages are shown in Table 3.3. The results are similar to the pointwise MSA method, as the center cluster (denoted in blue in Figure 3.11) has a very high %R&R percentage of 83%. However, the P/T ratio for cluster 1 is low at 1.83%, thus indicating that the low part variability in the center region of the part measurements is the reason for the high %R&R.

**Table 3.3 Gauge %R&R and P/T ratio for Planar Measurement Spatial Clusters**

Cluster	Normal		Operator effect		Gage effect	
	%R&R	P/T	%R&R	P/T	%R&R	P/T
1	<b>83.04</b>	0.037	<b>98.7</b>	1.20	29.26	0.19
2	5.11	0.051	<b>94.3</b>	1.26	21.28	0.18
3	5.00	0.037	<b>51.7</b>	1.22	16.82	0.18
4	4.13	0.045	<b>68.3</b>	1.22	<b>75.48</b>	0.21
5	18.26	0.084	<b>79.8</b>	1.19	<b>45.66</b>	0.17
6	6.22	0.094	<b>89.3</b>	1.28	-	-
7	5.53	0.028	<b>59.4</b>	1.20	-	-
8	6.72	0.043	<b>74.4</b>	1.20	-	-
9	4.96	0.048	<b>84.3</b>	1.21	-	-
10	5.24	0.031	<b>64.4</b>	1.12	-	-
11	4.74	0.0529	-	-	-	-

### 3.2.2. Volumetric Shell Measurements MSA

The volumetric HDM system utilized for the study was a 3D laser scanner with a 0.05 mm resolution, up to a 0.04 mm accuracy and stand-off distance of 300 mm. This system is utilized to measure volumetric shell objects, such as that observed in Figure 3.1(b). Depending on the size of the object, measurements from the scanner may result from thousands to millions of observations.

A two-factor high dimensional multivariate MSA study was performed on a 3D scanner, where two operators measured two parts three times each. Two flat-bottomed spheres with a 2” diameter were scanned. Prior to the %R&R analysis, the two parts were in different reference frames, as seen in Figure 3.12. To register the measurements, a rigid body ICP algorithm was used. The measurements were then regularized via triangular interpolation at 5000 predetermined sphere locations on a mesh.

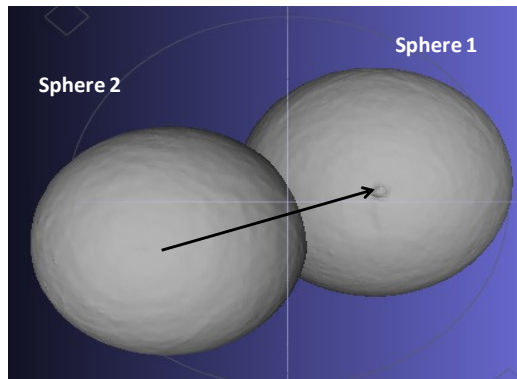


**Figure 3.12 Volumetric Part Measurements from Laser Scanner**

#### 3.2.2.1. Pointwise MSA

An individual MSA was performed on each of the 5000 measurement points of the spheres. The resulting %R&R distributions are depicted in Figure 3.13 for each of the three measurement data sets.

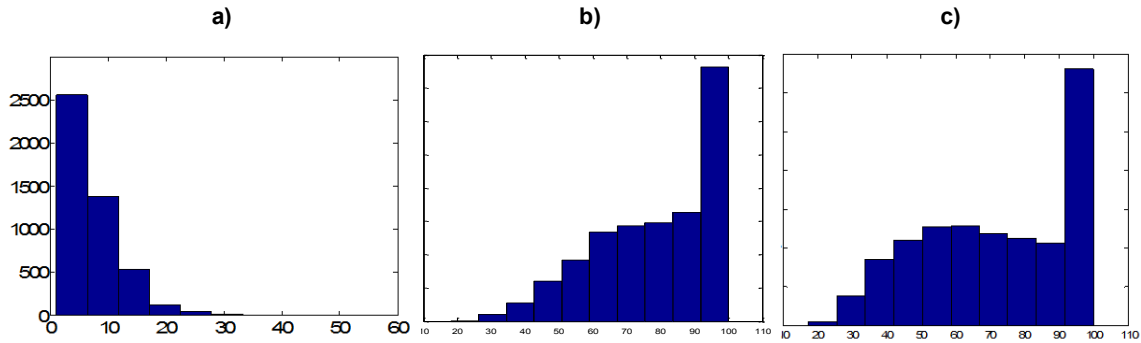


**Figure 3.13 %R&R distributions for (a) Normal Process Measurements (b) Measurements with Operator Effect and (c) Measurements with Gauge Effect**

As expected, the distributions for the measurements with simulated operator and gauge effects are highly skewed left, with the majority of the %R&R being 100%. The median %R&R was 10.3% for the normal parts data set, 75.2% for the data set with the simulated operator effect and 71.3% for the data set with the simulated gauge effect.

### **3.2.2.2. PCA based MSA**

The sphere data was reduced using PCA prior to performing the %R&R analysis, and the resulting eigenvalues from the MSA analysis shown in Table 3.4 for the three data sets.

The corresponding %R&R values were 9% for the normal process measurements, 20.4% for the measurements with the large operator effect, and 80.1% for the measurements with the large gauge effect. It can be seen from the table that the increased operator effect is reflected in the larger gauge variance components in the first PC, the direction with the most variation. However, the large gauge effect is reflected in an increase in the number of PC's, all with a large gauge variance component.

**Table 3.4 Eigenvalues for Parts, Measurement and Gauge Covariance Matrices for Volumetric Measurements**

No.	Normal			Operator effect			Gage effect		
	Part	Gage	Meas.	Part	Gage	Meas.	Part	Gage	Meas.
1	90.46	0.74	91.2	0	8.37E+4	9.1E+4	1.5E+05	4.1E+00	1.5E+05
2	-	-	-	6.6E+4	0.01E+4	6.8E+4	0.0E+00	8.0E+04	8.0E+04
3	-	-	-				0.0E+00	9.6E+04	9.6E+04
4	-	-	-				0.0E+00	3.3E+05	3.3E+05
5	-	-	-	-	-	-	0.0E+00	3.2E+05	3.2E+05
6	-	-	-	-	-	-	0.0E+00	3.2E+05	3.2E+05
7	-	-	-	-	-	-	0.0E+00	3.1E+05	3.1E+05
8	-	-	-	-	-	-	0.0E+00	3.1E+05	3.1E+05
9	-	-	-	-	-	-	0.0E+00	3.0E+05	3.0E+05
10	-	-	-	-	-	-	0.0E+00	3.0E+05	3.0E+05

**3.2.2.3.Spatial Clustering based MSA**

Spatial clusters were determined using the K-means algorithm using the average and standard deviation at each measurement point as the clustering characteristics. The resulting %R&R and P/T calculations are shown in Table 3.5 for each cluster. The values indicate that again the operator effect and gauge effect increase the %R&R.

**Table 3.5 %R&R and P/T Ratio for Volumetric measurement Spatial Clusters**

Cluster	Normal		Operator effect		Gage effect	
	%R&R	P/T	%R&R	P/T	%R&R	P/T
1	10.761	0.037	<b>64.75</b>	64.75	20.80	0.24
2	2.423	0.051	<b>96.62</b>	96.62	18.03	0.44
3	2.834	0.037	<b>80.36</b>	80.36	<b>48.22</b>	0.39
4	2.871	0.045	<b>65.26</b>	65.26	22.46	0.38
5	3.175	0.084	<b>93.91</b>	93.91	27.03	0.40
6	7.831	0.094	<b>44.26</b>	44.26	<b>63.72</b>	0.39
7	3.75	0.03	<b>58.14</b>	58.14	-	-
8	3.05	0.04	<b>89.19</b>	89.19	-	-
9	2.68	0.05	<b>50.97</b>	50.97	-	-
10	6.31	0.03	<b>67.42</b>	67.42	-	-

### 3.3. Discussion

This section discusses the advantages and disadvantages of using different reduction methods as explored in the case studies.

*Pointwise MSA.* This method is the most intuitive for practitioners, as it is based on current industry practices. However, its main drawback is that it is very computationally inefficient due to the high dimensionality of HDM measurements. In addition, HDM data often exhibits autocorrelation patterns, which can result in the overestimation of %R&R if the capability of the point measurements is calculated individually [58]. HDM systems are also typically prone to having measurement outliers, which might skew the results for some of the measurement points. Due to the high dimensionality of the measurement data, it is highly likely that false alarms will occur as individual points might fail the MSA. The method has severe shortcomings and is not recommended for use for HDM systems.

*PCA MSA.* The primary advantage of using a PCA approach is that it decomposes the measurement data into orthogonal components, thus eliminating data autocorrelation and resulting in more accurate %R&R estimations. By reducing the dimensionality of the data while capturing most of the variation between the measurements this method decreases the number of calculations required as compared to pointwise calculations. In addition, the results are condensed into a single %R&R figure, which can be easily compared to industry standard thresholds. However, the primary disadvantage is that PC scores are unitless and have no relationship to the initial measurements. Therefore, capability indices such as the P/T ratio cannot be calculated as the product tolerance is meaningless when compared to the standard deviation based on the PC's. Another disadvantage is that

using PCA as a reduction method does not provide information about the spatial distribution of the %R&R, such that defective areas cannot be located.

*Cluster MSA.* The cluster method is a compromise between the pointwise and the PCA methods for data reduction, as the data is reduced significantly while preserving the data units of measurement. One of the main advantages of this method is that it provides a visual, spatial map denoting the areas of the part where the gauge is not performing well. For example, it is not uncommon that laser based systems will have more variability towards the edges of the field of view. This method highlights the spatial pattern of the %R&R such that the problematic areas can be uncovered. Detecting the field of view areas which have high %R&R allows operators to potentially diagnose the gage problem and aid in gage calibration. One disadvantage of this method is that the selection of the number of spatial clusters may be subjective. In addition, the choice to use one clustering scheme over another might result in different spatial clusters and alter the results of the MSA.

### **3.4. Chapter Summary**

This chapter proposes an MSA framework for planar and volumetric HDM systems, and compares the framework with other existing MSA methods. The developed framework first registers and regularizes the measurement data using an engineering-driven approach to establish a common basis for comparison. Then, the data is reduced through spatial clustering, and the MSA study performed on the individual clusters. Case studies were conducted which demonstrated the advantages of the proposed framework over methods utilized by practitioners. Compared with previous approaches, the improvements of the proposed framework are:

- *Engineering-driven MSA for HDM systems:* An improved surface model which considers spatial and cross-correlations with process variables is proposed. The surface estimation method improves the accuracy and precision of the interpolated measurements, particularly in areas where there are a low number of observed measurement points.
- *Comparison on the effect of data reduction methods on MSA for HDM systems:* A comparative study between using several data reduction methods was done. It was found that using the spatial clustering and PCA data reduction methods effectively capture and summarize the global and local surface variations of the HDM gage.
- *Zone by Zone MSA:* The proposed spatial clustering based MSA method is able to locate the areas within the field of view where the gage is not capable. This enables the diagnosis of gage problem areas and aids with gage calibration.



## CHAPTER 4

### SURFACE VARIATION MONITORING USING HDM

Statistical process control for manufacturing processes is vital for process variation reduction and product quality improvement. In high precision manufacturing processes, it is often necessary to control the part surface variation within micron levels; thus, high definition metrology (HDM) systems which can measure parts densely across the surface may be employed to measure parts for the purposes of process control.

As explored in Chapter 1, HDM measurements can provide rich information at different feature scales, but the high density of data presents significant challenges in utilizing them for quality control. HDM data may have redundancy and cause unnecessary computational load for certain diagnostic purposes. HDM data may also be cost prohibitive and time consuming to measure. Most importantly, data show strong correlation patterns. In Figure 4.1, the top surface on the part was divided into 36 regions, and the relationships between the average height of each region plotted using scatter diagrams. Regions that are close to each other (such as  $R_1$  and  $R_2$ ) show a linear relationship between the average heights, while regions that are further apart (such as  $R_1$  and  $R_{33}$ ) do not exhibit such linear relationship.

In this chapter, new methods for HDM based monitoring are proposed to address the identified challenges. In section 4.1, a sequential monitoring method is developed for monitoring full-resolution HDM data. When HDM data is limited, a method is proposed in section 4.2 for monitoring of multi-resolution data based on a data fusion model presented in Chapter 2. The chapter is concluded in section 4.3.

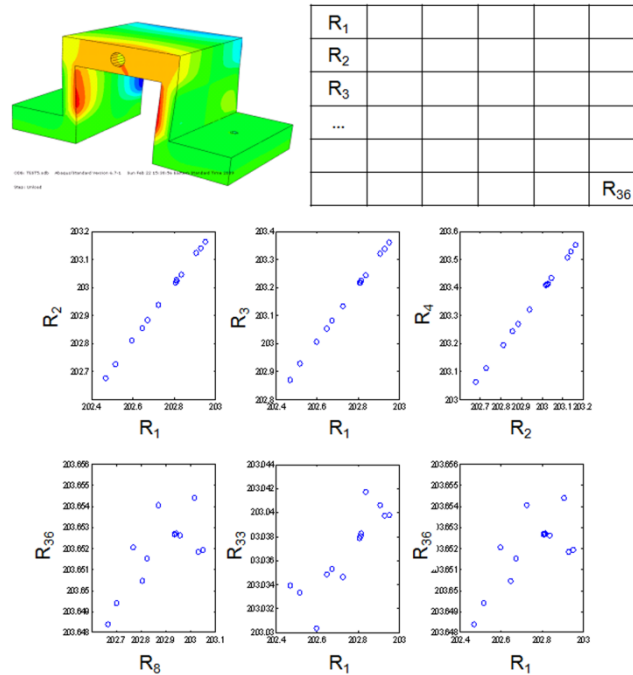


**Figure 4.1 Scatter Plot of Spatial Data between Regions**

#### **4.1. Sequential Monitoring of HDM Data**

A method is proposed to sequentially monitor process variation at both global and local scales using full resolution HDM data. The iterative approach is shown in Figure 4.2. At both scales, the process is first monitored by using a PCA-filtered principal curve regression method in conjunction with multivariate control charts. The idea is to reduce the data dimension through PCA and to parameterize the principal curve fitted through a non-parametric method, thereby constructing a model-based test statistic for process

monitoring. If an out of control condition is detected, localized monitoring is performed, in which the part surface is divided into a number of regions, and each region is monitored independently using EWMA charts. This aids in localizing the surface region where the defect is occurring, which supports diagnosis of variation sources.

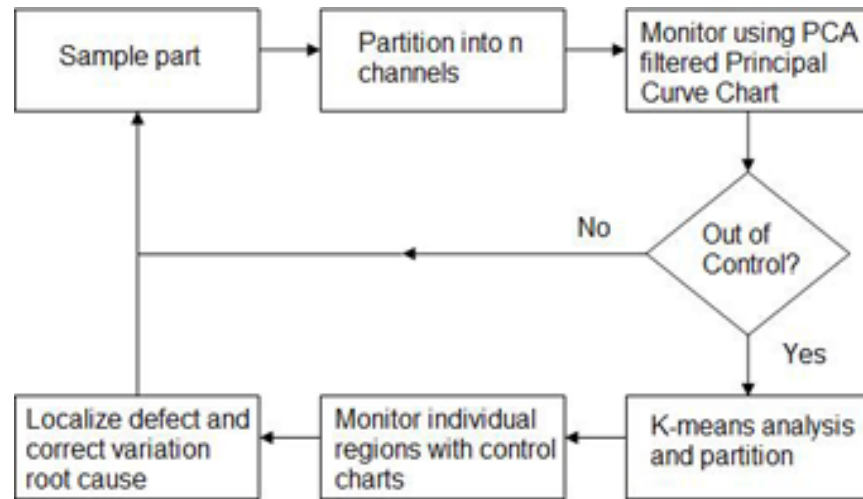


**Figure 4.2 Proposed HDM data monitoring Framework**

#### ***4.1.1. Preprocessing of HDM Data***

The HDM data should be preprocessed for efficient statistical analysis. Two preprocessing steps are required: data decomposition and data reduction through partitioning.

##### ***HDM data decomposition***

One challenge with monitoring schemes for HDM data is that the large scale variation may mask the variation change at a smaller scale. Potential sources of variation responsible for shape deformations are cutting forces, fixture errors and tool path deviation, while the sources for responsible for small scale feature variation may be

tooling related. Thus, it becomes difficult to differentiate between the variation patterns in both scales and conduct root cause diagnosis.

It is necessary to separate the large scale variation from the small scale variation (refer to Figure 4.3). The trend surface that characterizes surface shape can be obtained by interpolating the point cloud data into a grid using a large smoothing parameter. The surface that contains small scale features can be obtained by subtracting the trend surface from the original surface. Such decomposition allows the monitoring of process stability at two different levels. The first is concerned with the stability of the shape and overall spatial variability of the data over time. The second is the monitoring of smaller scale features.

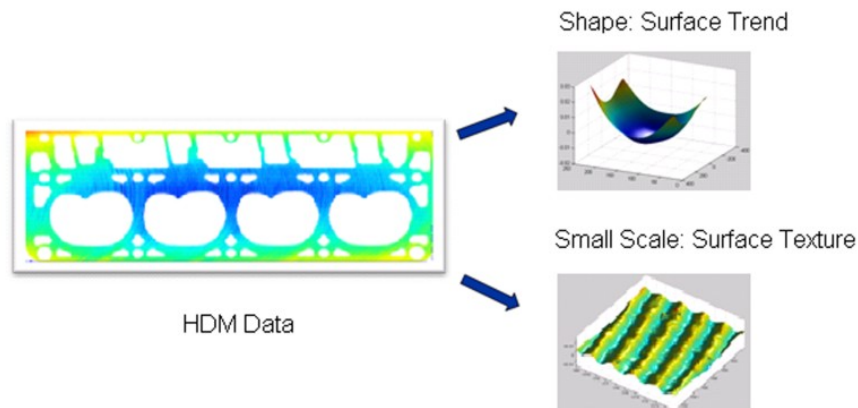


**Figure 4.3 Decomposition of HDM Data**

### ***HDM Surface Partition***

The metrology using laser holographic interferometry produces scattered data for  $x$ ,  $y$ , and  $z$  coordinates on a machined flat surface. For variation control purposes, the primary concern is to analyze  $z$  values (response) that are spatially distributed along the  $x$  and  $y$  directions. Since the points in the vicinity of each other usually show strong linear

correlation, they can be grouped into one region  $\mathbf{R}_i$ . A finer partition  $\{\mathbf{R}_i\}_{i=1}^n$  resulting in more regions, will better delineate the surface topography. The averaged height values  $\bar{z}$  in each region partitioned on the surface can be used as the response and a group of  $\{\bar{z}_{ij}\}_{i=1}^n, j=1,2,\dots,m$ , give the HDM data representation over  $n$  regions on each of a total of  $m$  part surfaces. The reasons for surface partitioning are: (1) to reduce the data redundancy and dimensionality by grouping the data points with similar responses; and (2) to produce a response in each region that follows a normal distribution (by the central limit theorem in applied statistics) to facilitate statistical monitoring.

Surface partitioning may be difficult for a non-rectangular surface or a surface with more complex spatial patterns (e.g., holes and grooves etc., such as the part surface in Figure 4.3) on it. The regions may not be of equal size because of the existence of empty zones. As a result, the average value  $\bar{z}$  in distinct regions may follow different normal distributions and make statistical monitoring of overall features infeasible. One way to deal with this problem is to project the scattered HDM data onto rectangular grids through interpolation and extrapolation methods, as discussed in section 3.1.1.2.

#### ***4.1.2. Large Scale Monitoring using Parameterized Principal Curve***

##### ***4.1.2.1. Principal curve modeling***

The principal curve modeling method is a generalization of PCA that captures the nonlinear variation pattern among spatial data. It is defined as a smooth and self consistent (not self-intersecting) curve  $\mathbf{f}(t)$  passing through the middle of a  $p$ -dimensional data cloud. Figure 4.4 shows an example of two-dimensional data ( $R_1$  vs.  $R_{36}$ ) and their principal curve fitted by projecting the data points onto it in an “orthogonal sense” [20].

For a collection of  $p$ -dimensional data from  $m$  parts  $\mathbf{z}_j=[z_1 \ z_2 \dots \ z_p]^T$ ,  $j=1,2,\dots,m$ , assume that  $\boldsymbol{\mu}$  and  $\boldsymbol{\Sigma}$  are the mean vector and covariance matrix, respectively. Also denote  $\lambda_i$  as the eigenvalues and  $\mathbf{e}_i$  their corresponding eigenvectors. The Hastie-Stuetzle algorithm for data projection searches for an estimate  $\hat{\mathbf{f}}(\cdot)$  that minimizes  $\sum_j \|\mathbf{z}_j - \hat{\mathbf{f}}\|^2$ .

The procedure can be stated as follows:

- Set initial values for projection as  $\mathbf{f}_0(t) = \boldsymbol{\mu} + t\mathbf{e}_1$ , which represents principal direction of the distribution of  $\mathbf{z}$  and set  $h=0$ .
- For each point  $\mathbf{p}$  on the projected curve, calculate the average of values in the neighborhood  $N(\mathbf{p})$  of  $\mathbf{p}$ , i.e.,  $1/n \sum_{i \in N(\mathbf{p})} z_i$ ; let  $h=h+1$ .
- Construct a new curve  $\mathbf{f}_h(t)$  using  $\mathbf{p}$ ' and replace  $\mathbf{f}_{h-1}(t)$ ;

Continue the iteration until estimation error  $\sum_j \|\mathbf{z}_j - \mathbf{f}_h\|^2$  does not change. For high-dimensional data, it is difficult to visualize the principal curve as shown in Figure 4.4. Instead, we can inspect the projection of the principal curve at each region with respect to  $t$ . Figure 4.5 shows an example of a principal curve projected onto 2 regions. It can be seen that the principal curve increases with  $t$  in region 33 while region 36 shows an increasing trend along with oscillatory patterns. This indicates that region 33 (on the edge of the part) and region 36 (on the corner) were bent upward over the 15 parts.

However, visual inspection of a principal curve from multiple regions is not an objective method to evaluate the process behavior. A quantitative method is required to monitor the nonlinear variation patterns.

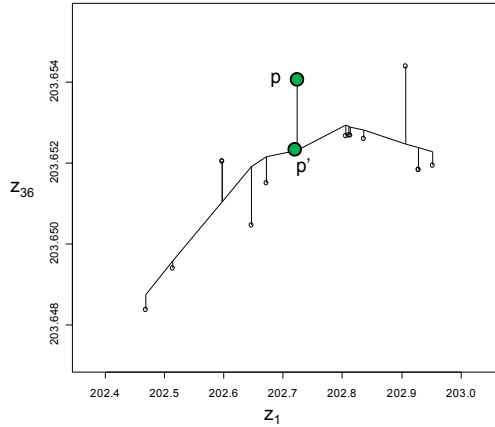


**Figure 4.4 An Example of a Principal /Curve for 2-D case**

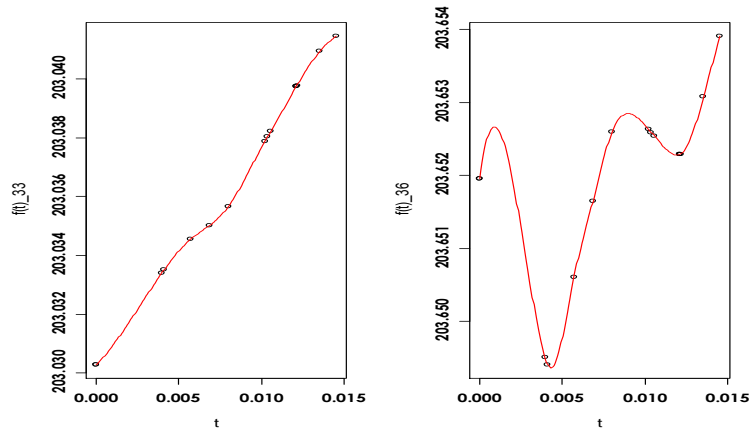


**Figure 4.5 Principal Curve projection at Regions 33 & 36**

For statistical monitoring purposes, it is necessary to know the underlying distribution of the metric of interest. Although a principal curve can efficiently capture the variation in multi-dimensional data, the distribution of a certain point  $\mathbf{p}'$  on the curve is not known. One can observe from Figure 4.4 that the value of  $\mathbf{p}'$  shows a positive correlation with the original data that are close to  $\mathbf{p}'$ . Motivated by this phenomenon, it is reasonable to parameterize the principal curve by building a regression model linking the original data to their projection  $\mathbf{p}'$  on the curve [85]. If the model accurately predicts the principal curve, the prediction error will follow a normal distribution.

Therefore, a parameterized principal curve model can be proposed as follows:

$$y_a = \beta_{0,a} + \sum_i \beta_{i,a} z_i + \sum_{i,j} \beta_{ij,a} z_i z_j + \dots + \varepsilon_a, \quad a = 1, 2, \dots, p \quad (4-1)$$

where  $y_k$  is the  $k$ th projected point on the principal curve,  $z_i$  is the averaged  $z$ -values in the  $i$ th region, and  $\varepsilon_k$  is the noise. When the data are filtered with PCA,  $z_i$  will be replaced by its score vector  $\mathbf{w}_j$  in the space spanned by  $\{\mathbf{e}_1, \mathbf{e}_2, \dots, \mathbf{e}_k\}$ , i.e.,

$$y_a = \beta_{0,a} + \sum_i \beta_{i,a} w_i + \sum_{i,j} \beta_{ij,a} w_i w_j + \dots + \varepsilon_a, \quad a = 1, 2, \dots, k \quad (4-2)$$

Stacking up Eq. (5.2) over all the principal components, one can write

$$\mathbf{Y}_{n \times k} = [\mathbf{I}_{n \times 1} \quad \mathbf{W}_{n \times l}] \mathbf{B}_{(l+1) \times k} + \mathbf{E}_{n \times k}, \quad (4-3)$$

where  $\mathbf{Y}_c = [y_{c1} \ y_{c2} \ \dots \ y_{ck}]$ ,  $\mathbf{W}_c = [w_{c1} \ w_{c2} \ \dots \ w_{ck} \ w_{c1} w_{c2} \ \dots]$ , each column in  $\mathbf{B}$  consists of  $[\beta_{0,a} \ \beta_{i,a} \ \beta_{ij,a} \ \dots]^T$ ,  $i=1, 2, \dots, n$ ,  $\mathbf{I}$  is an all-one vector, and  $[\varepsilon_1 \ \varepsilon_2 \ \dots \ \varepsilon_k]^T \sim N(\mathbf{0}, \boldsymbol{\Sigma}_{k \times k})$ . The subscripts indicate the matrix sizes. The covariance matrix  $\hat{\boldsymbol{\Sigma}}$  will be estimated by a generalized least square estimation procedure by minimizing  $(\mathbf{Y} - [\mathbf{I} \ \mathbf{W}]\mathbf{B})^T \boldsymbol{\Sigma}^{-1} (\mathbf{Y} - [\mathbf{I} \ \mathbf{W}]\mathbf{B})$ . The coefficient matrix  $\hat{\mathbf{B}}$  can be found by  $\hat{\mathbf{B}} = ([\mathbf{I} \ \mathbf{W}]^T \hat{\boldsymbol{\Sigma}} [\mathbf{I} \ \mathbf{W}])^{-1} [\mathbf{I} \ \mathbf{W}]^T \hat{\boldsymbol{\Sigma}} \mathbf{Y}$ . The terms in  $\mathbf{Z}$  can be chosen according a model selection procedure, e.g., forward selection.

The overall feature monitoring is briefly summarized as follows:

- Step 0.* Data preprocessing. Project HDM onto rectangular grids and partition the surface into regions as shown in Section 2.1. A finer partition is preferred for monitoring spatial variation pattern;
- Step 1.* Initialization. Let  $h=0$ . Assume a simple model for each row in  $\mathbf{W}$ , denoted as  $\mathbf{w}^{(0)} = [w_1 \ w_2 \ \dots \ w_k]$ . The total number of terms except intercept is  $q_0 = k$ . Then estimate  $\hat{\boldsymbol{\beta}}^{(0)}$ ,  $\boldsymbol{\varepsilon}^{(0)} = \mathbf{y} - [\mathbf{1} \ \mathbf{w}^{(0)}] \boldsymbol{\beta}^{(0)}$ , and residual sum of squares  $RSS^{(0)} = \sum_{c=1}^n [\varepsilon_c^{(0)}]^2$ ;



*Step 2.* Model expansion. Add more terms to  $\mathbf{w}^{(h)}$  (e.g., interaction terms  $w_i w_j$  or quadratic terms  $w_i^2$ ) and let  $h=h+1$ . In total,  $\mathbf{w}^{(h)}$  contains  $q_j$  parameters.

Estimate  $\hat{\boldsymbol{\beta}}^{(h)}$ ,  $\boldsymbol{\varepsilon}^{(h)}=\mathbf{y}-[\mathbf{1} \ \mathbf{w}^{(h)}]\boldsymbol{\beta}^{(h)}$ , and residual sum of squares  $RSS^{(h)}=\sum_{c=1}^n [\varepsilon_c^{(h)}]^2$ ;

*Step 3.* Model comparison. Calculate an  $F$  test statistic

$$F = \frac{[RSS^{(j)} - RSS^{(j-1)}]/(q_j - q_{j-1})}{RSS^{(j-1)}/(n - q_j - 1)}. \quad (4-4)$$

If  $F > F_{q_j - q_{j-1}, n - q_j - 1}(\alpha)$ , which is the  $100(1-\alpha)\%$  percentile of an  $F$  distribution with degrees of freedom  $q_j - q_{j-1}$  and  $n - q_j - 1$ , continue the model expansion in Step 2.

Otherwise, the model expansion in Step 2 cannot significantly improve the model accuracy and the smaller model will be chosen as the final model.

By multivariate statistics, the prediction error  $\boldsymbol{\varepsilon}$  is distributed as  $N(\mathbf{0}, (1 + [\mathbf{1} \ \mathbf{w}_i^*]\{[\mathbf{1} \ \mathbf{W}_0]^T[\mathbf{1} \ \mathbf{W}_0]\}^{-1} \begin{pmatrix} 1 \\ \mathbf{w}_i^{*T} \end{pmatrix})\boldsymbol{\Sigma})$ , where  $\mathbf{w}_i^*$  represents the new measurements projected onto the same subspace  $\text{span}\{\mathbf{e}_1 \ \mathbf{e}_2, \dots, \ \mathbf{e}_k\}$ . Therefore, one can establish a control chart for monitoring  $\hat{\boldsymbol{\varepsilon}}$  using  $100(1-\alpha)\%$  prediction ellipsoid:

$$\begin{aligned} & \{\mathbf{y}_i - [\mathbf{1} \ \mathbf{w}_i^*]\hat{\boldsymbol{\beta}}_k\}^T \left(\frac{n}{n-l}\hat{\boldsymbol{\Sigma}}\right)^{-1} \{\mathbf{y}_i - [\mathbf{1} \ \mathbf{w}_i^*]\hat{\boldsymbol{\beta}}_k\} \leq \\ & (1 + [\mathbf{1} \ \mathbf{w}_i^*]\{[\mathbf{1} \ \mathbf{W}_0]^T[\mathbf{1} \ \mathbf{W}_0]\}^{-1} \begin{pmatrix} 1 \\ \mathbf{w}_i^{*T} \end{pmatrix}) \left[\frac{p(n-l-1)}{n-l-p}\right] F_{p, n-l-p}(\alpha), \end{aligned} \quad (4-5)$$

where  $\mathbf{W}_0$  represents the measurements under the baseline conditions.

It has been found that HS algorithm [21] for fitting a principal curve could be sensitive to those points that are far from the data cloud (outliers), especially for high-dimensional data. False alarms will increase as the data dimension increases. Therefore, PCA based data reduction is a very necessary step to reduce the false alarm rate.

If the HDM data do not show a strong nonlinear pattern, principal components can be directly monitored by  $T^2$  Hotelling chart. The  $T^2$  test statistics for the  $i$ th sample can be estimated by

$$T_j^2 = \sum_{a=1}^k \frac{w_{a,j}^2}{\lambda_{a,j}}, \quad w_{a,j} = \mathbf{e}_a^T (\mathbf{z}_j - \bar{\mathbf{z}}), \quad (4-6)$$

where  $\lambda_a$  and  $\mathbf{e}_a$ ,  $a=1,2,\dots,k$ , and  $\bar{\mathbf{z}}$  are defined in the same way as above, where the Phase I control limit is

$$UCL = \frac{(m-1)^2}{m} B_{1-\alpha, k/2, (m-k-1)/2}, \quad (4-7)$$

and the Phase II control limit is

$$UCL = \frac{k(m+1)(m-1)}{m^2 - mp} F_{1-\alpha, k, m-k}, \quad (4-8)$$

where  $m$  is the number of observations for each region and  $\alpha=0.10$ .

#### ***4.1.2.2. Global Monitoring Case Study using PCA filtered Parameterized Principal Curve***

The proposed global monitoring method was applied to a set of simulated HDM data obtained via FEM prediction. These simulated parts are similar to the data obtained from the laser holographic interferometry system. To create the HDM data, a fine mesh was used to generate 52,300 elements in total. This simulation ignored the smaller scale features (e.g., tool marks) caused by machine tools.

Figure 4.6 shows the simulated aluminum alloy part with the top surface being milled followed by a drilling process on its side surface. The part was clamped on a fixture plate and located by a round pin on the left and a diamond pin on the right. The material

properties are given in Table 4.1. The fixture on the left side was assumed to vary along the vertical directions following  $N(0, 0.2^2 \text{ mm}^2)$ . The data can be used to monitor the stability of the process and analyze the impact of the drilling and clamping on the quality of the top surface.

The data on each surface were first projected onto rectangular grids and partitioned into numerous regions. Since no small scale features were available, a partition with  $6 \times 6$  regions was adequate to capture the spatial pattern in this case. The bottom panel of Figure 4.1 shows scatter plots of paired average height data from different regions, where both linear (upper panels) and nonlinear patterns (lower panels) can be identified.

**Table 4.1 Material Properties for FEM Simulation**

Material	AA2024	Poisson's ratio	0.33
Young's Modulus	70 Gpa	Ultimate stress	469 Mpa
Yield stress	324 Mpa	Elongation	20%

For monitoring purposes, nine of the samples were used to establish a baseline condition, while six parts were used as testing data. Two additional parts were simulated to have larger variation ( $\pm 0.2 \text{ mm}$ ) and mean-shifts ( $+0.2 \text{ mm}$ ) in regions  $\mathbf{R}_1 \sim \mathbf{R}_3$ . These were used as samples 7 and 8 in the testing data set, and served as nonconforming parts under a faulty process condition.

As shown in [20], if the distribution of multi-dimensional data can be approximated as piecewise linear, PCA can be used as a pre-processing step to reduce the data dimension without losing the variation information. Piecewise nonlinearity is not

uncommon in many manufacturing applications. In this case, the principal curve can be approximated by a set of hyper straight lines connected to each other. Assume there are  $k$  ( $\leq p$ ) dominant eigenvalues. Denote  $\mathbf{P}$  as the transformation matrix consisting of the first  $k$  eigenvectors  $\{\mathbf{e}_a\}_{a=1}^k$  of covariance matrix  $\Sigma$ . Thus, the PCA score vectors can be estimated by  $\mathbf{w}_j = \mathbf{P}^T [\mathbf{z}_j - \bar{\mathbf{z}}]$ , where  $\mathbf{w}_j = [w_{1j} \ w_{2j}, \dots, \ w_{kj}]^T$  is a  $k \times 1$  vector and  $\bar{\mathbf{z}}$  is the average vector of  $m$  parts.

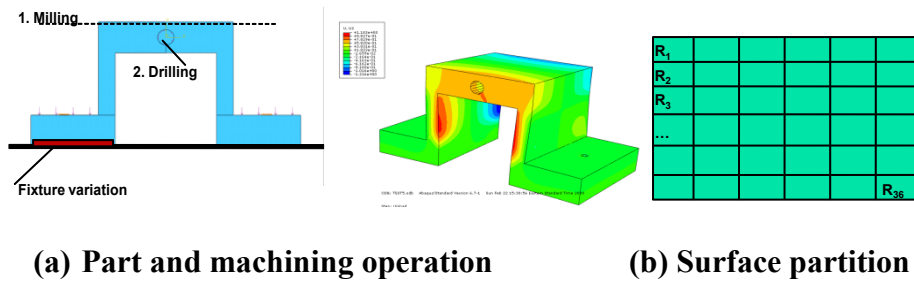


**Figure 4.6 Part and Machining Operation for Case Study**

Figure 4.7 shows the first four eigenvalues of the covariance matrix for the data from 36 partitioned regions. It can be seen that the first four principal components explain more than 90% of the total variation among the 36 regions. Thus, only the first four principal components need to be monitored and the data dimension is significantly reduced.

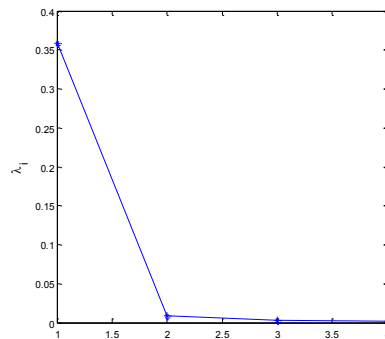


**Figure 4.7 Scree Plot based on PCA**

Applying Equations 4-1 ~ 4-4 to the PCA filtered data in the case study, it was found that a linear model is adequate ( $j=1$ ) to predict the variation of the principal curve. Table 2 lists the intercepts and the coefficients in front of 4 principal components. The coefficients for the insignificant variables are not shown. Figure 4.8 displays a multivariate control chart for the case study data based on Equation 4-5, where the nonconforming samples 7 and 8 have been successfully detected to be out-of-control.

**Table 4.2 Model Coefficients for the first 4 Principal Components**

	$Y_1$	$Y_2$	$Y_3$	$Y_4$
<b>Intercept</b>	--	--	--	--
<b><math>w_1</math></b>	1.00	--	--	--
<b><math>w_2</math></b>	--	$3.30 \times 10^{-1}$	$-1.5 \times 10^{-1}$	$3.50 \times 10^{-2}$
<b><math>w_3</math></b>	$-1.58 \times 10^{-3}$	$-2.22 \times 10^{-1}$	$1.44 \times 10^{-1}$	$5.94 \times 10^{-2}$
<b><math>w_4</math></b>	$1.20 \times 10^{-3}$	$6.48 \times 10^{-2}$	$7.55 \times 10^{-2}$	$5.62 \times 10^{-1}$

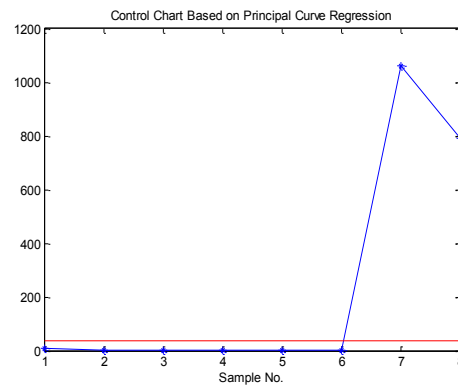


**Figure 4.8 Multivariate Control Chart based on the Parameterized Principal Curve Model**

Figure 4.9 shows the direct monitoring of principal components using  $T^2$  control chart ( $k=4$ ) for 36 regions. The left panel is the Phase I control chart and the right one gives the

Phase II control monitoring 8 samples. Samples 7 and 8 are also detected to be out-of-control.

It can be observed that Figure 4.8 and Figure 4.9 (Phase II) exhibit a similar pattern, which implies that the linear variation patterns in the data from 36 regions are more significant compared with nonlinear patterns. This phenomenon is quite common in multiple simulations of bending variation caused by clamping and drilling.

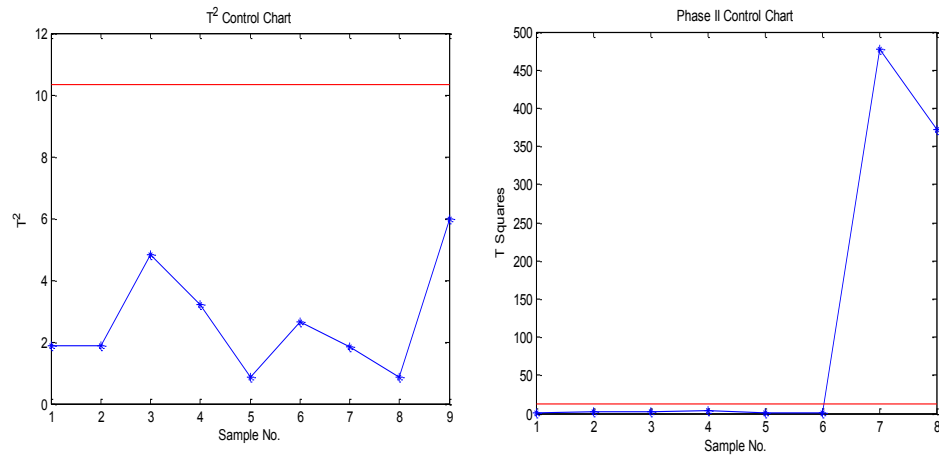


**Figure 4.9  $T^2$  control Chart for Monitoring Principal Components**

### ***4.1.3. Localized Monitoring using Spatial Clustering***

The global monitoring using the parameterized principal curve method is unable to pinpoint the surface region where the defect occurs; hence, the purpose of localized monitoring is to identify the out-of-control surface region in order to provide insight to the root cause of the variation. Localized monitoring methodology first partitions the part into  $k$  regions, and focuses on monitoring part-to-part variation in each of the individual regions by using conventional control charts.

#### 4.1.3.1. Spatial clustering analysis

The selection of regions for localized monitoring requires careful consideration. A very fine partition can generate regions highly correlated to each other, thus leading to a large number of redundant regions for inspection and computational inefficiency. Conversely, a small number of regions might not accurately represent part surface differences or spatial characteristics.

This section presents a partitioning method using spatial clustering analysis to obtain an estimate of the number of regions required to capture the spatial variation pattern of the part. There are a number of statistical clustering methods. The K means algorithm [78, 86] is a clustering analysis technique which partitions  $n$  observations into  $k$  clusters that minimize each cluster's within sum of squares (WSS), such that the objective function is

$$\arg \min_s \sum_{i=1}^k \sum_{z_j \in S_i} (z_j - \mu_i)^2, \quad (4-9)$$

where  $z_j$  is the mean surface height for the  $j^{\text{th}}$  region,  $k$  is the number of desired clusters,  $S_j$  are the sets formed by partitioning into  $k$  groups such that  $S_j = (S_1, \dots, S_k)$ , and  $\mu_i$  is the centroid of each set.

The selection of the partition number (clusters)  $k$  is important as the number of groups should be adequate to capture spatial variability. The most popular methods for the selection of  $k$  are the Calinski criterion, the SSI criterion and the elbow test based on a scree plot. The method utilized in this research is the elbow test, as the other criterions did not converge upon repeated iterations. To select the variable  $k$ , a plot of the WSS

versus the number of groups is created. The best value of  $k$  is deemed to be the one where the WSS has decreased significantly (i.e. there is a ‘bend’ in the plot).

The procedure to find the  $k$  clusters for the regions is below.

*Step 0.* Select the number of  $k$  clusters to classify observations into, using any selection criteria method (e.g. elbow method, Calinski, or SSI).

*Step 1.* Select initial values for centroids,  $\{c_i\}^k$ .

*Step 2.* Generate  $k$  clusters such that each observation is grouped with the nearest  $c_i$ .

*Step 3.* Find the centroids for each new cluster. These centroids of become the new cluster generator  $\{c_i\}^k$ .

*Step 4.* Iterate steps 1 through 3 until the results converge and cluster assignments are unchanged.

#### ***4.1.3.2. Monitoring Procedure***

By first partitioning the part into an arbitrary, but sufficiently large  $n$  regions, the K means algorithm can be utilized to group the regions that have similar means into  $k$  clusters, where  $k < n$ . Based on the spatial configuration, these  $k$  clusters can be further subdivided into  $p$  subclusters, where each subcluster consists of regions that are spatially adjacent to each other. These subclusters can then be monitored individually. This will reduce the computational load of monitoring  $n$  regions, but at the same time ensure that the spatial complexity of the part is captured.

The proposed localized monitoring procedures are stated below.



- Step 0.* Project the data onto rectangular grids as outlined in Section 2.1.
- Step 1.* Calculate the average part for the last  $m$  parts if the out-of-control has been detected by the overall monitoring (at least  $m = 10$  recommended)
- Step 2.* Tessellate the average part surface into  $n$  rectangular regions, where  $n$  is selected by the operator depending on part complexity (at least  $n = 25$  recommended).
- Step 3.* Find the clustering of the observations into  $k$  clusters by using K means algorithm.
- Step 4.* Create  $p$  final clusters based on the spatial arrangement of the  $k$  clusters ( $p \geq k$ ). If a cluster consists of regions that are not adjacent to each other, divide each cluster into as many subclusters as necessary so that each new subcluster consists only of contiguous regions.
- Step 5.* Calculate the average for each region,  $\bar{z}_i$  for all  $i = \{1, \dots, p\}$ .
- Step 6.* Monitor each  $z_i$ , using individual EWMA charts. If an out-of-control condition exists in region  $i$ , find the source of variation and probable cause.

#### **4.1.4. Small Scale Monitoring using Variograms**

The iterative procedure as described in Figure 4.2 can also be applied to monitoring the part small scale features (such as surface waviness). Using conventional SPC techniques for the localized monitoring to isolate the defective region for small scale features provides some information for root cause diagnosis, but is limited in calculating the scope and exact location of the process change. This section proposes a new

methodology for the localized monitoring of small scale features. The methodology uses spatial statistics to provide further insight to diagnose variation sources.

One common measure of spatial variability is the variogram, which quantifies the spatial dissimilarity of a surface as a function of the lag between surface points [87-89]. This chapter proposes the use of variogram functions to characterize the part surface topography, and to use these variogram profiles to monitor the spatial variability of the small scale features.

The variogram is defined as

$$2\gamma(\mathbf{h}) = \text{Var}[z(\mathbf{u}) - z(\mathbf{u} + \mathbf{h})] = \text{E}\{[z(\mathbf{u}) - z(\mathbf{u}+\mathbf{h})]^2\}, \quad (4-10)$$

where  $z$  is a stationary random function with mean  $m$  and variance  $\sigma^2$  for all locations  $\mathbf{u}$  in the study area. The variogram is therefore the square of the expected difference between two data values which are separated by a distance vector  $\mathbf{h}$ . It is also common to use the quantity  $\gamma(\mathbf{h})$ , referred to as a semi-variogram for interpretation and analysis.

Figure 4.10 shows a theoretical semi-variogram.

Applied to HDM data, the variogram can be thought of as the spatial dissimilarity of the surface height as a function of radial distance. The variogram thereby is a non-linear function that characterizes the surface texture waveform in two dimensions. Using a two dimensional variogram captures more information than using a single trace of the part surface height, therefore by using the variogram profiles to monitor part to part variation, out of control conditions can be detected in both the x and y directions. In addition, variograms can provide better insight to root cause variation identification, as

abnormalities in the variogram pattern can be used to determine the location of the disturbance.

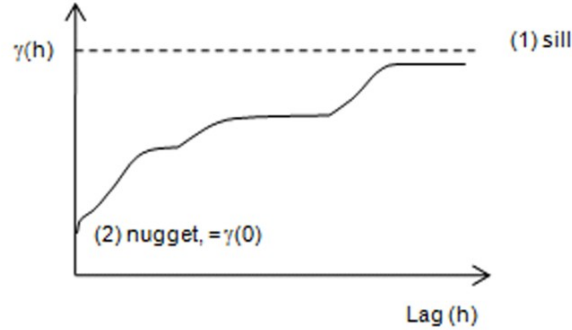


**Figure 4.10 Theoretical Variogram**

Due to the surface complexity of the case study data, the approach used was to isolate critical patches, or regions and monitor them independently. The procedure for small scale monitoring based on the variogram is as follows:

*Step 0.* Extract surface information at  $r$  different regions of interest for  $n$  normal production parts.

*Step 1.* Calculate  $g_{ij}(\mathbf{h})$ , where  $i = 1 \dots n$ , and  $j = 1 \dots r$ .

*Step 2.* Calculate Phase I control limit for each region  $r$ , where

$$UCL_r(\mathbf{h}) = \frac{1}{n} \sum_{i=1}^n \gamma_i(\mathbf{h}) + \frac{3}{n} \sum_{i=1}^n (\gamma_i(\mathbf{h}) - \overline{\gamma(\mathbf{h})})^2, \text{ and } LCL_r(\mathbf{h}) = 0.$$

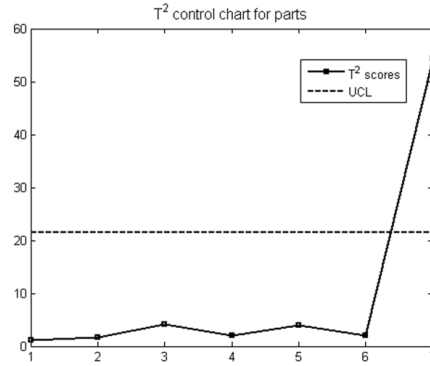
*Step 3.* Monitor each  $g_{ir}(\mathbf{h})$ , using the control limits established in step 2 in  $r$  control charts. If an out-of-control condition exists in region  $r$ , find the source of variation and probable causes.

#### ***4.1.5. Case Study***

The proposed sequential monitoring methodology was applied to an automotive engine head case study. Parts were measured using an HDM measurement system with an x-y resolution of 150  $\mu\text{m}$  and z-height resolution of 1  $\mu\text{m}$ . The parts were mounted by a trained operator onto measurement fixtures and placed beneath the laser system housing for scanning. While it is possible to have an in-line measurement system while using this measurement device, the parts for this study were measured off-line.

##### ***4.1.5.1. PCA Monitoring for Overall Process Diagnosis***

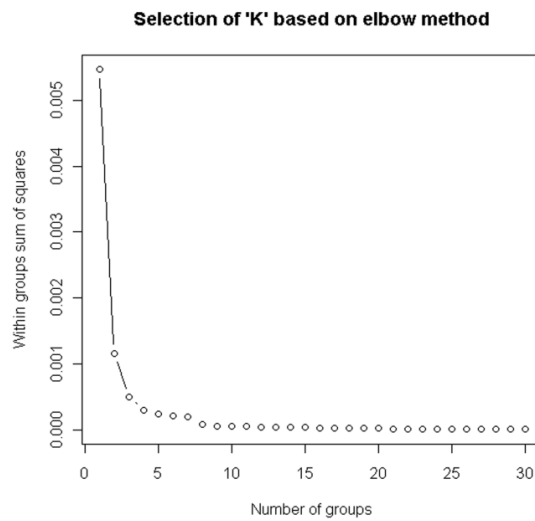
As mentioned in section 4.1.2, in many applications, the spatial variation pattern can be approximated by a linear or piece-wise linear relationship [20]. Thus, this case study only considers the linear correlation pattern and uses PCA to reduce the data dimension. Six normal condition parts were used as training data, and the seventh defective part was used as a test data. It was found that four principal components explained 95% of the variation in the data. These principal components were monitored using a Hotelling  $T^2$  [36] chart for individual sample sizes, which is shown in Figure 4.11. The out of control condition was detected using the PCA multivariate chart, which demonstrates that a linear pattern model is adequate to capture the spatial correlation on machined deck faces of engine heads.



**Figure 4.11 T<sup>2</sup> control chart for Engine Head Principal Components**

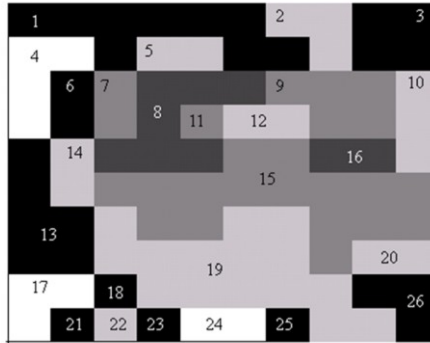
#### ***4.1.5.2. Localized monitoring using Spatial Clustering***

Figure 4.12 shows the scree plot of the WSS versus the number of  $k$  groups for the case study data. Based on the elbow test,  $k = 5$  was selected.



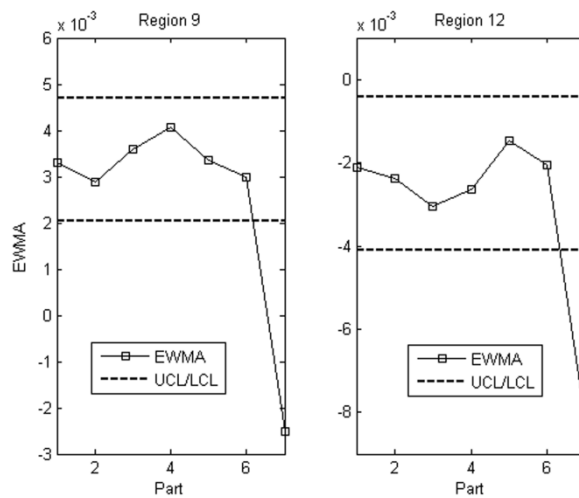
**Figure 4.12 Scree Plot for Selection of  $k$**

Figure 4.13 shows the partition results using the case study samples, with  $n = 100$  and  $k = 5$ . Note that there are now  $p = 26$  regions to be monitored instead of 100. By decreasing the number of regions monitored, the false alarm rate will most likely decrease.



**Figure 4.13 K-means partition for Average Part**

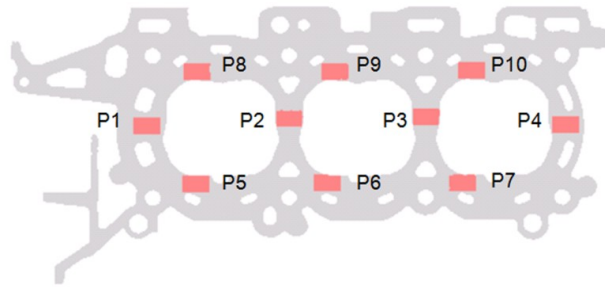
Each of the 26 regions was monitored individually using the first 6 in-control data samples to establish the Phase I control limits. The control charts used were individual EWMA charts with parameters  $\lambda = 0.8$  and 3-sigma limits. The 7 samples were plotted using the Phase I control limits, and the control chart was able to detect the defective part in Regions 9 and 12 as seen in Figure 4.14.



**Figure 4.14 Localized Monitoring using Spatial Clustering**

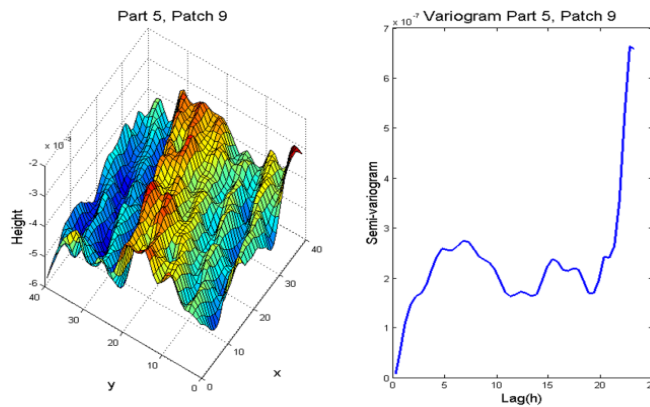
## Localized monitoring using Variograms

Figure 4.15 shows the  $r$  regions of interest that were monitored for the case study data. In this case the regions were chosen due to their critical position in the engine head, and the areas where surface defects are most common. There are 10 regions in total, from  $n = 7$  parts.



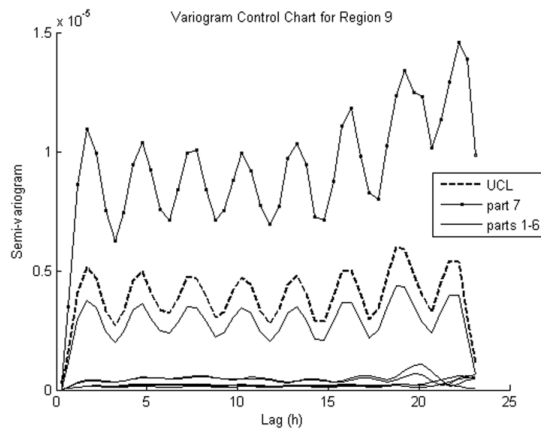
**Figure 4.15 Patch Selection for Case Study Data**

Figure 4.16 shows an example of the surface data from sample 5, Region 9. As it can be seen from the figure, the variogram captures the wave pattern and overall shape of the part. The variogram also indicates that when the distance between points is very large, the dissimilarity increases. Towards the edges of the data set, the part has larger amplitude peaks, which would explain this large jump in the variogram.



**Figure 4.16 Surface and Variogram for Part 5, Patch 9**

Figure 4.17 shows the variograms for each of the parts plus the upper control limit as described in step 2 above. The variogram is able to detect the out of control condition of the defective part (sample 7). Because the magnitude of the sample 7 variogram is higher than the rest, this indicates that the waviness amplitude is higher for sample 7. This higher variogram magnitude possibly indicates a chipped tool, which causes higher vibration thereby affecting the waviness of the surface. The variogram for sample 7 also shows an increasing trend in variation with increased lag which the other parts do not exhibit.



**Figure 4.17 Variogram-based Control Chart**

#### **4.2. Progressive Monitoring of Multi-resolution Data under Bayesian Framework**

This section develops a framework for monitoring the fusion of process data and HDM data based on the surface model proposed in Equations 2-1~2-2. The framework involves two steps as shown in Figure 4.18, including

- A training phase, in which normal production parts are used to establish a baseline correlation model. For each part, the generalized covariance and cross-covariance



models are calculated based on the training data which are collected by employing a HDM system to scan the entire surface; and

- An implementation phase, in which the incoming production parts are monitored and Bayesian inference is used to update the correlation parameters. For monitoring purposes, the measurement should provide information on global trend and fine-scale details of a surface. Therefore, the surface of each part should be measured by a low-resolution metrology system in conjunction with high-resolution measurements that are performed on preselected local regions. The data are used through the established models to estimate a sampling distribution of surface shapes (or equivalently, percentiles at each point). Based on the distribution, a new monitoring algorithm will be developed to establish control limits and identify the locations of out-of-control (OOC) areas. Additional high-resolution measurements on OOC surface areas could be necessary to identify the nature of the defects. Normal parts will be used to update surface model parameters.

The remainder of this section discusses the monitoring algorithm development, which consists of the estimation of the statistical distribution of the surface model to establish control limits, and monitoring procedures.

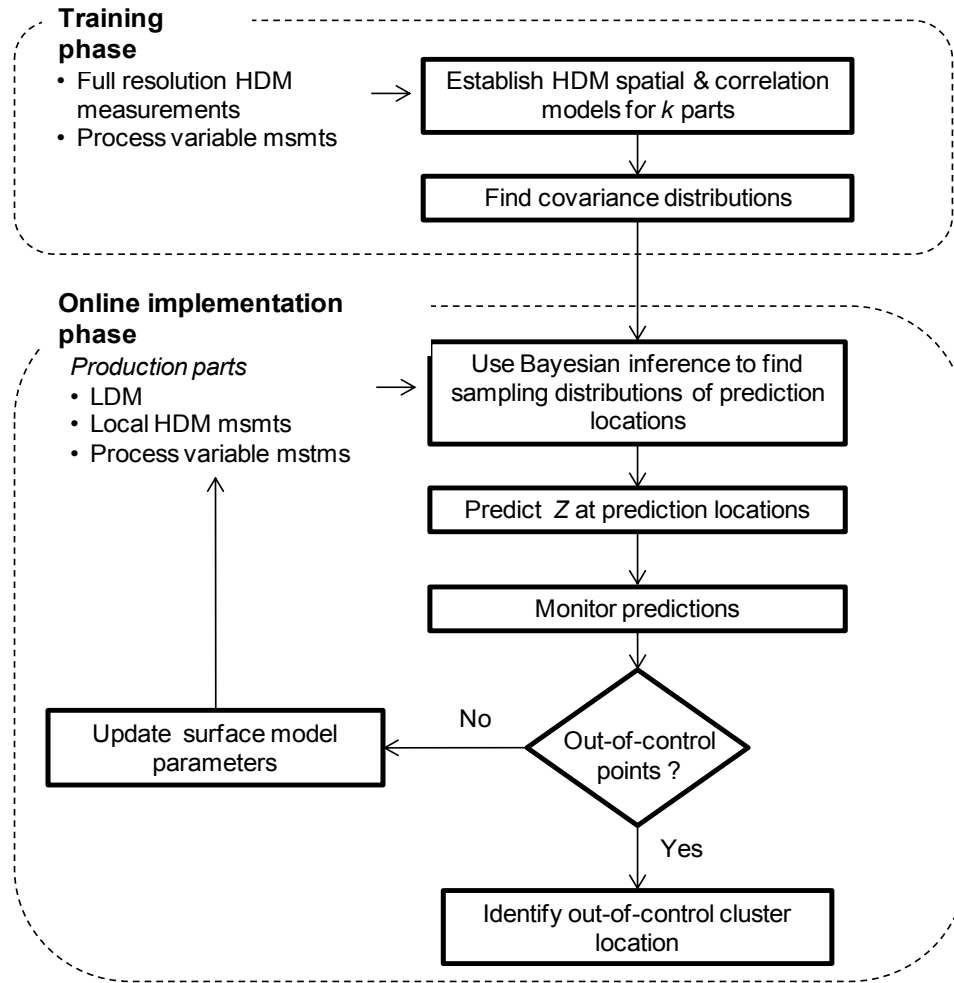


Figure 4.18 Proposed Monitoring Framework

#### 4.2.1. Fusion Model based Inference

To determine the control limits, the distribution of the predicted surface height, ( $Z_1 \dots Z_k$ ) at the  $k$  prediction locations, are needed. Prediction intervals using conventional spatial statistics are based on measuring a single surface, and cannot reflect the part-to-part variation in a manufacturing scenario. As such, the distribution of surface points should be estimated by using the sampling distribution of the prediction obtained from a number of parts. Using the hierarchical spatial model as described in Equations 2-1~2-2 it is assumed that this predictive distribution of surface points are contingent on the

distribution of the parameters  $\boldsymbol{\beta}$ ,  $\boldsymbol{w}$  and  $\tau^2$ . Thus, these models can be solved by using Bayesian inference in three steps [57] The first one estimates the marginal likelihood of the surface distribution as  $\mathbf{Z}(\mathbf{s}) | \boldsymbol{\beta}, \boldsymbol{w}, \tau^2 \sim \prod N(\mathbf{Z}(\mathbf{s}_0) | [1 \ \mathbf{U}^T] \boldsymbol{\beta} + \boldsymbol{w}, \tau^2)$ . The second model estimates the marginal distribution spatial process,  $\boldsymbol{w}$ , which is normal given  $\sigma^2$  and  $\phi$  as  $\boldsymbol{w} | \sigma^2, \phi \sim N(\mathbf{0}, \sigma^2 \mathbf{R}(\phi))$ . Combining the two models, the third model estimates the marginal likelihood for  $Z$  as normal using the parameter prior distributions  $\boldsymbol{\beta}$ ,  $\tau^2$ ,  $\sigma^2$  and  $\phi$  as

$$\mathbf{Z}(\mathbf{s}) | \boldsymbol{\beta}, \tau^2, \sigma^2, \phi \sim N([1 \ \mathbf{U}^T] \boldsymbol{\beta}, \sigma^2 \mathbf{R}(\phi) + \tau^2 \mathbf{I}), \quad (4-11)$$

where  $\mathbf{I}$  is the identity matrix and the  $ij$ th entry of the matrix  $\mathbf{R}$  is  $\sigma^2 \rho(\phi; \|s' - s\|)$ . The first step models the marginal likelihood of  $Z(\mathbf{s})$  as a multivariate normal with a mean influenced by  $\mathbf{U}$  and the residuals,  $\boldsymbol{w}$ . The marginal likelihood of the residuals is assumed to have a normal distribution with a mean of zero and standard deviation dependent on the correlation parameter  $\phi$ . And finally, the marginal likelihood of  $Z$  based on the parameters  $\boldsymbol{\beta}$ ,  $\tau^2$ ,  $\sigma^2$  and  $\phi$  is assumed, where these parameters are assigned a prior distribution based on a sampling of parts. Due to the difficulty in solving these models analytically, a Markov Chain Monte Carlo (MCMC) method is used to estimate the sampling distribution of predicted points, which allows for the calculation of the percentiles needed to establish prediction control limits from a set of in-control training data.

Another inference needed is on estimating and updating correlation model parameters during monitoring. When the HDM measurement on each part is time-consuming, it is not feasible to collect adequate amount of high-dimensional data in order to accurately estimate the model parameters. Additionally, the process baseline could shift (e.g., due to

regular maintenance for tool change) and the resultant data pattern update under the normal condition should be captured by the surface model. Thus, Bayesian inference can be employed to update the spatial and cross correlation parameters progressively once incoming production parts are measured. After establishing the distributions of the parameters  $\boldsymbol{\varphi}=[\boldsymbol{\beta}, \tau^2, \sigma^2, \phi]$  the new posterior distribution,  $f(\boldsymbol{\varphi}|\mathbf{Z}(\mathbf{s}_0), \mathbf{U}(\mathbf{s}_1))$ , can be obtained, i.e.,

$$f(\boldsymbol{\varphi}|\mathbf{Z}(\mathbf{s}_0), \mathbf{U}(\mathbf{s}_1)) \propto f(\boldsymbol{\varphi})f(\mathbf{Z}(\mathbf{s}_0), \mathbf{U}(\mathbf{s}_1)|\boldsymbol{\varphi}) \quad (4-12)$$

where  $f(\boldsymbol{\varphi})$  is the prior distribution of the parameters, and  $f(\mathbf{Z}(\mathbf{s}_0), \mathbf{U}(\mathbf{s}_1)|\boldsymbol{\varphi})$  is the likelihood. The above integral can be approximated by a sampling approach such as Bayesian inference using Gibbs sampling (BUGS). This posterior distribution then becomes the prior distribution for the next incoming part.

#### ***4.2.2. Single Linkage Clustering Monitoring using Surface Fusion Model***

The established surface model considering cross correlations can determine the sampling distribution of predicted surface points  $p(\mathbf{Z}(\mathbf{s})|\mathbf{Z}(\mathbf{s}_0), \mathbf{U}(\mathbf{s}_1))$  as determined by Equation 4-12. The surface manufacturing process can be monitored by comparing each of the predicted surface points to a prediction limit with a desired Type I error. The prediction limits can be established by using the percentiles of the distribution of prediction points determined by Equation 4-12. However, due to the large number of prediction locations, using individual control charts for each point could be sensitive to prediction errors or noise, potentially increasing false alarm rates. To compensate for this increased probability of false alarms, researchers have used correction factors, such as the Bonferroni correction, which distributes the total desired Type I error ( $\alpha$ ) into each of the monitoring charts. The Bonferroni method will yield a very conservative control strategy

in the presence of a large number of points, as the individual chart alpha error will be very small. This method could inflate the control limits, resulting in very few false alarms, but a high misdetection rate of out of control (OOC) areas. Another candidate method for monitoring of HDM data is to use a multivariate control chart (e.g.,  $T^2$  chart). But directly applying such a chart on full resolution part surface data potentially leads to singular covariance matrices for high-density spatial data. In addition, when monitoring surface data, the multivariate charts are able to detect defects, but not locate them. Thus, a strategy is needed to efficiently monitor the surface prediction data with reduced false alarms and locate defective areas.

This section proposes to monitor the predicted surface points that are outside of the normal prediction limit, or the out of limit (OOL) points. Due to the prediction error, it is very likely that a normal part surface will have some predicted points falling outside of the normal prediction limits. Thus, comparing each predicted point to its prediction limit is not an effective monitoring strategy for a large number of data points. We consider the true out of control condition as occurring in three different situations when (1) the number of individual OOL points is high, (2) the number of OOL points is low but spatially clustered, or (3) the number of OOL points in one part surface is both large and highly clustered.

Figure 4.19 shows the examples of such conditions; part 1 is an example of an ‘in-control’ surface, as it is normally expected that there will be several spatially random OOL points. Pattern 2 has a similar number of OOL points; however they are clustered on the wing section of the part and thus it is more likely that the surface defects occur in that spot. Different patterns, such as those shown in Patterns 1-7, reflect different OOC

conditions and may indicate distinct root causes to aid in problem resolution. Thus, the situations patterns 1-6 should be distinguishable from each other and from the in-control part.

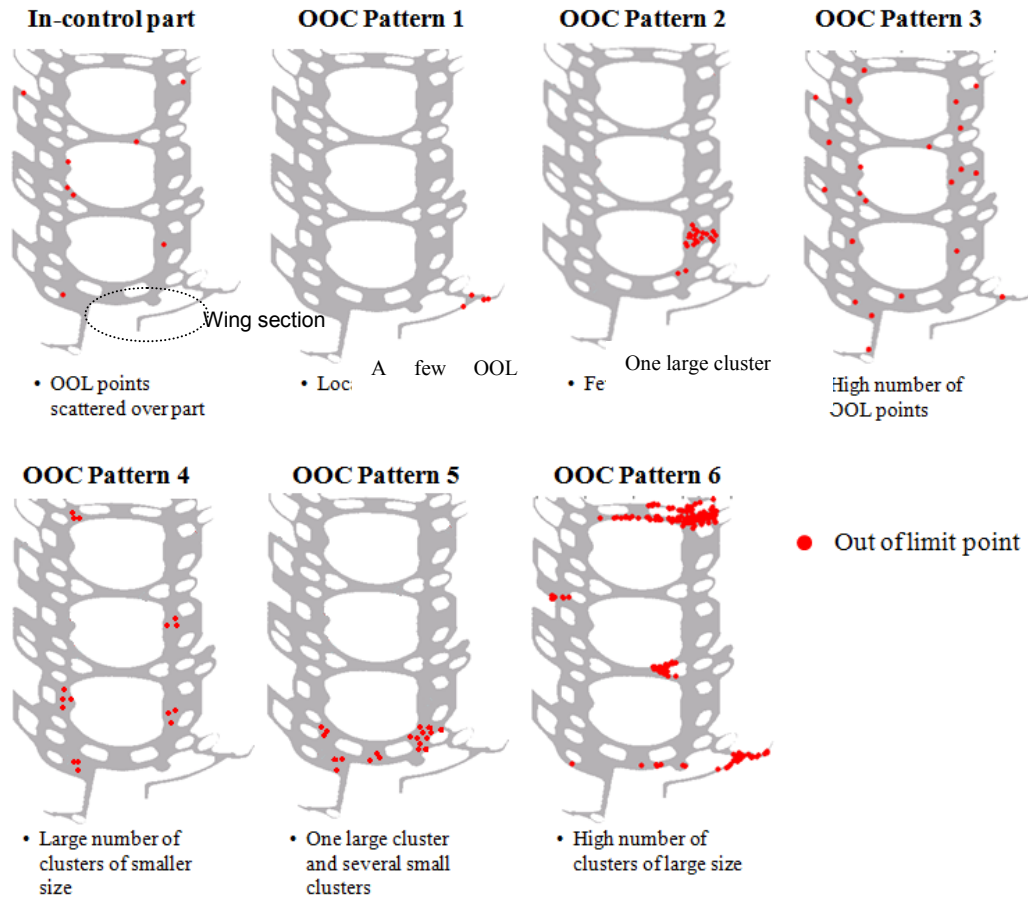


**Figure 4.19 Spatial distribution Patterns of Out of Limit Points**

Considering the OOC scenarios, the recommended characteristics for monitoring a data cloud can be the number of OOL points per surface, the size of the largest cluster of OOL points and the number of clusters in a part that are larger than a threshold size,  $s_c$ . For example, the first characteristic can detect patterns 2-4 in Figure 4.19; the second characteristic can detect patterns 1-2 and 4, and the third characteristic to be able to identify multiple cluster locations such as patterns 3-4. Denote  $k$  as the number of OOL

points on the surface of part  $i$ ,  $clust$  is the number of clusters found in the part,  $N_{i,clust}$  as the size of each cluster  $clust$  in part  $i$ , and  $S_j$  as a binary variable with value 1 when cluster  $j$  has a size larger than  $s_c$  and 0 otherwise. The three quality characteristics can be represented by

$$x_1 = k_i, \quad x_2 = \max(N_{i,clust}), \text{ and} \quad x_3 = \sum_{j=1}^{clust} S_j \quad (4-13)$$

Abnormal surface variations can be detected by jointly or individually monitoring statistics  $x_1$ - $x_3$ . This method can also identify faulty patterns and locates defective areas. To calculate  $x_2$  and  $x_3$ , it is necessary to identify OOL point clusters on a surface and determine  $s_c$ . Different from centroid method based clustering, this chapter proposes to monitor OOL point clusters that are created by a single-link merge criterion, as motivated by engineering knowledge on surface defects, i.e., many surface defects connected locally are of the same type (pores, scratches, burrs etc.). Using a *single-linkage clustering algorithm* can help distinguish between defects, and aims to find clusters such that each point in the cluster is less than a distance  $d$  away from at least one other point in the cluster. The following hierarchical agglomerative algorithm is proposed, as depicted in Figure 4.20.

*Step 0.* Find all  $n$  OOL points  $o_i$  in the surface  $i=1 \dots n$ .

*Step 1.* Calculate the upper triangular matrix  $\mathbf{D}$  of size  $n \times n$  with elements  $d_{ij}$ , where each  $d_{ij}$  is the distance between  $z_i$  and  $z_j$  for  $i=1 \dots n-1$  and  $j=1+i \dots n$ . Create an indicator matrix ( $\mathbf{E}$ ) of size  $n \times n$  where each entry is  $e_{ij}=1$  if  $d_{ij} < d$  and  $e_{ij} = 0$  otherwise. Denote the cluster that point  $i$  belongs to as  $\mathbf{E}_i$ . The initial  $\mathbf{E}_i$  is a collection of points with  $e_{ij}=1$  in the  $i$ th row of  $\mathbf{E}$ .

Step 2. For each column of matrix  $\mathbf{E}$  representing point  $i$ , find the rows where  $e_{ij}=1$ .

Combine the rows of matrix  $\mathbf{E}$  where  $e_{ij}=1$  to form clusters, i.e.,  $\mathbf{E}_i \leftarrow \mathbf{E}_i \cup \mathbf{E}_j$ .

Step 3. Continue combining clusters (rows) in Step 2 until there are no more overlapping  $e_{ij}$ 's in any pair of clusters  $\mathbf{E}_j$ . The final clusters correspond to each row in  $\mathbf{E}$ , with cluster elements denoted by  $e_{ij}=1$ .

The proposed algorithm has an advantage when there is no initial knowledge of the number of clusters present in the data and the largest possible cluster size is desired. This algorithm has a complexity of  $O(n^3)$  and other alternative algorithms for single-linkage clustering can be used [90].

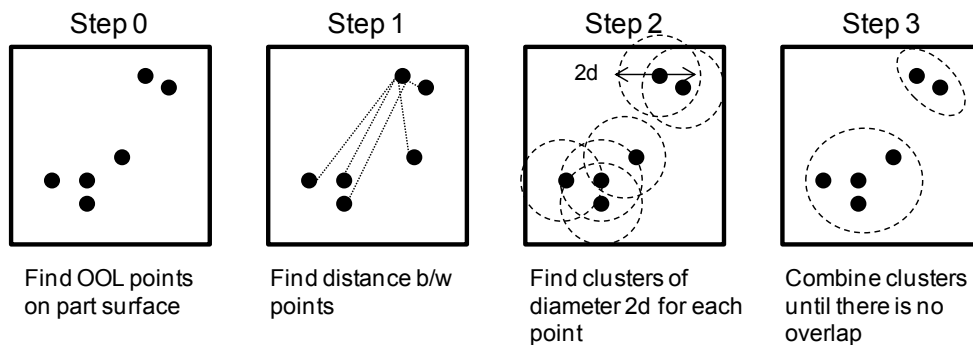


**Figure 4.20 Clustering Algorithm Steps**

Once the OOL clusters have been identified on the part surface, each quality characteristic in Equation 4-13 can be calculated and monitored by using individual control charts. Different OOC surface patterns detected based on which quality characteristic is OOC, as described in Table 4.3, which summarizes the OOC patterns of these three variables and their corresponding surface defective patterns as seen in Figure 4.19. It is important to note that some of the patterns might not have a practical



significant difference depending on the application that is being analyzed. For example, Pattern 5 displays more scattered OOL points than Pattern 4 but is otherwise the same. If a manufacturer is mostly concerned with identifying the defective clusters, both of these patterns are indicative of small defects on the surface.

**Table 4.3 OOC pattern based on individual control chart points**

$x_1$ Number of OOL pts	$x_2$ Max cluster size	$x_3$ Number of clusters greater than size $s_c$	OOO Pattern
IC	IC	IC	In control part
IC	IC	OOO	Pattern 5
IC	OOO	IC	Pattern 2
IC	OOO	OOO	Pattern 6
OOO	IC	IC	Pattern 3
OOO	IC	OOO	Pattern 4
OOO	OOO	IC	Pattern 1
OOO	OOO	OOO	Pattern 7

In addition, once an OOC condition is detected, the defective area can be located by identifying the centroid of the clusters as determined by the clustering algorithm. An area with a large number of scattered OOL points could indicate a non-local problem occurring such as surface shape change and surface texture degradation on the entire area or a measurement error. If a point is in-control, the corresponding surface measurements can be used to update the covariance parameters as outlined in section 3.1. The summary of the proposed algorithm is as follows:

A. Training

*Step A.0* Take  $t$  full resolution HDM part measurements from an in-control process.

*Step A.1* For each part

- Calculate the raw covariance and cross-covariance values of the primary variable and secondary variables using Equation 2-2.

- Choose the best fitting theoretical covariance, and estimate the covariance parameters.

*Step A.2* Estimate the distributions of parameters from Step A.1. Using MCMC, estimate the  $(1-\alpha)^{\text{th}}$  percentile at each of the prediction points given certain significant level  $\alpha$ . The percentile for each point will be used to establish the prediction limit in the implementation phase.

#### B. Monitoring implementation

*Step B.0* Measure an incoming part from the process using a combination of LDM and HDM measurements.

*Step B.1* Predict the observations at each of the desired prediction points using the median of the parameters obtained in step A.1 for the covariance and cross-covariance. Compare each of the prediction points to the prediction limits. If there are OOL points, use the clustering algorithm and plot the three individual control charts for  $x_1$ ,  $x_2$  and  $x_3$  to detect and locate the OOC (defective) patterns. If an OOC condition is found, measure the part at the specified cluster location with HDM if it is necessary to confirm the nature of the defect. Otherwise, if there are no OOC continue to Step B.2.

*Step B.2.* Use Bayesian inference to update the parameters to reflect the process changes as outlined in Section 3.1.

One note to practitioners is that further data reduction can be implemented before calculating the predictions for each desired location point. By using a clustering algorithm, points with similar height values that are clustered spatially can be treated as a single region and approximated by one single prediction point. This data preprocessing

could significantly reduce the number of prediction calculations and the computational load.

A discussion on the selection of  $d$

The value of  $d$  affects  $s_c$ . An appropriate choice for the threshold distance that determines a cluster,  $d$ , is of importance in this algorithm. A  $d$  that is too small will result in smaller clusters which may jeopardize defect detection, while a  $d$  that is too large may generate false alarms. One method of estimating  $d$  is to use engineering knowledge, e.g., the value of  $d$  should be the smallest surface defect that needs to be detected, and larger than the metrology resolution.

If there is little process knowledge, a data driven approach can be used to determine  $d$ . Such an approach should be based on minimizing the spatial spread within each cluster while maximizing the distance between the clusters. An iterative algorithm for determining  $d$  based on the single-linkage clustering can be proposed as follows. With each iteration  $w=1, 2, 3, \dots$ ,  $d$  will increase by a predetermined value, and each  $d$  is used to create clusters based on the single-linkage clustering as outlined before. Each of the  $w$  clustering schemes has  $l$  clusters that are of size 2 or greater. The optimal  $d$  should be selected by

$$\max_w \frac{\beta(d_w)}{\gamma(d_w)}, \tag{4-14}$$

where  $\beta(d_w) = \min(D_{between}^w)$  is the minimum distance between two clusters in iteration  $w$  and  $D_{between}^w$  is the distance between cluster centroids;  $\gamma(d_w) = \max(D_{within}^w)$  reflects the

spatial spread of each cluster and  $D_{within}^w = \max_i \min_j D^w(\mathbf{p}_i, \mathbf{p}_j)$  is the maxmin of the distance between OOL points  $\mathbf{p}_i$  and  $\mathbf{p}_j$  within each cluster.

### 4.2.3. Case Study

The methodology was applied to an automotive engine head deck face machining process. The measurement is to evaluate the surface flatness of the engine head joint face. In the manufacturing plant, the surface flatness is currently assessed through two measures: the overall flatness, which is the range of surface height variation, and the 25 mm span flatness, which is the surface variation range in a 25 mm square region. The manufacturing plant uses a coordinate measurement machine (CMM) to make traces, as seen in the second panel of Figure 1.1, to calculate both flatness measures. Each of the CMM measurements contains approximately 800 points which roughly outline the surface topography. In addition, a profilometer is used to measure fine-scale details on predetermined surface areas. Although the surface flatness and 25 mm span flatness are the critical features used to monitor the process, these two measurements may be insufficient to identify abnormal local variations. This study applies the proposed algorithm to monitor local surface variations and shape changes.

Since ten automotive engine heads (Parts 1-10) were already measured by an HDM system (a laser holographic interferometer with lateral resolution 150  $\mu\text{m}$ ) at a Ford engine plant, without losing generality, we used these measurements to generate simulated CMM and profilometer data for simplicity. The HDM measurements also provide training data and validation for implementation phase. Two of these parts have defective areas possibly due to chatter during machining that are on a spot in the top right

wing area (Part 9) and a few spots in a bridge area between the bores (Part 10). The procedure of generating the simulated data from the real HDM data is as follows. From each HDM surface measurement, 100 points were selected to simulate the CMM plant measurements, and four patches (size  $5 \times 5 \text{ mm}^2$ ) consisting of 50 points each were chosen to simulate the profilometer data. Eight automotive engine heads were used as the training data, and an additional two defective engine heads used as implementation data to validate the methodology.

#### ***4.2.3.1. Cross and Spatial Correlation***

In the automotive engine machining process, there are several process variables that are correlated to surface height, such as MRR or axial cutting force variations. When the feed rate, depth of cut and tool path are assumed constant, the MRR can be measured using the cutting arc length as determined by part geometry. As shown in Section 2.1 and in the scatterplot in Figure 4.21 the MRR is highly correlated to  $Z_{HD}$ . Thus, considering the ease of measurement and such a positive correlation pattern, the MRR variable was selected as a secondary variable to predict the surface.

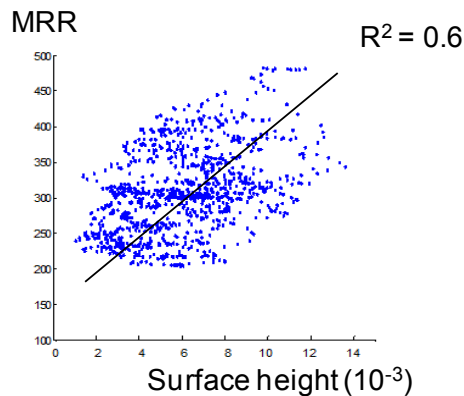


**Figure 4.21 Scatter Plot of MRR vs. Surface Height**

#### 4.2.3.2. *Monitoring of surface variations*

Ten parts were measured using an HDM laser interferometry system. Eight parts were normal, in-control parts, and 2 were defective parts. For each of the in control training parts, the theoretical exponential variograms were calculated based on the full HDM data set. Based on these theoretical variograms, the distributions for each of the unknown parameters were estimated:

$$\begin{aligned}\beta &\sim \text{unif}() \\ \phi &\sim \text{unif}(0.1,3) \\ \sigma^2 &\sim IG(2,0.35) \\ \tau^2 &\sim IG(2,1.04e-5)\end{aligned}\tag{4-15}$$

Based on the parameter distributions, MCMC was used to find the prediction distributions at each prediction location for each surface. The corresponding 95th percentile of each prediction point was used as a prediction limit for each individual point.

Figure 4.22 shows the predictions for one of the normal parts and the two defective parts. It can be observed that Part 9 had a relative higher spot in the top right wing area while Part 10 had several higher spots on the bridges areas which may be due to excessive vibration or chatter.

After estimating the predictions at each of the prediction locations, the summary variables were calculated, as shown in Table 1, where  $x_1$  =number of OOL points per surface,  $x_2$  = size of the biggest cluster of the OOL points and  $x_3$  is the number of clusters of size 5 and larger. To obtain  $x_2$  and  $x_3$ , the single-linkage clustering algorithm presented in Section 3.2 was used based on  $d = 450\mu\text{m}$ , which was selected considering the size of chatter defect of interest, i.e.,  $750\mu\text{m}$ .

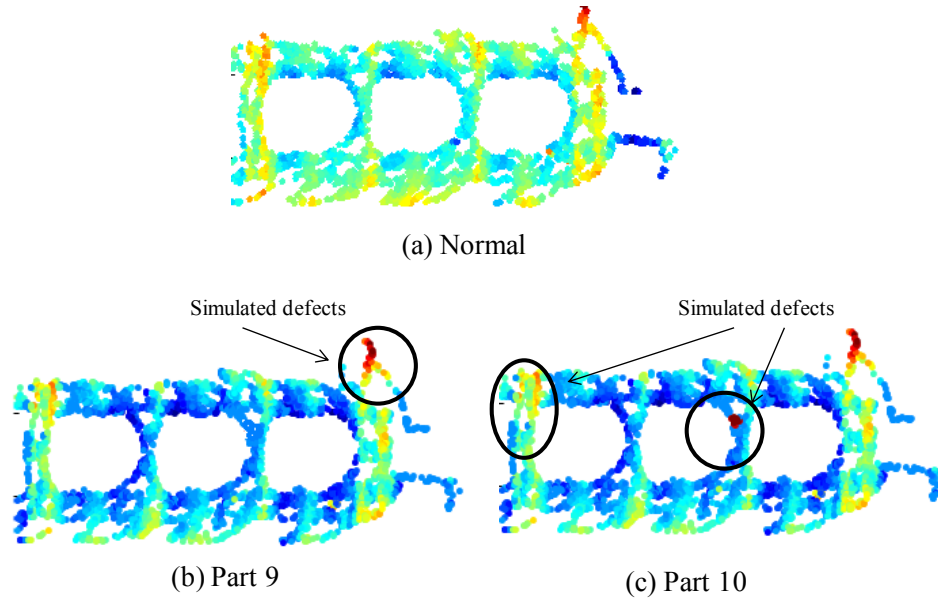


**Figure 4.22 (a) Normal Part (b) Defective Part**

Using the measurements in Table 4.4, the three characteristics were plotted on individual control charts (Montgomery, 2010) over the ten parts, and the results shown in

Figure 4.23. A c chart was chosen for  $x_1$  and  $x_3$  since they are count data, and an individual control chart was chosen for  $x_2$ . As seen in the control charts, both Part 9 and 10 result in OOC points in the charts. Part 9 is OOC for  $x_1$  and  $x_2$ , which indicates that the number of clusters is low, but these clusters are large. Part 10 is OOC for all three quality characteristics, thus indicating that there are many clusters of large size.

**Table 4.4 Values of Quality Characteristics for Monitoring**

Part	$x_1$	$x_2$	$x_3$	Part	$x_1$	$x_2$	$x_3$
P1	8	1	4	P6	8	1	4
P2	4	1	0	P7	9	1	5
P3	7	1	3	P8	4	2	0
P4	5	1	1	P9	35	24	4
P5	10	2	5	P10	183	110	10

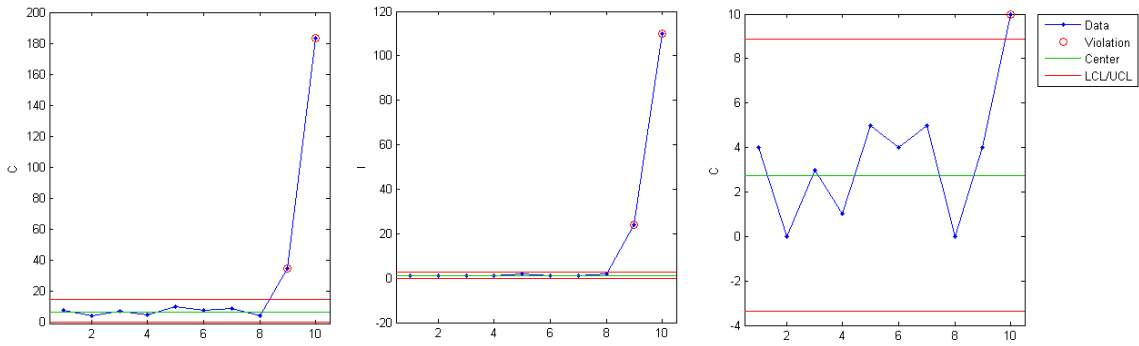


**Figure 4.23 Surface Variation Monitoring**

As shown in Figure 4.24, the methodology was able to identify defective clusters effectively. The centroids from the identified clusters can pinpoint the location of the defective surface areas.

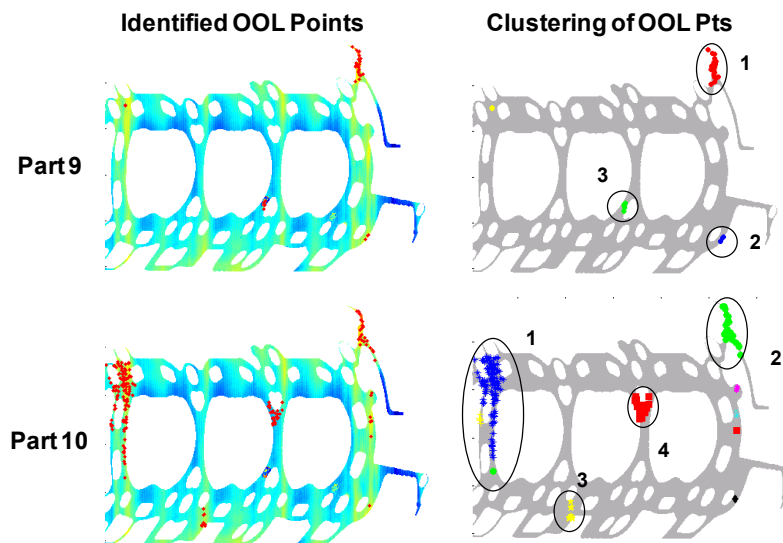


**Figure 4.24 OOL points for Normal and Defective Parts**

### 4.3. Chapter Summary

This chapter presents an improved sequential strategy to monitor a high precision machining process using HDM data and applies it to an automotive engine head machining process. The overall spatial features were monitored using a multivariate PCA chart. When an out of control condition was detected, the defective surface region was



localized by using individual EWMA control charts. To reduce computational load, K-means clustering was used to determine the partition of the part surface efficiently. Finally, a variogram-based profile monitoring was proposed to monitor small scale features and localize defects. This method was able to detect a defective sample, as well as characterize the defect.

In addition, a measurement and monitoring method for surface variation control for process and HDM fusion data is proposed. An engineering-driven surface model with improved prediction is first established by incorporating the cross correlations between surface height and machining process variables in conjunction with the spatial correlation. The prediction distributions are estimated using sampling method such as MCMC to build control limits based on in-control data. A Bayesian framework is adopted to update surface model parameters and control limits for monitoring of high-dimensional data. Based on the model, a new monitoring method of high-dimensional data is established and demonstrated by a case study of an engine head machining process.

Compared with the previous approaches, the proposed method has the following advantages:

- *Reduction of measurement cycle time through surface modeling using spatial and cross-correlation between the surface data and significant process variables:* The model reduces the number of measurements needed by supplementing lower lateral resolution measurement with process variable information which can be quickly measured at lower cost. In addition, if confirmation of the nature of defects is necessary, more HDM measurements

can be implemented only on the detected areas. Therefore this method is more efficient than performing full resolution HDM measurements over the entire surface.

- *Progressive measurement strategy for monitoring high-dimensional data enabled by the Bayesian framework:* The strategy does not require a large number of samples at one time to estimate the distribution of model parameters and instead collect/update surface information incrementally. Thus, the progressive strategy is more time efficient in measuring and monitoring high-dimensional data.
- *New single-linkage algorithm for monitoring high-dimensional data:* The proposed algorithm can jointly detect and locate abnormal surface shape variations without significantly increasing false alarm.

**CHAPTER 5**

**MULTISTAGE MODELING AND MONITORING OF HIGH DEFINITION**

**METROLOGY DATA**

In multistage manufacturing processes (MMP), a machined surface may change its shape as it goes through each stage because a downstream operation can change the surface characteristics generated from a prior upstream operation. For example, Figure 5.1 shows a workpiece going through a face milling operation (Stage  $i$ ) that mills its top surface followed by a hole drilling operation on its side (Stage  $i+1$ ). Due to the drilling torque, the top surface is twisted, thus creating a local height variation. Monitoring of such multistage surface variation is important for root cause diagnosis by identifying the effects of the relationships between stages. The multistage surface monitoring is also a key enabler of an “inter-stage” compensation strategy to reduce surface variations. For example, to compensate for the distortion introduced at a downstream stage, one can generate a “reverse” distortion on the part surface at an upstream stage so that the downstream stages could create a part with a flat surface (Figure 5.1). Thus, the monitoring of the surface variations at intermediate stages can ensure the appropriate adjustments are applied to create the desired surface shape.

A new methodology is needed to efficiently monitor multistage surface variation. In this chapter, a functional morphing approach is used to model the interdependence between stages, such that an end-of-line measurement can be morphed backward into a surface estimate at any upstream stage. To monitor an intermediate stage, a surface prediction is calculated using the surface-process fusion data model proposed in Chapter 2. Based on the prediction, the abnormal surface variations are detected and located using a single-linkage cluster monitoring algorithm, as proposed in Chapter 4.

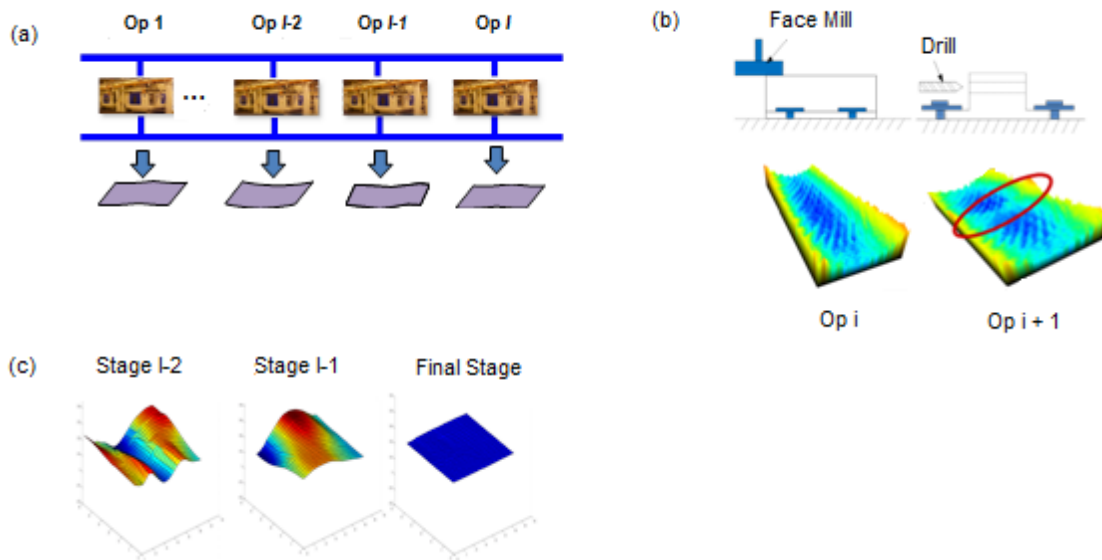


**Figure 5.1 (a) Part surface Changes in Multistage Process (b Two-stage machining Process Part Measurements (c) Inter-stage Surface Shape Compensation [3]**

The chapter is organized as follows: Section 5.1 reviews the morphing based monitoring algorithm as developed in [3] and identifies the limitations of the approach. An improved morphing based monitoring method is developed in Section 5.2, which is demonstrated using a two-stage machining process in Section 5.3. Section 5.4 summarizes this chapter.

## 5.1. Background: Modeling of Multistage Interdependence using Functional Morphing

Previous research using a high-definition metrology (HDM) system modeled the between-stage interdependence through a functional morphing method, providing opportunities for multistage surface variation improvement. This section provides fundamental background of this approach and discusses its limitations.

The functional morphing concept is briefly reviewed here; for more details, refer to [91-93]. Consider a multistage manufacturing process with  $I$  stages, consisting of the initial part (stage 0) through the final stage  $I$ . Assume that the surfaces from stage  $i$  and  $i+1$  are defined by the surface grids  $S^i$  and  $S^{i+1}$  respectively and  $T^{i+1,i}$  is defined as the mapping function from stage  $i$  to  $i+1$ .

The cubic Free Form Deformation (FFD) is then defined as

$$\begin{aligned} (x \quad y \quad z) &= \sum_{l=0}^3 \sum_{m=0}^3 \sum_{n=0}^3 B_l(u) B_m(v) B_n(w) \Phi_{l,m,n} \\ &= \sum_{l=0}^3 \sum_{m=0}^3 \sum_{n=0}^3 B_l(u) B_m(v) B_n(w) \left[ \Phi_{l,m,n}^X \quad \Phi_{l,m,n}^Y \quad \Phi_{l,m,n}^Z \right] \end{aligned} \quad (5-1)$$

where  $(u, v, w)$  are localized coordinates corresponding to the global coordinates  $(x, y, z)$  and  $B_0(t), B_1(t), B_2(t)$  and  $B_3(t)$  are the uniform cubic B-Spline blending functions defined in Equation 5-2. The lattice points  $\Phi_{i,j,k}$  define the FFD volume space. The global coordinates  $(x, y, z)$  are derived using cubic spline interpolation of their local coordinates  $(u, v, w)$  and corresponding  $\Phi_{i,j,k}$ .

$$\begin{aligned} B_0(t) &= (-t^3 + 3t^2 - 3t + 1) / 6 \\ B_1(t) &= (3t^3 - 6t^2 + 4) / 6 \\ B_2(t) &= (-3t^3 + 3t^2 + 3t + 1) / 6 \\ B_3(t) &= t^3 / 6 \end{aligned} \quad (5-2)$$

If surface  $S^i$  has the dimension of  $(d_1 \times d_2)$ , at the initial stage 0, the local coordinates  $(u_a, v_a, w_a)$  of point  $S_a^0$  in  $S^0$ ,  $a = 1 \dots d_1 \times d_2$ , are determined by

$$S_a^0(u_a, v_a, w_a)|_0 = \sum_{l=0}^3 \sum_{m=0}^3 \sum_{n=0}^3 B_l(u_a|_0) B_m(v_a|_0) B_n(w_a|_0) \cdot \Phi_{l,m,n}^0 \quad (5-3)$$

where  $\Phi^0$  is the initial FFD volume space. The notation  $\bullet|_0$  denotes that  $\bullet$  is measured at stage 0. The surface grid at any stage  $S^i$  can be generated by deforming the volume space  $\Phi$ , such that any point  $a$  on  $S^i$  can be expressed as,

$$S_a^i|_0 = (\hat{X}_{morph}^i, \hat{Y}_{morph}^i, \hat{Z}_{morph}^i) = \sum_{l=0}^3 \sum_{m=0}^3 \sum_{n=0}^3 B_l(u_a|_0) B_m(v_a|_0) B_n(w_a|_0) \cdot \Phi_{l,m,n}^i \quad (5-4)$$

where  $\Phi^i$  is the FFD volume space at stage  $i$ .

Given the initial lattice  $\Phi_{i,j,k}^0$  and the global coordinates  $(x, y, z)$ , the local coordinates  $(u, v, w)$  corresponding to the initial lattice can be found. If the lattices in  $\Phi_{i,j,k}^0$  are equally spaced, the solution can be simplified to

$$u = \frac{x}{n_x} - \left\lfloor \frac{x}{n_x} \right\rfloor, \quad v = \frac{y}{n_y} - \left\lfloor \frac{y}{n_y} \right\rfloor, \quad \text{and} \quad w = \frac{z}{n_z} - \left\lfloor \frac{z}{n_z} \right\rfloor, \quad (5-5)$$

where  $\lfloor \cdot \rfloor$  denotes the floor rounding function. The  $\Phi^i$  are calculated by minimizing a distance function,  $g_1$ , between the two surfaces  $S^i$  and  $S^{i+1}$ , such that

$$\mathbf{Min}_{\Delta\Phi^{i+1,i}} (1-\alpha)g_1(S^i|_i, S^{i+1}|_{i+1}) + \alpha \cdot J \quad (5-6)$$

where  $\alpha$  takes values between 0 and 1, and  $J$  is the bending energy of the workpiece, representing the bending energy that is derived from the strain energy associated with a small deflection of a thin plate [3]. A higher  $\alpha$  value places more weights on the smoothness of the transformation. Inclusion of the bending energy term reduces the solution space for the optimization problem and allows the identification of a mapping

function that transforms a surface to an equilibrium state due to the Principle of Minimum Potential Energy. Therefore, Equation 5-6 combines data-driven image morphing with the bending energy term which provides part physical insights to characterize the morphing function. Unlike conventional morphing algorithms in computer graphics that focus on transformations between geometries only, the functional morphing integrates process physical insights into the geometric mappings, thereby characterizing the shape changes in physically meaningful ways.

Continuous forward mapping determines the volume space at any stage after measurement  $i$  through the summation of all the mapping functions from stage  $i$  to  $j$ . Define  $\Delta\Phi^{j,i}$  as the deformation of FFD volume space from stage  $i$  to  $j$ ; then the volume space at stage  $j$  can be obtained by

$$\Phi^j = \Phi^i + \Delta\Phi^{j,i} = \Phi^i + \Delta\Phi^{i+1,i} + \dots + \Delta\Phi^{j,j-1} \quad (i \leq j) \quad (5-7)$$

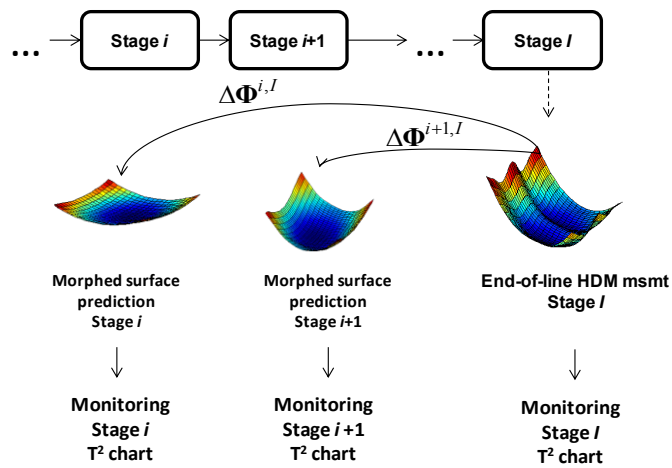
Similarly, when the final surface  $S^I|_I$  measured at stage  $I$  is obtained, the surface shape at any previous stage  $i < I$  can be estimated by using a backward mapping function, which is derived based on the forward mapping function by using the same FFD volume space  $\Phi^i$  ( $i=1..I$ ) at each stage. Given the final surface  $S^I|_I$ , Equation 5-5 can be used to determine the local coordinates  $[u \ v \ w]^I|_I$ . Thus, the continuous mapping suggests that the FFD volume space at any stage is determined by the summation of all mapping functions from stage  $I$  to  $i$  ( $i \leq I$ ).

$$\Phi^i = \Phi^I + \Delta\Phi^{i,I} = \Phi^I + \Delta\Phi^{I-1,i} + \dots + \Delta\Phi^{i,i+1} \quad (5-8)$$

where  $\Delta\Phi^{i,i+1} = -\Delta\Phi^{i+1,i}$ . The forward and backward mapping function enables a surface prediction based on a single HDM measurement.

## 5.2. Multistage Monitoring using Functional Morphing and Spatial Correlation

A process monitoring methodology was developed by monitoring the backward morphed surfaces, as illustrated in Figure 5.2. An end-of-line measurement is used to predict the surface at the intermediate stages by using the appropriate morphing function. The predicted surfaces are then monitored at each intermediate stage individually through a multivariate chart. This methodology successfully captures the variation propagation under normal process conditions, thus eliminating the need for measurements after the intermediate stages.

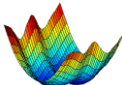
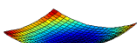
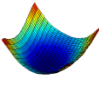
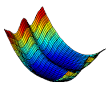
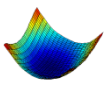
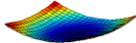


**Figure 5.2 Monitoring using Backward Morphing**

When monitoring new incoming surfaces, this method can lead to misdetection or false alarm errors that may arise from using a backward morphed prediction calculated by in-control training data. Figure 5.3 shows two examples when the prediction from backward morphing does not reflect the state of the intermediate stage  $i$  accurately. The first column in the figure is the observed HDM measurement at the final stage. A false alarm will be caused when an abnormal surface is seen in the final stage, but there was no abnormality in the intermediate stage. For example, an error in a stage occurring after



stage  $i$  can propagate to the final stage, resulting in an incorrect backward morphed prediction at stage  $i$ . Conversely, a misdetection can occur if the morphed prediction at the final stage is normal, but the actual surface at stage  $i$  has abnormal variation. Thus, for root cause diagnosis and control purposes, it is necessary to ensure that the backward morphed surface for the intermediate stage is an accurate prediction of the surface shape without needing an HDM measurement at each intermediate stage.

	Final Stage $l$	Intermediate Stage $i$	
	Measurement	Backward morphed prediction from $\Delta\Phi^{i,l}$	Actual surface
FALSE ALARM	 abnormal	 abnormal	 normal
MISDETECTION	 normal	 normal	 abnormal

**Figure 5.3 False alarm and Misdetection Scenarios Using Backward Morphing**

This chapter proposes to reduce false alarms and misdetections of a functional morphing based monitoring framework by improving the multistage surface prediction through the incorporation of limited intermediate stage measurements and the effect of process variables. End-of-line HDM measurements are used to create a backward morphed surface prediction at the intermediate stage of interest. Then, the multistage surfaces are predicted by developing an improved surface model that combines the morphed surface and effect of process variables with low-resolution measurements at intermediate stages. Based on the surface model, abnormal surface variations are detected

and located by the single-linkage cluster surface monitoring algorithm as developed in our previous work.

It is assumed that surface measurements for multistage monitoring can be carried out in two ways: (1) multi-resolution measurements, which can be either from HDM (Figure 5.4a) or from a combination of metrology systems such as CMM and profilometer (Figure 5.4b) and (2) low-resolution measurements over the part surface.

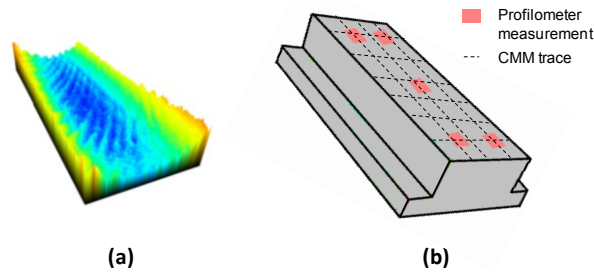


**Figure 5.4 Part Surface Measurements using (a) HDM and (b) Multi-resolution Metrology (CMM and profilometer)**

The multistage surface monitoring consists of two steps. Consider a multistage manufacturing process with  $I$  stages. Define the surface  $Z^i(\mathbf{s})$  at stage  $i$ , where  $i=1 \dots I$ , at locations  $\mathbf{s}=(x,y)$ . In step I, multi-resolution measurements after each stage are measured to establish the backward morphing functions. To monitor the process in step II, multi-resolution measurements are carried out on incoming part surfaces  $Z^I(\mathbf{s})$  at the final stage  $I$ . By applying the backward morphing function to the observed surface at stage  $I$  as in (8), we can predict the surfaces at intermediate stages  $1 \dots I-1$ , denoted as  $\hat{Z}_{morph}^{i \leftarrow I}$ . Meanwhile, low-resolution measurements at each of the intermediate stages,  $Z^i(\mathbf{n}_j)$ , are carried out at locations  $\mathbf{n}_j=(x_j,y_j)$ ,  $j=1 \dots I$ . The final predicted surface at the intermediate stage can be estimated by combining morphed prediction and the observed measurements, such that  $Z^i = f(\hat{Z}_{morph}^{i \leftarrow I}, Z^i(\mathbf{n}_j)) + \varepsilon$ . Integrating the limited measurements with

the backward morphed prediction at the intermediate stages can reduce the false alarms and misdetection scenarios shown in Figure 5.3.

Various models can be adopted to expand  $f()$ . As proposed in previous chapters, a hierarchical spatial Bayesian approach was chosen due to the complex variation structure of the spatial data. The surface model proposed in Chapter 2 can then be expressed as

$$Z^i(\mathbf{s}) = \mu(\mathbf{s}) + w(\mathbf{s}) + \varepsilon(\mathbf{s}), \quad \text{where} \quad (5-9)$$

Mean	$\mu(\mathbf{s}) = \beta_1 + \beta_2 \hat{Z}_{morph}^{i-1}$
Covariance	$w(\mathbf{s}) \sim \text{GP}(0, \sigma^2 \rho(\phi; \ \mathbf{s}_i - \mathbf{s}_j\ ))$
Error	$\varepsilon(\mathbf{s}) \sim N(0, \tau^2)$

The mean of the expression,  $\mu(\mathbf{s})$  is modeled as a deterministic function in terms of the backward morphed surface, and the residuals,  $w(\mathbf{s})$ , are modeled as a spatial process with mean zero and variance  $\sigma^2 \rho(\phi)$ , where  $\rho(\phi)$  is the exponential correlation of the form  $\exp(-\phi \|s' - s\|)$ , and the error  $\varepsilon(\mathbf{s})$  is normally distributed with mean zero and variance  $\tau^2$ .

The prediction distribution of  $Z^i(\mathbf{s})$  in Equation 5-9 can be estimated by a three step data model, such as in Chapter 2. After the HDM predictions are obtained, the single linkage cluster monitoring framework as proposed in Section 4.2 is used to monitor the process and locate defective regions when abnormal process variation exists.

*Discussion: surface model improvement using cross correlation*

The number of measurements needed at the intermediate stages can be further reduced by utilizing process variables that are highly correlated with the surface shape. A correlated process variable  $U^i$  such as the cutting arc length discussed in Chapter 2 can be incorporated into the prediction model for  $Z^i$  as a covariate such that

$$Z^i(\mathbf{s}) = \mu(\mathbf{s}) + w(\mathbf{s}) + \varepsilon(\mathbf{s}) \quad \text{where}$$

$$\mu(\mathbf{s}) = \beta_1 + \beta_2 \hat{Z}_{morph}^{i \leftarrow 1} + \beta_3 U^i. \quad (5-10)$$

It is important to note that variables should only be included in the model if they improve the prediction accuracy. A variable selection method is needed to determine the key process variables that mostly contribute to surface variations. Methods for comparing the models, such as subset selection and Lasso method can be used for the variable selection.

The proposed approach for multistage monitoring is summarized in Figure 5.5. Compared to the framework in Figure 5.2, improved predictions are obtained by adding low-resolution measurements at the intermediate stages and the effects of process variables.

### 5.3. Case Study

The proposed method was applied to a two-stage machining process, such as the one seen in Figure 5.1(b). In stage 1, the top surface of one workpiece was milled, and in stage 2, one hole was drilled on its side. The workpiece was measured before and after each stage while still on the adapter plate using a HDM system based on laser holographic interferometry (x-y resolution: 150 $\mu$ m and vertical resolution: 1 $\mu$ m). Figure 5.6 shows surfaces at each stage after filtering. It can be seen that the drilling induces a distortion on the part surface, creating a slight bump in the middle of the part due to drilling torque.

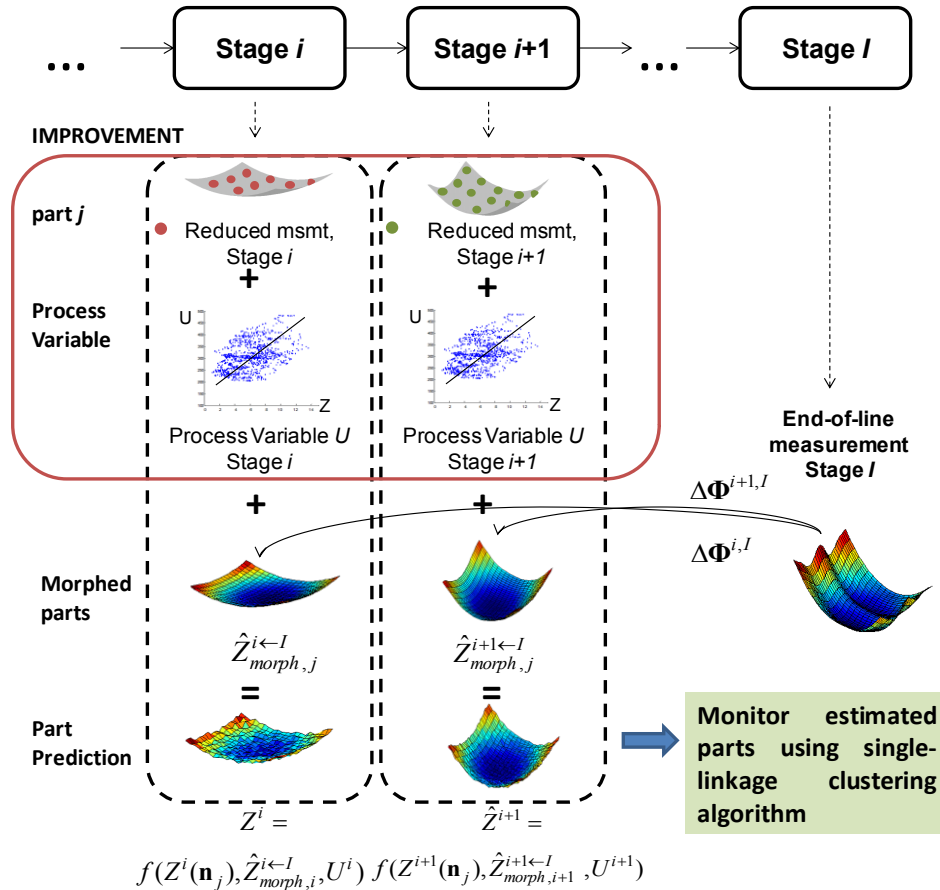


Figure 5.5 Proposed Monitoring Framework for Multistage Processes

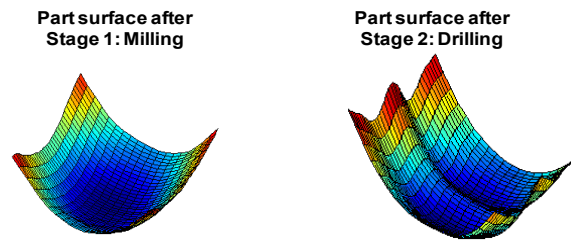
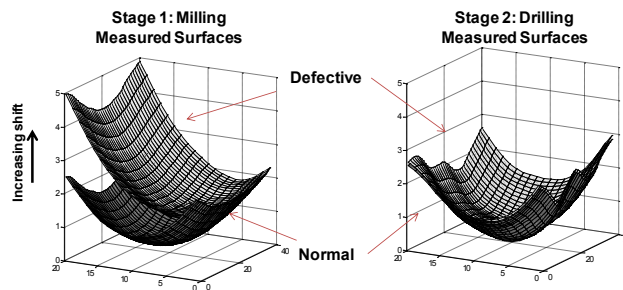


Figure 5.6 Part Surface (a) After Milling and (b) After Drilling

The measured surface was projected onto a rectangular grid. The optimization parameters and morphing function  $\Delta\Phi^{1,2}$  were calculated based on the projected surface. A total of fourteen parts were simulated and each part was measured with low resolution (10 points) after stage 1 and with high resolution after stage 2. Seven parts were assumed to come from a normal process, and for the remaining seven parts a small mean shift was

introduced at the milling stage. Figure 5.7 shows an example of a normal surface in dark color and a defective surface in gray at each stage. Parts 8-14 have an increasing mean shift of up to  $3\mu\text{m}$  at stage 1. At the drilling stage, the defective parts were not noticeably different than the normal parts, and the mean shift is only assumed to exist in Stage 1. There were no measured data available for correlated process variables and the cross correlation patterns are not considered.



**Figure 5.7 Normal and Defective Part Surfaces after Stage 1 and 2**

*Surface modeling considering multistage interdependence*

A hierarchical model as in Equation 5-10 was fit to the data. To define the parameter prior probabilities, the cross covariance parameters for the residuals were calculated from four normal parts as shown in Table 5.1.

**Table 5.1 Cross-Covariance Parameters for Model Residuals**

Part	$\sigma^2$	$\phi$	$\tau^2$
1	0.00025	0.5	0.00003
2	0.00018	0.75	0.00002
3	0.00012	0.375	0.00002
4	0.00015	0.375	0.00001

The observed samples in Table 5.1 were used to estimate the prior distributions for  $\tau^2$ ,  $\sigma^2$  and  $\phi$ , such that

$$\begin{aligned}
\beta &\sim dflat() \\
\tau^2 &\sim IW(2, 0.00014) \\
\sigma^2 &\sim IW(2, 0.00002) \\
\phi &\sim unif(0.1, 1)
\end{aligned}
\tag{5-11}$$

Noninformative priors were chosen for  $\beta$  and  $\phi$ ; and the variances  $\tau^2$  and  $\sigma^2$  were assumed to have an inverse Gamma distribution, which is a conjugate prior to the multinormal distribution model assumed for  $Z$ . The predicted surface was obtained using Markov chain Monte Carlo (MCMC) with Gibbs sampling.

### *Surface model validation*

To demonstrate the improved accuracy of the proposed surface model, the results from the following three prediction models of the part surface are compared: (1) A spatial Kriging model using the limited measured data from Stage 1, (2) the backward morphed prediction, and (3) the hierarchical model using the limited measurements and the backward morphed surface as a covariate. Figure 5.8 shows the predictions from each of the models outlined above for an in-control surface and the corresponding root mean squares (RMS). The RMS values show that using either model 2 or model 3 results in a more accurate surface prediction for an in-control part. Table 5.2 shows the average RMS for the 14 case study parts using each model stratified by normal and defective parts. The RMS values indicate that both surface models 2 and 3 are comparable when the process is normal (that is, the low-resolution measurements after milling do not improve the prediction accuracy). However, when there is a mean shift, model 3 is superior to model 2. The improved prediction precision is explained by examining how  $\Delta\Phi^{1,2}$  is calculated. The morphing function is calculated from normal and in-control parts, thus, if there is a change in the multistage interdependence, it will not be reflected in the  $\Delta\Phi$ 's. Therefore,

model 2 will not produce an accurate prediction in the instance where the error is not noticeable at the end-of-line measurement. Thus, a surface model which incorporates both the low-resolution observations from Stage 1 and the backward morphed prediction provides the most robust results.

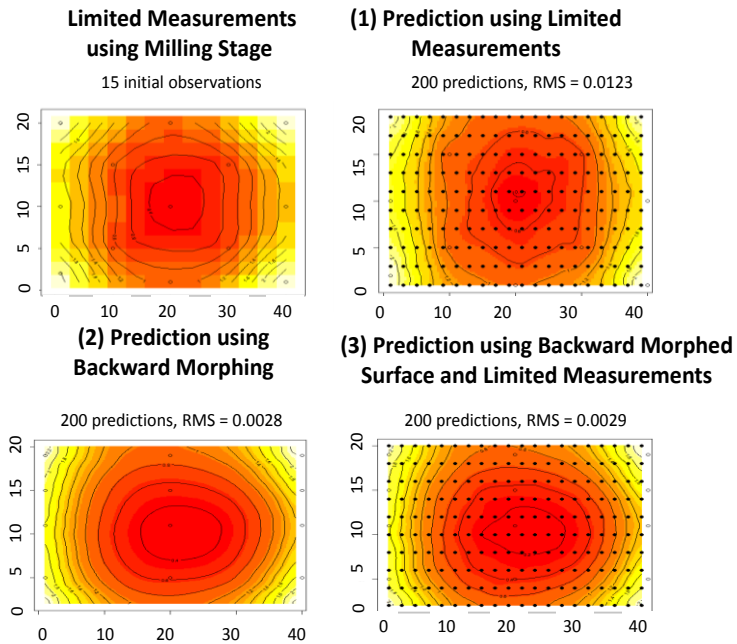


**Figure 5.8 Predicted Surfaces for Several Models**

**Table 5.2 Average Surface Prediction RMS for each Surface Model**

	Prediction Method RMS		
	(1) Limited Observations	(2) Morphing Prediction	(3) Morphing + Limited Obs.
<b>Normal Parts</b>	0.0155	0.0032	0.0032
<b>Defective Parts</b>	0.0235	0.0469	0.0243
<b>Average</b>	<b>0.020</b>	<b>0.025</b>	<b>0.014</b>



### *Surface Variation Monitoring*

The proposed methodology in [3] uses a Hotelling  $T^2$  multivariate chart of the principal components (PC) of each surface to monitor stage quality. For the purposes of comparison, the same method was used on the Stage 1 data using the (a) part estimates obtained from morphing and (b) part estimates obtained from the Bayesian model combining the morphed estimate with limited measurements. The resulting control charts are shown in Figure 5.9.

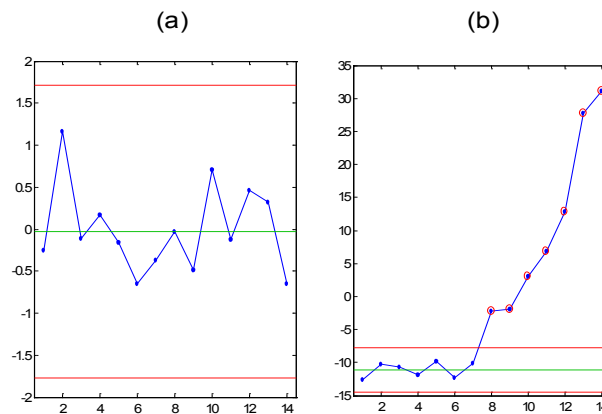


**Figure 5.9 Individual Monitoring Charts for Stage 1 using (a) Morphed Estimates and (b) Morphed Estimates Adjusted using Limited Measurements**

It was determined that the first PC contributed to 98% of the variation of the data, and thus, only the first PC was used to monitor the process using an individual control chart. While the control chart using the combination of measurements was able to capture the mean shift, the control chart using only the morphed estimates was not, demonstrating that the proposed methodology is able to prevent the missed detection of surface errors at intermediate stages.

The single-linkage clustering monitoring method proposed in Chapter 4 can be used to monitor the surface variation for defect location. The resulting control charts using the

single linkage method are shown in Figure 5.10, with the control limits established from the seven normal, in-control parts. It can be seen that the simulated mean shift introduced after Part 7 was immediately detected due to an increased proportion of defective points and large cluster size.

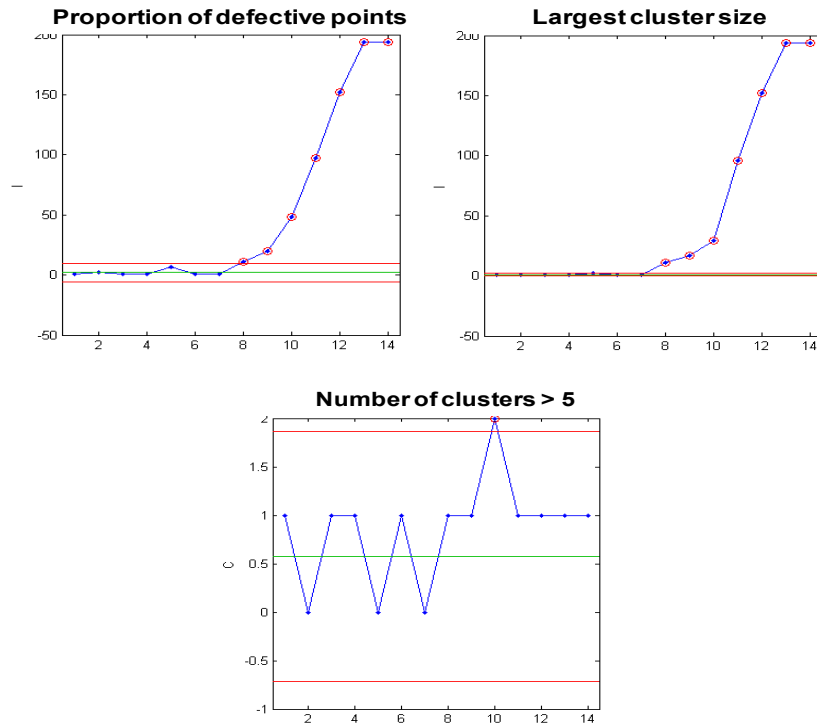


**Figure 5.10 Monitoring of OOC Patterns using Control Charts for Upstream Stage**

The single-linkage cluster monitoring method can also locate the defective area by identifying the cluster centroids. A visual rendering of the cluster locations for some of the normal and defective parts can be seen in Figure 5.11. For the normal parts, there are only a few OOL points, each far apart from the rest. The first part after the mean shift, Part 8, shows a cluster in the top left corner of the part, and as the mean shift increases, the OOL clusters get larger and merge. Therefore, the methodology can effectively detect and locate defective surface areas.

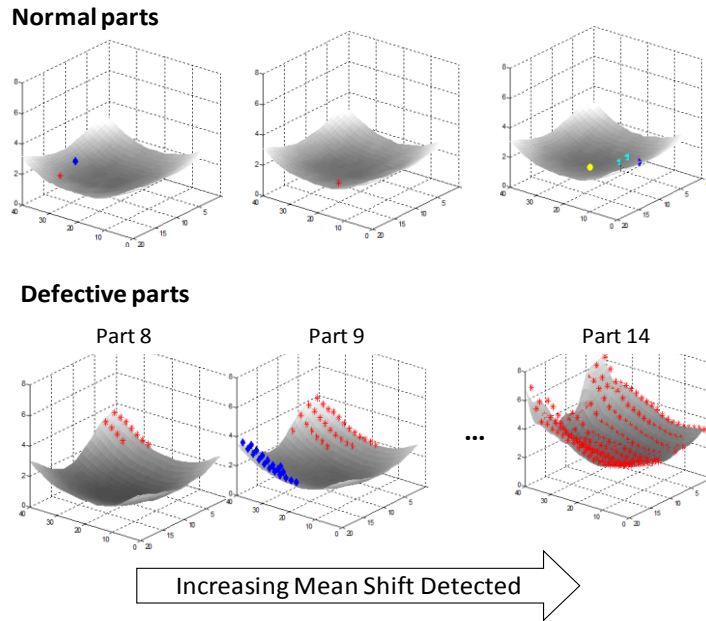


**Figure 5.11 Cluster Locations for Normal and Defective Parts for Upstream Stage**

#### 5.4. Chapter Summary

This chapter presents a monitoring method for multistage surface variation control using morphing and multi-resolution surface data. The variation propagation is modeled using a functional morphing approach, which also provides a backward morphing prediction at the intermediate stages. The final surface prediction at the intermediate stages is obtained by using a hierarchical Bayesian model. The surface prediction is then monitored using a single-linkage cluster monitoring approach. The methodology was applied to a two-stage machining process, where a defective area in the intermediate stage was detected and located successfully.

The proposed method has the following advantages:

- *Measurement reduction for multi-stage surface monitoring:* The methodology eliminates the need of high-resolution surface measurement after each stage by

using the combination of morphed surface predictions, reduced measurements, and easy-to-measure process variables to model the surface.

- *Reduction of false alarms and misdetection:* The previous functional morphing approach uses a deterministic morphing function established from normal parts. However, the backward morphed surface prediction leads to misdetections and false alarms at the intermediate stage. By establishing a model which incorporates in-production measurements at the intermediate stage, the surface prediction accuracy increases when abnormal variations are present.

## CHAPTER 6

### CONCLUSION

#### 6.1. Conclusions

Metrology innovations have enabled new opportunities for HDM data based process control of high precision manufacturing processes. This dissertation developed a novel surface data-process fusion model to utilize the spatial correlation in surface data and cross-correlations between the HDM data and process variables for process control and improvements. Based on the surface model, methods were developed for measurement system analysis (MSA), surface variation monitoring and inter-stage monitoring using HDM data. A detailed summary of the dissertation is given below:

1. *Surface Modeling through Fusion of Process Information and HDM Data.* An engineering-driven surface prediction model was developed by incorporating the cross correlations between surface height and machining process variables in conjunction with the spatial correlation. This new model enables HDM based process control by reducing the number of HDM measurements required for analysis. A case study demonstrates the improved accuracy of the model prediction while decreasing the number of HDM measurement points needed.
2. *Measurement System Analysis for HDM using Cross-Correlation.* An engineering-driven MSA method for planar and volumetric HDM systems was developed. The

measurement data was pre-processed using the fusion model to improve the precision of the measurement interpolation. A comparison of several data reduction techniques and their impact on the capability estimate was performed. Case studies were conducted which demonstrated the advantages of using the proposed method over current industry practices. The proposed method provides an engineering driven MSA methodology for HDM data.

3. *Surface Variation Monitoring using HDM.* Methods for monitoring processes using HDM data and for monitoring multi-resolution fusion data using cross-correlation were developed as follows:
  - a. *Sequential Monitoring for HDM data.* In this framework, the HDM data was decomposed to efficiently monitor the large and small scale surface variations. The large scale HDM data features were monitored using a PCA-filtered principal curve regression method, while the small scale features were monitored using a variogram approach. When an out of control signal was detected, local monitoring identified the location of the defective area through clustering techniques. This method is able to locate defective part areas and improves upon existing monitoring methods by parameterizing the principal curve to capture the non-linear spatial variation patterns of the HDM data.
  - b. *Progressive Bayesian Monitoring for Multi-resolution Data.* The fusion model proposed in Chapter 2 was utilized to develop a progressive Bayesian monitoring framework. The prediction distributions at each measurement point were estimated using an MCMC sampling method to build control limits based on in-control data. The Bayesian framework was adopted to update surface model

parameters and control limits for monitoring the HDM data. A single-linkage clustering algorithm was developed to monitor and locate defective areas on a part without significantly increasing false alarm rates. A case study on an automotive engine machining process demonstrated the effectiveness of the proposed method. The method enabled the time efficient monitoring of HDM data when limited HDM data is available.

4. *Multistage Modeling and Monitoring of HDM Data.* A new method was presented for multistage surface variation monitoring using morphing and multi-resolution surface data. The variation propagation between stages was modeled using a functional morphing approach, which also provided a backward morphing prediction at the intermediate stages. The final surface prediction at the intermediate stages was obtained by using a hierarchical Bayesian model. The surface prediction was then monitored using a single-linkage cluster monitoring approach. The proposed approach reduced the need for HDM measurements at intermediate stages, while reducing the number of false alarms and misdetections. The proposed surface prediction model incorporated surface measurements at the intermediate stage, thus improving surface prediction accuracy when abnormal variations are present.

## **6.2. Future Work**

The following represents potential areas of future research:

- *Engineering-driven variable selection.* Although a number of candidate process variables can be pre-identified based on engineering knowledge for the data fusion surface model, different process variables play unequal roles in affecting surface

variations under various machining conditions. For example, the correlation between the MRR and surface height is varying as the remaining tool life decreases. To enhance surface model interpretability, an engineering-driven variable selection method can be developed to determine the key process variables that mostly contribute to surface variations.

- *HDM based Closed Loop Feedback Control.* Components of this dissertation can be incorporated into a closed loop feedback control methodology for two levels of surface variation as shown in Figure 6.1 and detailed below.

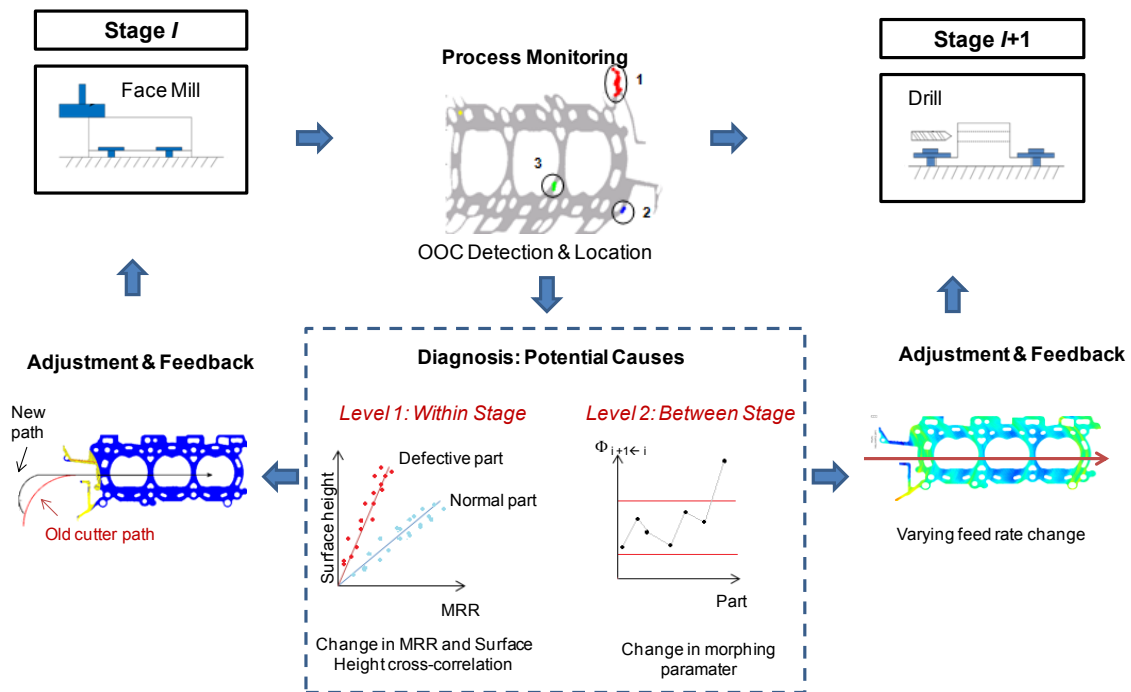


**Figure 6.1 Two level closed loop feedback control**

1. *Level 1: Surface variation reduction at a single stage.* The proposed MSA and monitoring methods may be combined with a previous surface variation reduction study [56] for close loop feedback control in an automotive milling process. In [56], an algorithm based on the cross-correlation between the MRR and surface



profile is utilized to minimize surface spatial variation through cutter path adjustment. A closed loop control method can be developed such that after detecting abnormal surface variations, the process can be diagnosed and adjusted. For instance, if the cross-correlation relationship between the MRR and abnormal surface profile changes, feedback to the machining systems can automatically adjust the cutter path based on the new updated correlation structure to eliminate the process abnormal conditions and minimize the surface variation.

2. *Level 2: Inter-stage Surface Variation Reduction.* The proposed morphing-based model and monitoring may be used for close-loop feedback control between manufacturing stages to reduce multistage surface variation. This task would first require the diagnosis of multistage surface variation by separating the effects of the variation sources of upstream/downstream stages from the current stage. When abnormal surface variation is detected through process monitoring, the forward mapping morphing function may be used to automatically introduce shape deformation in upstream operations to compensate for end-of-line form errors. For instance, in Figure 6.1, the morphing parameters calculated between stage 1 and stage 2 may be monitored. An out of control condition would indicate a change in the inter-stage surface morphing relationship. The updated morphing parameters could be used to quantify the change in the surface variation, and a process variable (such as feed rate) adjusted in stage 2 to compensate for this change.
- *Surface Model for Data Fusion.* The model proposed in Chapter 2 could be further improved to incorporate the correlation between parts over time. This might result in

more precise surface estimates. Extending the model to include previous part information has the potential to further reduce the number of HDM measurement points needed for process control.

- *Adaptive HDM systems.* Another potential future area of research is adaptive HDM systems. To decrease HDM data redundancy and increase system efficiency, adaptive algorithms could be developed to determine the resolution required to capture the local variation for different part areas. For example, higher resolution measurements could be obtained in part areas where monitoring identifies larger surface variation, or in the areas where defects are likely to occur. Lower resolution measurements could be obtained from areas where there is lower surface variation. The measurement resolution could be adjusted and updated with new incoming part measurement information. Such measurement strategies will further reduce the number of measurements needed to monitor process quality without sacrificing performance of the monitoring algorithms.

## REFERENCES

1. Nguyen, H., H. Wang, and S.J. Hu, *Characterization of Cutting Force Induced Surface Shape Variation Using High-Definition Metrology*. Proceedings of MSEC 2012, 2012a.
2. Nguyen, H., H. Wang, and S.J. Hu, *Cutter Tilt and Cutter-Spindle Stiffness Modeling for Machine Condition Monitoring in Face Milling Using High Definition Surface Metrology*. Submitted to International Journal of Machine Tool and Manufacture, 2012b.
3. Zhou, L., et al., *Functional Morphing in Multistage Manufacturing and Its Applications in High-Definition Metrology-Based Process Control*. Automation Science and Engineering, IEEE Transactions on, 2012. **9**(1): p. 124-136.
4. Zhu, X., H. Ding, and M.Y. Wang, *Form error evaluation: an iterative reweighted least squares algorithm*. Journal of manufacturing science and engineering, 2004. **126**(3): p. 535-541.
5. GROVE, D.-M., D.C. Woods, and S.M. LEWIS, *Multifactor B-spline mixed models in designed experiments for the engine mapping problem*. Journal of quality technology, 2004. **36**(4): p. 380-391.
6. Jung, H. and K. Kim, *A new parameterisation method for NURBS surface interpolation*. The International Journal of Advanced Manufacturing Technology, 2000. **16**(11): p. 784-790.
7. Yang, B.-D. and C.-H. Menq, *Compensation for form error of end-milled sculptured surfaces using discrete measurement data*. International Journal of Machine Tools and Manufacture, 1993. **33**(5): p. 725-740.
8. Xia, H., Y. Ding, and J. Wang, *Gaussian process method for form error assessment using coordinate measurements*. IIE Transactions, 2008. **40**(10): p. 931-946.
9. Yang, T.-H. and J. Jackman, *Form error estimation using spatial statistics*. Journal of manufacturing science and engineering, 2000. **122**(1): p. 262-272.
10. Atkinson, P., R. Webster, and P. Curran, *Cokriging with ground-based radiometry*. Remote Sensing of Environment, 1992. **41**(1): p. 45-60.

11. Curran, P. and H. Williamson, *Sample size for ground and remotely sensed data*. Remote Sensing of Environment, 1986. **20**(1): p. 31-41.
12. Wang, G., G. Gertner, and A. Anderson, *Sampling design and uncertainty based on spatial variability of spectral variables for mapping vegetation cover*. International Journal of Remote Sensing, 2005. **26**(15): p. 3255-3274.
13. Xiao, X., et al., *Optimal sampling scheme for estimation landscape mapping of vegetation cover*. Landscape ecology, 2005. **20**(4): p. 375-387.
14. Jin, R., C.-J. Chang, and J. Shi, *Sequential measurement strategy for wafer geometric profile estimation*. IIE Transactions, 2012. **44**(1): p. 1-12.
15. Wikle, C.K. and L.M. Berliner, *Combining information across spatial scales*. Technometrics, 2005. **47**(1): p. 80-91.
16. Qian, P.Z. and C.J. Wu, *Bayesian hierarchical modeling for integrating low-accuracy and high-accuracy experiments*. Technometrics, 2008. **50**(2): p. 192-204.
17. Xia, H., Y. Ding, and B.K. Mallick, *Bayesian hierarchical model for combining misaligned two-resolution metrology data*. IIE Transactions, 2011. **43**(4): p. 242-258.
18. Huang, Y. and X. Qian, *A dynamic sensing-and-modeling approach to three-dimensional point-and area-sensor integration*. Transactions-American Society of Mechanical Engineers Journal of Manufacturing Science and Engineering, 2007. **129**(3): p. 623.
19. Nolot, E. and A. André, *Systematic combination of X-ray reflectometry and spectroscopic ellipsometry: A powerful technique for reliable in-fab metrology*. Thin Solid Films, 2011. **519**(9): p. 2782-2786.
20. Apley, D.W. and F. Zhang, *Identifying and visualizing nonlinear variation patterns in multivariate manufacturing data*. IIE Transactions, 2007. **39**(6): p. 691-701.
21. Hastie, T. and W. Stuetzle, *Principal curves*. Journal of the American Statistical Association, 1989. **84**(406): p. 502-516.
22. Hastie, T., R. Tibshirani, and J. Friedman, *The elements of statistical learning: data mining, inference, and prediction*. 2001, Springer New York.
23. Chang, K.-Y. and J. Ghosh, *A unified model for probabilistic principal surfaces*. Pattern Analysis and Machine Intelligence, IEEE Transactions on, 2001. **23**(1): p. 22-41.

24. Kégl, B., et al., *Learning and design of principal curves*. Pattern Analysis and Machine Intelligence, IEEE Transactions on, 2000. **22**(3): p. 281-297.
25. Apley, D. and J. Shi, *Diagnosis of multiple fixture faults in panel assembly*. Journal of manufacturing science and engineering, 1998. **120**(4): p. 793-801.
26. Hu, S.J. and S. Wu, *Identifying sources of variation in automobile body assembly using principal component analysis*. Transactions of NAMRI/SME, 1992. **20**: p. 311-316.
27. Shi, J. and D. Ceglarek, *Fixture Failure Diagnosis for Autobody Assembly Using Pattern Recognition*. Journal of Engineering for Industry, 1996. **118**: p. 55.
28. Wang, H. and Q. Huang, *Error cancellation modeling and its application to machining process control*. IIE transactions, 2006. **38**(4): p. 355-364.
29. Etesami, F., *Tolerance verification through manufactured part modeling*. Journal of manufacturing systems, 1988. **7**(3): p. 223-232.
30. WANG, Y., et al., *Manufactured part modeling for characterization of geometric variations of automotive spaceframe extrusions*. Journal of manufacturing science and engineering, 1998. **120**(3): p. 523-531.
31. Zahouani, H., et al., *Identification of manufacturing signature by 2D wavelet decomposition*. Wear, 2008. **264**(5): p. 480-485.
32. Jeong, M.K., et al., *Wavelet-based data reduction techniques for process fault detection*. Technometrics, 2006. **48**(1): p. 26-40.
33. Jeong, M.K., J.-C. Lu, and N. Wang, *Wavelet-based SPC procedure for complicated functional data*. International Journal of Production Research, 2006. **44**(4): p. 729-744.
34. Lada, E.K., J.-C. Lu, and J.R. Wilson, *A wavelet-based procedure for process fault detection*. Semiconductor Manufacturing, IEEE Transactions on, 2002. **15**(1): p. 79-90.
35. Paynabar, K. and J. Jin, *Characterization of non-linear profiles variations using mixed-effect models and wavelets*. IIE Transactions, 2011. **43**(4): p. 275-290.
36. Johnson, R.A. and D.W. Wichern, *Applied multivariate statistical analysis*. Vol. 4. 1992: Prentice hall Englewood Cliffs, NJ.
37. Hawkins, D.M., *Multivariate Quality Control Based on Regression-Adjusted Variables*. Technometrics, 1991. **33**(1): p. 61-75.
38. Rao, S., et al., *Monitoring multistage integrated circuit fabrication processes*. Semiconductor Manufacturing, IEEE Transactions on, 1996. **9**(4): p. 495-505.

39. Wolbrecht, E., et al., *Monitoring and diagnosis of a multistage manufacturing process using Bayesian networks*. AI EDAM, 2000. **14**(01): p. 53-67.
40. Jin, M., Y. Li, and F. Tsung, *Chart allocation strategy for serial-parallel multistage manufacturing processes*. IIE Transactions, 2010. **42**(8): p. 577-588.
41. Zantek, P.F., G.P. Wright, and R.D. Plante, *Process and product improvement in manufacturing systems with correlated stages*. Management Science, 2002. **48**(5): p. 591-606.
42. Zhang, G., *Cause-selecting control charts—a new type of quality control charts*. The QR Journal, 1985. **12**(1).
43. Tsung, F., Y. Li, and M. Jin, *Statistical process control for multistage manufacturing and service operations: a review and some extensions*. International Journal of Services Operations and Informatics, 2008. **3**(2): p. 191-204.
44. Hu, S.J. and Y. Koren, *Stream-of-variation theory for automotive body assembly*. CIRP Annals-Manufacturing Technology, 1997. **46**(1): p. 1-6.
45. Shi, J., *Stream of variation modeling and analysis for multistage manufacturing processes*. Vol. 10. 2006: CRC.
46. Cai, W., S.J. Hu, and J. Yuan, *A variational method of robust fixture configuration design for 3-D workpieces*. Journal of Manufacturing Science and Engineering, 1997. **119**(4): p. 593-602.
47. Camelio, J., S.J. Hu, and D. Ceglarek, *Modeling variation propagation of multi-station assembly systems with compliant parts*. Journal of Mechanical Design, 2003. **125**(4): p. 673-681.
48. Jin, J. and J. Shi, *State Space Modeling of Sheet Metal Assembly for Dimensional Control*. Journal of manufacturing science and engineering, 1999. **121**: p. 756-762.
49. Zhou, S., Q. Huang, and J. Shi, *State space modeling of dimensional variation propagation in multistage machining process using differential motion vectors*. Robotics and Automation, IEEE Transactions on, 2003. **19**(2): p. 296-309.
50. Liu, J., J. Shi, and S.J. Hu, *Engineering-driven factor analysis for variation source identification in multistage manufacturing processes*. Journal of Manufacturing Science and Engineering, 2008. **130**(4): p. 41009.
51. Djurdjanovic, D. and N. JUN, *Dimensional errors of fixtures, locating and measurement datum features in the stream of variation modeling in machining*. Journal of manufacturing science and engineering, 2003. **125**(4): p. 716-730.

52. Wang, H. and Q. Huang, *Using error equivalence concept to automatically adjust discrete manufacturing processes for dimensional variation control*. Transactions-American Society of Mechanical Engineers Journal of Manufacturing Engineering, 2007. **129**(3): p. 644.
53. Zhong, J., J. Liu, and J. Shi, *Predictive control considering model uncertainty for variation reduction in multistage assembly processes*. Automation Science and Engineering, IEEE Transactions on, 2010. **7**(4): p. 724-735.
54. Ding, Y., D. Ceglarek, and J. Shi, *Fault diagnosis of multistage manufacturing processes by using state space approach*. Ann Arbor, 2002. **1001**: p. 48109.
55. Martinsen, K., *Vectorial tolerancing for all types of surfaces*. ASME DES ENG DIV PUBL DE., ASME, NEW YORK, NY(USA), 1993. **65**: p. 187-198.
56. Tai, B.L., et al., *Surface Variation Reduction for Face Milling based on High Definition Metrology*. Proceedings of MSEC 2012, 2012.
57. Banerjee, S., B.P. Carlin, and A.E. Gelfand, *Hierarchical modeling and analysis for spatial data*. Vol. 101. 2003: Chapman & Hall/CRC.
58. Majeske, K.D., *Approval criteria for multivariate measurement systems*. Journal of quality technology, 2008. **40**(2): p. 140-153.
59. Adamec, E. and R.K. Burdick, *Confidence intervals for a discrimination ratio in a gauge R&R study with three random factors*. Quality Engineering, 2003. **15**(3): p. 383-389.
60. Burdick, R.K., C.M. Borrer, and D.C. Montgomery, *A review of methods for measurement systems capability analysis*. Journal of Quality Technology, 2003. **35**(4): p. 342-354.
61. Montgomery, D.C. and G.C. Runger, *Applied statistics and probability for engineers*. 2010: Wiley.
62. Devore, J.L., *Probability and Statistics for Engineering and the Sciences*. 2011: Duxbury Press.
63. Franaszek, M., G.S. Cheok, and K.S. Saidi, *Gauging the Repeatability of 3-D Imaging Systems by Sphere Fitting*. Instrumentation and Measurement, IEEE Transactions on, 2011. **60**(2): p. 567-576.
64. Voelkel, J.G., *Gauge R&R analysis for two-dimensional data with circular tolerances*. Journal of quality technology, 2003. **35**(2): p. 153-167.
65. He, S.-G., G.A. Wang, and D.F. Cook, *Multivariate measurement system analysis in multisite testing: An online technique using principal component analysis*. Expert Systems with Applications, 2011. **38**(12): p. 14602-14608.

66. Huopaniemi, I., et al., *Multivariate multi-way analysis of multi-source data*. Bioinformatics, 2010. **26**(12): p. i391-i398.
67. Fujikoshi, Y., T. Himeno, and H. Wakaki, *Asymptotic results of a high dimensional MANOVA test and power comparison when the dimension is large compared to the sample size*. J. Japan Statist. Soc, 2004. **34**(1): p. 19-26.
68. Horton, P., et al., *Applications of multi-variate analysis of variance (MANOVA) to multi-electrode array electrophysiology data*. Journal of neuroscience methods, 2005. **146**(1): p. 22-41.
69. Wang, C.-C. and B.C. Jiang, *Integral DOE and MANOVA techniques for classification feature selection: using solder joint defects as an example*. The International Journal of Advanced Manufacturing Technology, 2005. **27**(3): p. 392-396.
70. Zitova, B. and J. Flusser, *Image registration methods: a survey*. Image and vision computing, 2003. **21**(11): p. 977-1000.
71. Campbell, R.J. and P.J. Flynn, *A survey of free-form object representation and recognition techniques*. Computer Vision and Image Understanding, 2001. **81**(2): p. 166-210.
72. Kittler, J., et al. *3D assisted face recognition: A survey of 3D imaging, modelling and recognition approaches*. in *Computer Vision and Pattern Recognition-Workshops, 2005. CVPR Workshops. IEEE Computer Society Conference on*. 2005. IEEE.
73. Eggert, D.W., A. Lorusso, and R.B. Fisher, *Estimating 3-D rigid body transformations: a comparison of four major algorithms*. Machine Vision and Applications, 1997. **9**(5): p. 272-290.
74. Besl, P.J. and N.D. McKay, *A method for registration of 3-D shapes*. IEEE Transactions on pattern analysis and machine intelligence, 1992. **14**(2): p. 239-256.
75. De Berg, M., et al., *Computational geometry: algorithms and applications*. 2008: Springer.
76. Samet, H., *The design and analysis of spatial data structures*. Vol. 85. 1990: Addison-Wesley Reading MA.
77. Chilès, J.P. and P. Delfiner, *Frontmatter*. 2008: Wiley Online Library.
78. Cressie, N., *Statistics for spatial data*. Terra Nova, 1992. **4**(5): p. 613-617.



79. Barber, C.B., D.P. Dobkin, and H. Huhdanpaa, *The quickhull algorithm for convex hulls*. ACM Transactions on Mathematical Software (TOMS), 1996. **22**(4): p. 469-483.
80. Lehmann, T.M., C. Gonner, and K. Spitzer, *Survey: Interpolation methods in medical image processing*. Medical Imaging, IEEE Transactions on, 1999. **18**(11): p. 1049-1075.
81. Li, J. and A.D. Heap, *A review of comparative studies of spatial interpolation methods in environmental sciences: Performance and impact factors*. Ecological Informatics, 2011. **6**(3): p. 228-241.
82. Srivastava, M.S. and M. Srivastava, *Methods of multivariate statistics*. 2002: Wiley-Interscience.
83. Yang, J., et al., *Two-dimensional PCA: a new approach to appearance-based face representation and recognition*. Pattern Analysis and Machine Intelligence, IEEE Transactions on, 2004. **26**(1): p. 131-137.
84. Amemiya, Y., *What should be done when an estimated between-group covariance matrix is not nonnegative definite?* The American Statistician, 1985. **39**(2): p. 112-117.
85. Wang, H., H. Kababji, and Q. Huang, *Monitoring global and local variations in multichannel functional data for manufacturing processes*. Journal of Manufacturing Systems, 2009. **28**(1): p. 11-16.
86. Lloyd, S., *Least squares quantization in PCM*. Information Theory, IEEE Transactions on, 1982. **28**(2): p. 129-137.
87. Barnes, R.J., *The variogram sill and the sample variance*. Mathematical Geology, 1991. **23**(4): p. 673-678.
88. Emery, X., *Reducing fluctuations in the sample variogram*. Stochastic Environmental Research and Risk Assessment, 2007. **21**(4): p. 391-403.
89. Gringarten, E. and C.V. Deutsch, *Teacher's aide variogram interpretation and modeling*. Mathematical Geology, 2001. **33**(4): p. 507-534.
90. Sibson, R., *SLINK: an optimally efficient algorithm for the single-link cluster method*. The Computer Journal, 1973. **16**(1): p. 30-34.
91. Coquillart, S., *Extended free-form deformation: a sculpturing tool for 3D geometric modeling*. Vol. 24. 1990: ACM.
92. Hsiao, S.-W. and M. Liu, *A morphing method for shape generation and image prediction in product design*. Design Studies, 2002. **23**(6): p. 533-556.

93. Sederberg, T.W. and S.R. Parry. *Free-form deformation of solid geometric models.* in *ACM Siggraph Computer Graphics*. 1986. ACM.